WAVE-INDUCED DEEP EQUATORIAL OCEAN CIRCULATION

A DISSERTATION SUBMITTED TO THE GRADUATE DIVISION OF THE UNIVERSITY OF HAWAII IN PARTIAL FULFILLMENT OF THE REQUIREMENTS FOR THE DEGREE OF

DOCTOR OF PHILOSOPHY

IN

OCEANOGRAPHY

AUGUST 2008

By

François Ascani

Thesis Committee:

Eric Firing, Chairperson

Fei-Fei Jin

Dennis W. Moore

Julian P. McCreary

Douglas S. Luther

We certify that we have read this thesis and that, in our opinion, it is satisfactory in scope and quality as a dissertation for the degree of Doctor of Philosophy in Oceanography.

THESIS COMMITTEE

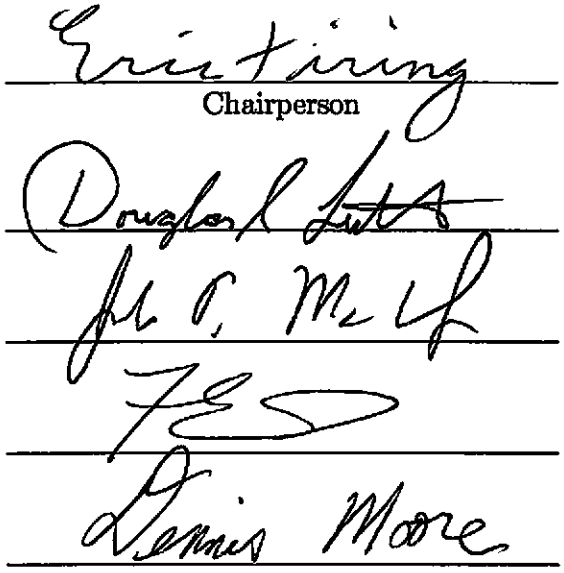

Chairperson

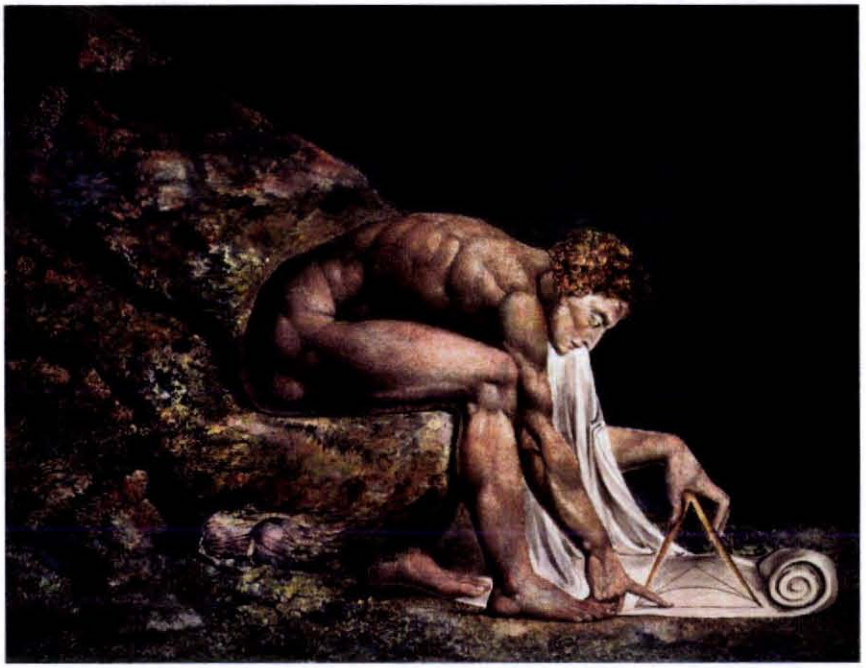

William Blake's *Newton* (1795)

"J'avais besoin de théorie pour structurer ma pensée et t'objectais qu'une pensée non structurée menace toujours de sombrer dans l'empirisme et l'insignifiance. Tu répondais que la théorie menace toujours de devenir un carcan qui interdit de percevoir la complexité mouvante du réel."

André Gorz, *Lettre à D., Histoire d'un amour.*

"The love of complexity without reductionism makes art; the love of complexity with reductionism makes science."

Edward O. Wilson, *Consilience: the unity of knowledge.*

ABSTRACT

In the Pacific and Atlantic oceans, a complex equatorial current structure is found below the thermocline. The currents are zonal with typical speeds from 5 to 20 cm s^{-1} and extend as deep as 2500 m. The structure can be divided into two overlapping parts: the Tall Equatorial Jets (TEJs), with large vertical scale and alternating with latitude, and the Equatorial Deep Jets (EDJs), centered on the equator and alternating in the vertical with a wavelength of several hundred meters.

This circulation poses a computational and a theoretical challenge. First, state-of-the-art high-resolution regional models and Ocean General Circulation Models (OGCMs) typically produce a rather weak, inaccurate and incomplete picture of the circulation. Second, the most promising existing theory, based on the rectification of intraseasonal Yanai waves, cannot account for the basin-wide presence of the TEJs.

In the present study, using idealized numerical simulations and analytical solutions, we demonstrate that the TEJs could result from a rectification of a beam of monthly-periodic Yanai waves that is generated in the eastern part of the basin by instabilities of the swift equatorial surface currents.

For weak Yanai wave amplitude, currents resembling the TEJs are obtained, but only within the beam. They are the mean Eulerian flow, which cancels the Stokes drift of the Yanai waves, yielding a zero-mean Lagrangian flow: the water parcels conserve their potential vorticity (PV) and are stationary over a wave cycle. With stronger amplitude, the Yanai waves become unstable, and lose their energy to small vertical scales where it is dissipated. The resulting vertical decay of the Yanai waves provides a source of PV, allowing water parcels to move meridionally within the beam. This process results in TEJs with a mean Lagrangian zonal flow extending to the west of the beam.

Contents

List of Tables

List of Figures

Chapter 1

Introduction

1.1 Brief review of the observed circulation

Below the Equatorial Undercurrent (EUC) and the pair of South and North Subsurface Countercurrents (SSCC and NSCC), a superposition of two different sets of zonal flows can be found in the Pacific (Fig. 1.1a; see also Firing 1987, Firing *et al.* 1998) and Atlantic (Schott *et al.* 1995; Gouriou *et al.* 2001; Bourlès *et al.* 2002; Bourlès *et al.* 2003; Schott *et al.* 2003; Ollitrault *et al.* 2006) equatorial oceans. A first set of large-vertical-scale zonal currents with typical mean velocities ranging from 5 to 15 cm s^{-1}that alternate meridionally is found down to 1500 m depth. These currents will be named hereafter the Tall Equatorial Jets (TEJs). They are the westward South and North Equatorial Intermediate Currents (SEIC and NEIC; note that the NEIC is missing in Fig. 1.1a) located around 3° off the equator, the eastward South and North Intermediate Countercurrents (SICC and NICC) located around 1.5–2° off the equator, the Equatorial Intermediate Current (EIC), a robust westward flow located just below the EUC, and the Lower Equatorial Intermediate Current (LEIC), an inconsistent deep extension of the EIC found down to 600 m depth.

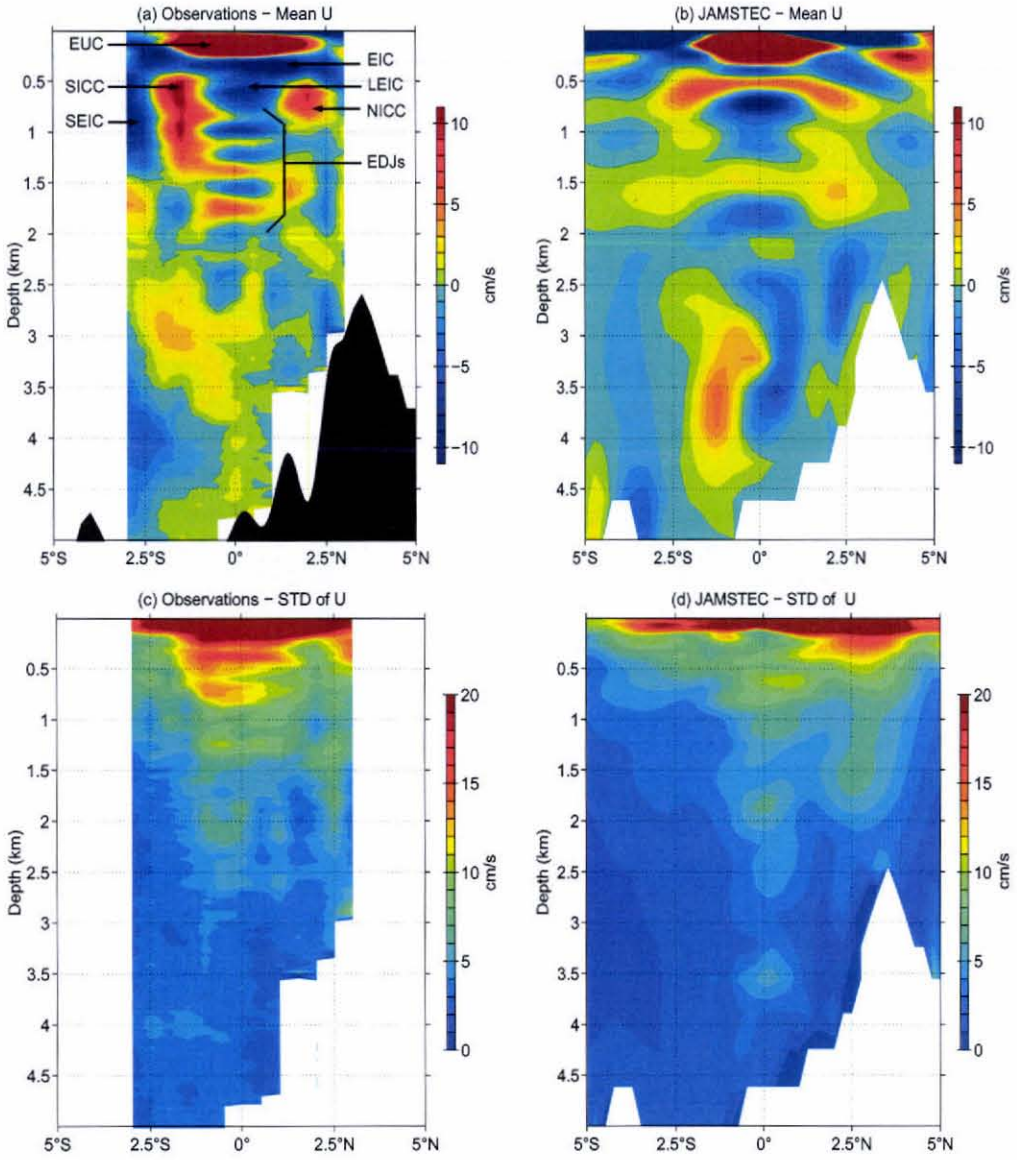

Figure 1.1: Mean (upper) zonal velocity U and its standard deviation (lower) at 159°W: (a) and (c) observed from March 1982 to June 1983 (Firing 1987) and (b) and (d) over model year 20 in JAMSTEC.

A second set of small-vertical-scale (about 150–200 m) zonal currents within 1.5° of the equator and alternating vertically between 500 and 2500 m depth, is superimposed on the first set. These are the Equatorial Deep Jets (EDJs). Their typical mean zonal velocity ranges from 5 to 10 cm s^{-1}, but individual jets in synoptic profiles can reach 25 cm s^{-1}. Observations have found the EDJs to have a rather large zonal scale, suggesting that they, like the TEJs, are basin-scale features (Dutrieux *et al.* 2008). These jets may propagate vertically, taking at least several years per cycle, but this aspect of this variability is not yet clear (Firing 1987; Send *et al.* 2002; Johnson *et al.* 2002; Johnson and Zhang 2003). Unlike the TEJs, EDJ-like currents have also been observed in synoptic sections in the Indian Ocean (*e.g.*, Luyten and Swallow 1976; Dengler and Quadfasel 2002) but their temporal and zonal structure is much less known. Nevertheless, the vertical scale of the EDJs tends to be larger in the Atlantic and Indian oceans than in the Pacific, and their meridional and vertical structures do not quite match in neither oceans Kelvin or Rossby waves (*e.g.*, Ascani 2005).

During 1982–1983 in the central Pacific, the amplitude of the mean NEIC/SEIC and SICC/NICC were about as large as their variability, while the mean EIC/LEIC and EDJs were either half or as large as the magnitude of their variability (Fig. 1.1c). Such variability may have been higher than average owing to El-Niño conditions (Firing 1987).

1.2 The modelling challenge

Despite the recent improvement in spatial resolution, realistically-forced numerical models have produced an inconsistent and unsatisfactory picture of the deep equatorial circulation. Brandt and Eden (2005; their Fig. 2), using a regional primitive equation (PE) model of the tropical Atlantic (12°S–12°N respectively) with

a 1/3° horizontal resolution and 450 levels in the vertical, found at 35°W a mean deep equatorial circulation with little resemblance to the observations. Böning and Kröger (2005; their Fig. 4c), using a hierarchy of regional PE models of the tropical and North Atlantic (18°S–70°N) with 45 levels in the vertical and from 1/3° to 1/12° resolution, obtained weak EIC/LEIC and SICC/NICC but no EDJs. Nakano and Hasumi (2005; their Fig. 5c) using a PE model of the Pacific Ocean with 1/4° resolution in longitude, 1/6° in latitude, and 54 levels in the vertical found only a tendency to eastward and westward flows off the equator and to smaller vertical scales on the equator. Recently, output from several PE global and regional models of the Pacific and Atlantic, with resolutions varying from 1/4° to 1/10° in the horizontal and from 40 to 106 levels in the vertical, show that the EIC, SICC and NICC are robust model features although generally weaker and shallower than in the observations. At the same time, the SEIC, NEIC and the EDJs appear much less consistently in these solutions (Ascani *et al.* 2008).

Among all these models, the most realistic circulation to our knowledge is the Pacific basin in the JAMSTEC model (Ishida *et al.* 1998; Ascani *et al.* 2008). In this model, the SEIC and NEIC appear as weak currents. The SICC, NICC, EIC and LEIC are comparable to observations, but the SICC and NICC do not extend as deep as observed (Fig. 1.1b). The EDJs are also reproduced all across the Pacific basin, but their vertical wavelength is about twice the observed one (Fig. 1.2a). The ratio of the mean currents to their variability is also comparable to the 1982–1983 observations (Fig. 1.1d).

The main conclusion from prior work is that we do not know the necessary and sufficient ingredients needed to reproduce a realistic deep mean equatorial circulation in numerical models. Although resolution would seem critical, some models with a poorer resolution than others paradoxically reproduce more realistic deep mean cur-

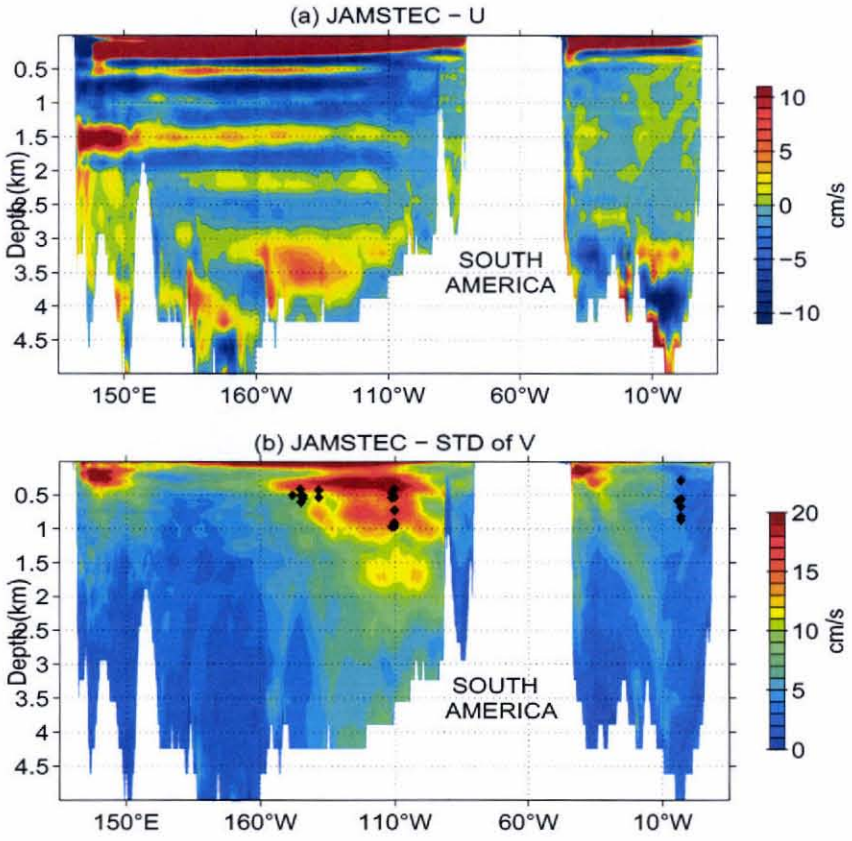

Figure 1.2: (a) Mean equatorial U and (b) standard deviation of equatorial V over years 20–22 in the JAMSTEC model. Black diamonds in (b) show the locations of the moorings used to compute the averaged power spectrum density (PSD) in Fig. 2.6.

rents. Although the deep equatorial circulation appears significantly stronger with biharmonic than Laplacian mixing, its structure exhibits little sensitive to mixing strength (Ascani 2005). Differences in wind stress, the main forcing of the models, have not been addressed with respect to the deep mean equatorial circulation. It is possible that the type of wind product used may have significant impact on the realism of the circulation. Finally but not less puzzling, a model can in the same run perform well in one basin but poorly in another. This situation is the case for the JAMSTEC model, which reproduces a realistic Pacific circulation but a relatively poor Atlantic one: for instance, notice the absence of EDJs in the Atlantic in Fig. 1.2a. Although the deep mean equatorial circulation can be considered a secondary feature of the general ocean circulation, its absence in numerical models may reflect some important modelling deficiencies.

1.3 The theoretical challenge

Several theories have been suggested to explain the deep equatorial currents, but even the most recent ones are still incomplete. Wind-forced linear equatorial waves alone were first proposed to explain the EDJs but it was later realized that unrealistically low-frequency waves are needed to reproduce the relative vertical stationarity of the EDJs (*e.g.* Wunsch 1977; McCreary 1984) except in the presence of a relatively strong and uniform equatorial background flow (McCreary and Lukas 1986), which has not been observed in the mean.

Recently, it has been conjectured that high-frequency (defined here as periods between 10 and 100 days) equatorial waves may generate the deep mean flows *via* instability. Only the case of mixed Rossby-gravity (Yanai) waves forming one vertical mode has been studied so far. First, d'Orgeville and Hua (2005) studied the instability of a zonally-independent ($k = 0$, where k is the zonal wavenumber) Yanai

mode. In their numerical simulations, they observed the formation of small and large-vertical-scale mean flows, which are partly consistent with the observations: the small-vertical-scale currents are not centered on the equator and they do not coexist with the large-vertical-scale structure because it is the breaking of the former which gives rise to the latter. d'Orgeville *et al.* (2007; herafter dOrg07) and Hua *et al.* (2008; hereafter Hua08) then studied the destabilization of $k \neq 0$ Yanai waves in a zonal channel. They observed that only westward-propagating Yanai waves with very short zonal wavelengths ($k \ll 0$) destabilize into large and small-vertical-scale mean flows resembling the TEJs and EDJs. The instability is described as a set of triad interactions, and this description successfully predicts the vertical and meridional structure of the mean flows they obtain in their numerical simulations. In particular, it is found that the waves need to have periods of around 60 days in order to reproduce the vertical scale of the Atlantic EDJs. The authors argue that one source of such variability can be intraseasonal variability of the Deep Western Boundary Current (DWBC) and they test the hypothesis in a basin configuration by forcing the Yanai wave along the western boundary. They find that, although the EDJs are found everywhere along the equator forming low-frequency equatorial basin modes (Cane and Moore 1981), the TEJs are found only near the western boundary where the instability occurs, inconsistent with the observations.

The theory proposed so far by dOrg07 and Hua08 is incomplete. First, it does not explain why the TEJs are also found away from the western boundary. Second, its applicability is unclear in the Pacific, where little is known about the high-frequency variability of the DWBC at the equator.

1.4 Present study

In this study, a new scenario to generate the TEJs is suggested. It is based on the working hypothesis that

> *the monthly-periodic variability generated by instabilities of surface equatorial currents in the central-eastern Pacific and Atlantic, which radiate into the deep ocean mostly as Yanai waves with moderate k, constitutes one important source of energy and potential vorticity (PV) for the TEJs and EDJs.*

This hypothesis has been motivated in part by the analysis of the JAMSTEC model (Section 2.1). It has the advantage of 1) explaining why the TEJs are found away from the western boundary and 2) offering a single explanation for both the Atlantic and Pacific oceans where the monthly variability appears to be ubiquitous (Section 2.2).

The hypothesis is first tested in a numerical model of an idealized equatorial oceanic basin by directly forcing a beam of monthly-periodic and moderate k Yanai waves and observing its subsequent rectification into mean flows (Chapter 3). Details and configuration of the different simulations are given in Section 3.2. The numerical solutions and their sensitivity to different model and forcing parameters are presented in Sections 3.3 and 3.4.

The classic mechanism of mean flow generation by wave dissipation (*e.g.*, Andrews and McIntyre 1976) is then proposed to explain the generation of the TEJs. Analytical solutions of the mean flows resulting from a single plane Yanai wave or a Yanai beam are derived in Chapter 4 and compared to two of the numerical solutions. Discussion and conclusions follows (Chapter 5).

The main differences from the recent dOrg07 and Hua08 studies are: 1) the configuration of the high-frequency variability, which forms a well-defined beam *propa-*

gating vertically and away from the western boundary leaving a zone to the west and to the east free of any forced motion; 2) the regime of instability with formation of mean flows observed at the monthly period and moderate k; 3) the use of the same source of variability for the Pacific and Atlantic oceans; and finally 4) the application of a mechanism already tested successfully as an explanation for a number of geophysical motions (*e.g.*, Andrews and McIntyre 1976; Rhines and Holland 1979; Haidvogel and Rhines 1983).

Chapter 2

Motivation

2.1 Mean potential vorticity balance in the JAMSTEC model

One of the most realistic simulations of deep equatorial circulation among all reported models is the Pacific basin in the JAMSTEC model. The analysis of this model reveals that the monthly-periodic variability found at depth in the central-eastern Pacific may be an important source of energy and PV for the deep equatorial mean flows.

Several reasons point to an eastern source for the EDJs and TEJs. The primary reason is that the TEJs form zonally elongated gyres closed at the western boundary and at the Galápagos Islands (Fig. 2.1a). If we assume that the TEJs are Lagrangian mean flows, then water parcels need to change their PV in order to recirculate at each edge of the gyre. At the western edge, western boundary processes such as lateral mixing offer the needed source of PV to close the gyre. In the east, however, no such process exists and another source of PV is needed.

A secondary reason is the presence in the model of a strong high-frequency vari-

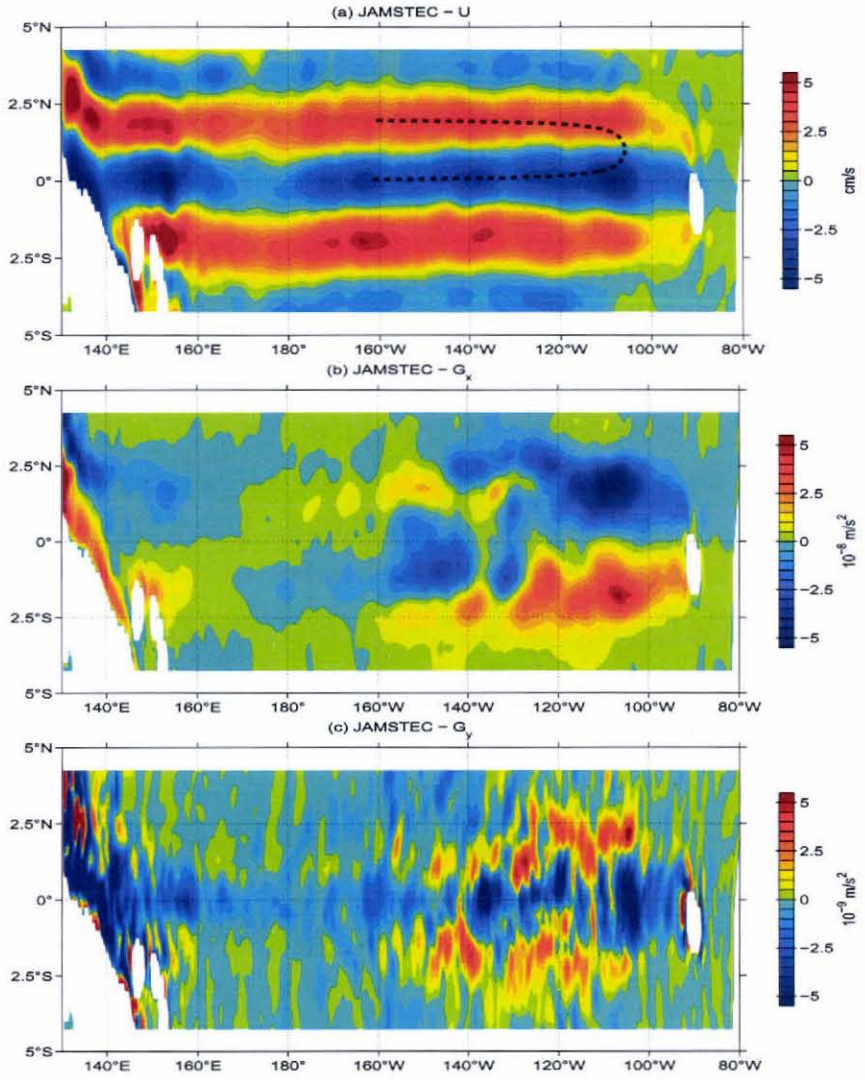

Figure 2.1: (a) Thickness-weighted mean zonal velocity (see text), and (b) zonal and (c) meridional eddy PV fluxes G_x and G_y. All quantities are averaged over 26.9-27.3 kg/m^3 (about 490-890 m) and over years 20-22. This range of potential density anomaly corresponds to the depths of the main core of the eastward TEJs in JAMSTEC (Fig. 1.1). The dashed line in (a) illustrates the recirculation of a water particle in the eastern Pacific.

ability generated by the upper-ocean instabilities in the central-eastern Pacific. Such variability is a source of energy for the deep ocean that, if dissipated, could in turn be a source of PV. In Section 2.2, this variability is shown to be a robust feature of not only the central-eastern Pacific Ocean but also the Atlantic Ocean in both observations and numerical models. In the JAMSTEC model, it strongly peaks in the Pacific at the monthly period (Fig. 2.6a and b) and is associated mainly with Yanai waves and to a lesser extent first-meridional-mode Rossby waves. It is revealed for instance *via* the standard deviation of the meridional velocity field on the equator (Fig. 1.2b), which shows an ill-defined beam of energy starting in the central-eastern Pacific near the surface and radiating downward and eastward, reaching the Galápagos Islands near 90°W at mid-depth.

To diagnose the effects of this high-frequency variability on the deep mean flows, the balance of PV is decomposed into a mean and eddy terms. PV is computed along isopycnals and defined as

$$q = \frac{f + \zeta}{h} \tag{2.1}$$

where f is the planetary vorticity, $h = -\partial_\rho z$ and z and ρ are the depth and potential density of the isopycnal. The vertical component of vorticity is $\zeta = \partial_x v - \partial_y u$, where u and v are the zonal and meridional velocities taken along isopycnals. The variables are taken from 5-day snapshots over years 20–22 of a climatological run. Details about the run and model configuration can be found in Ishida *et al.* (1998). For every quantity a, one considers only two components, its 3-year time-mean $\overline{a}$ and its Yanai-wave (or "eddy") component a' defined as the band-pass filtered version of a between the 23 and 55-day periods. The addition of other components has only a negligeable effect.

For a quasi-steady state and in the absence of dissipation and external source/sink

of PV, the time-mean PV balance is

$$(\overline{h}\overline{u}^*)\,\partial_x\overline{q} + (\overline{h}\overline{v}^*)\,\partial_y\overline{q} = -\partial_x\overline{(hu)'\,q'} - \partial_y\overline{(hv)'\,q'}, \tag{2.2}$$

where $\overline{u}^* = \overline{hu}/\overline{h}$ and $\overline{v}^* = \overline{hv}/\overline{h}$ are the thickness-weighted mean zonal and meridional velocities respectively (Vallis 2006). Because $\overline{q}$ is dominated by $f/\overline{h}$ and $\overline{h}$ is nearly horizontally uniform at depth, the balance (2.2) is approximated by

$$\beta\overline{v}^* \approx -\partial_x\overline{(hu)'\,q'} - \partial_y\overline{(hv)'\,q'} \tag{2.3}$$

where $\beta = \partial_y f$. Equation (2.3) is the "turbulent" Sverdrup equation (Rhines and Holland 1979; Holland and Rhines 1980) and quantifies the effect of the eddies on the mean meridional circulation.

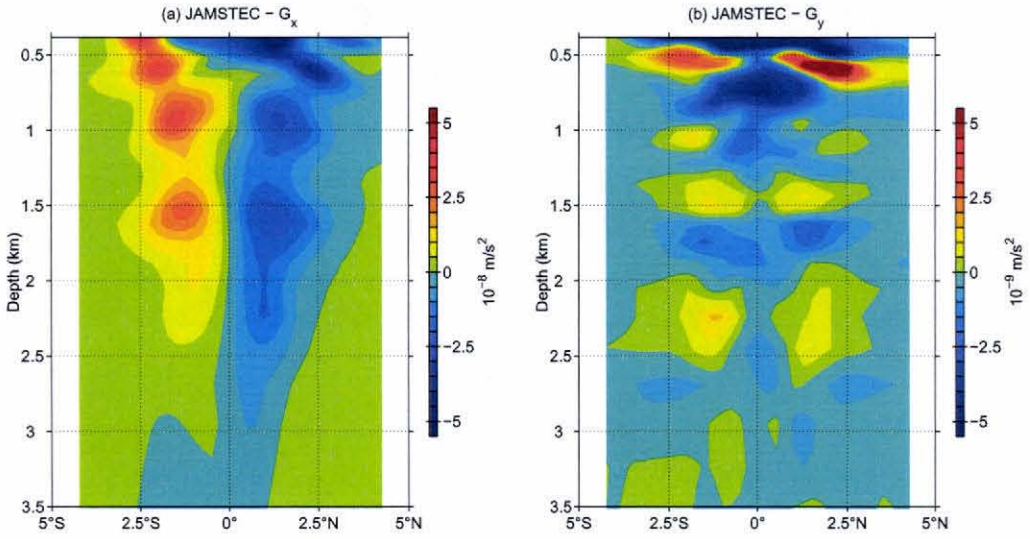

Figure 2.2: (a) G_x and (b) G_y averaged between 140°W and 95°W.

One advantage of using this formulation is that the zonal circulation $\overline{u}^*$ induced by the eddies can be deduced in the same way as for the classic wind-driven Sverdrup circulation (Kessler *et al.* 2003). For a quasi-steady state and $\overline{h}$ nearly uniform in

space, the continuity equation is approximately

$$\partial_x \overline{u}^* + \partial_y \overline{v}^* \approx 0, \tag{2.4}$$

and the difference in eddy-induced zonal flow between two longitudes L_w and L_e is then

$$\overline{u}^*(L_w) - \overline{u}^*(L_e) = -\frac{1}{\beta} \int_{L_w}^{L_e} \partial_y \vec{\nabla} \cdot \vec{G}\, dx, \tag{2.5}$$

where

$$\vec{G} = (G_x, G_y) = (\overline{(hu)' q'}, \overline{(hv)' q'}) \tag{2.6}$$

is the mean eddy PV flux. A meridional gradient in the divergence of the eddy PV flux will thus result in a mean zonal flow.

In JAMSTEC, the mean eddy PV flux away from boundaries is concentrated in the central-eastern Pacific where the Yanai wave is radiating (Fig. 2.1 and 2.2). The zonal flux G_x is antisymmetric about the equator being negative north of the equator and stays mostly of the same sign over depth (Fig. 2.1b and 2.2a). The meridional flux G_y is mostly symmetric being negative or zero at the equator while it alternates sign on the vertical at 2° off the equator (Fig. 2.1c and 2.2b).

Although G_y is an order of magnitude weaker than G_x, its eddy-induced zonal velocity in Eq. (2.5) is an order of magnitude larger and appears to be the dominant term responsible for the deep mean flows (Fig. 2.3c and d). Unfortunately, G_y is also noisier than G_x and its eddy-induced zonal velocity bears little resemblance with the output flows (Fig. 2.3a and d). The noisiness of G_y is concentrated within a few degrees from the equator and may be related to the nature of the eddy variability, which is dominated by Yanai waves. Only by averaging over the depths of the main core of the eastward TEJs (from about 490 to 890 m) is a profile obtained that shares the same tendency of westward flow on the equator and eastward flows off the equator as the output flows (Fig. 2.4). In the case of G_x, its eddy-induced velocity is

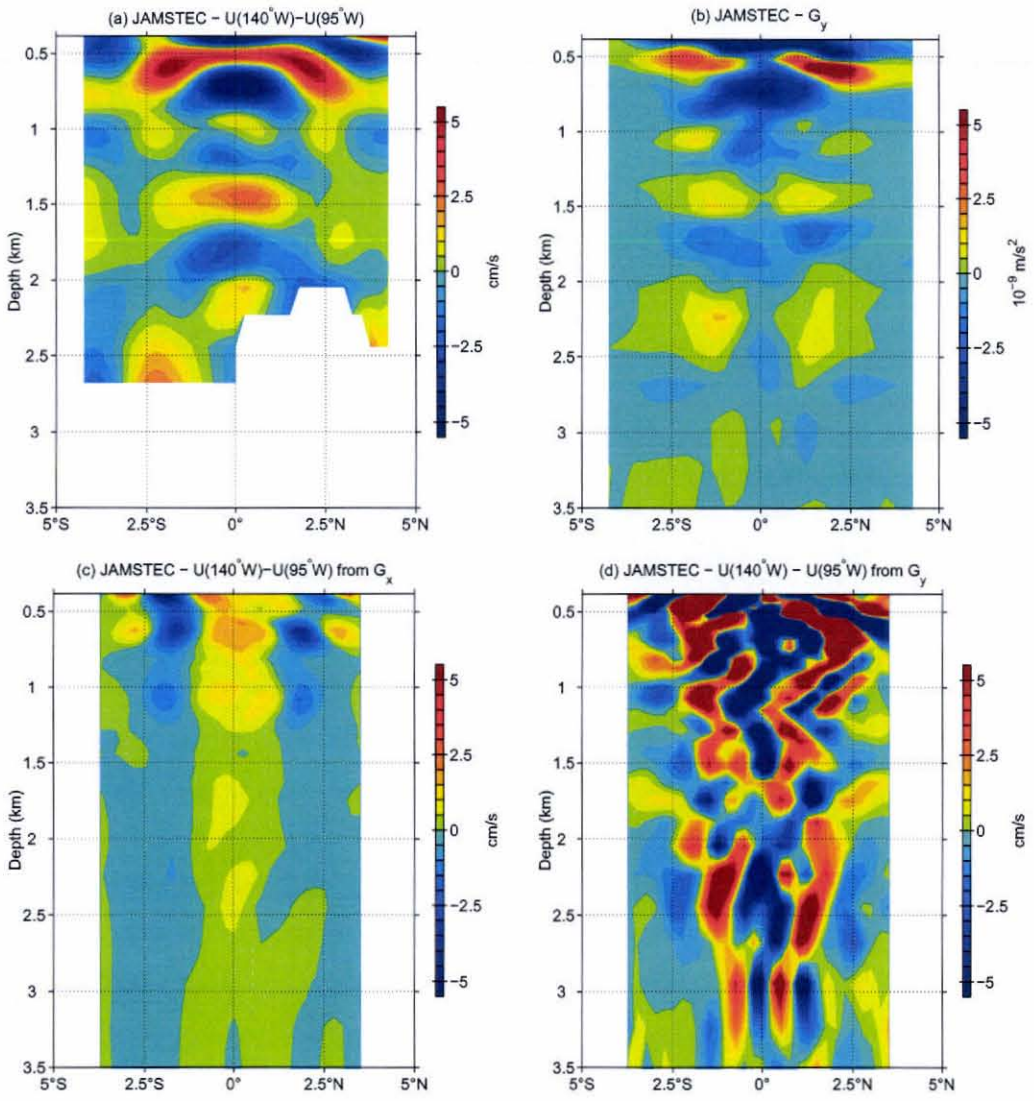

Figure 2.3: Thickness-weighted mean zonal velocity difference between 140°W and 95°W (a) from the model output over years 20–22, (c) from G_x alone and (d) from G_y alone as described by Eq. (2.5). In (b) is reproduced G_y for a qualitative comparison with (a).

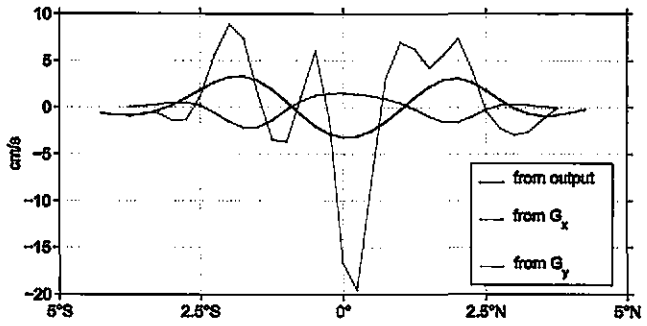

Figure 2.4: Thickness-weighted mean zonal velocity difference between 140°W and 95°W from the model output over years 20–22 (black), from G_x (blue) and from G_y (red) averaged over the depths of the main cores of the eastward TEJs as in Fig. 2.1.

weaker and tends to oppose the mean flows, suggesting that G_y is the driver of the TEJs and G_x a sink.

The TEJs as well as two westward EDJs can nonetheless be *qualitatively* explained as a result of G_y (Fig. 2.3a and b). At several depths, G_y is negative on the equator and positive 2° off (500, 1100 and 1500 m), or negative on the equator with no reversal (750, 1250 m). According to Eq. (2.5), both structure lead to eastward flows about 2° off the equator consistent with the eastward TEJs. They also lead to westward flow on the equator, consistent with the westward EDJs found at 750 and 1250 m depth, but not at 500, 1100 and 1500 m where eastward EDJs are found instead. Finally, in the case with meridional reversal only, it leads to westward flows poleward of 2–3° relatively consistent with the weak westward TEJs off the equator.

2.2 High-frequency equatorial waves in observations and models

The high-frequency variability present at depth in the JAMSTEC model appears ubiquitous in both the central-eastern Pacific and Atlantic oceans and seems to be dominated by monthly-periodic Yanai waves. Its presence in both observations and numerical models is reviewed in this section.

In the eastern Pacific, Harvey and Patzert (1976) observed a high-frequency motion near the bottom around 95°W. Although their time series was only two months long, they identified a motion with a 25-day and 1000-km zonal-wavelength wave and an amplitude of 4 cm s^{-1} propagating westward with a phase speed of 50 cm s^{-1}. They interpretated it as a first-baroclinic, first-meridional-mode equatorial Rossby wave, but later Cox (1980) suggested that their data were also consistent with a Yanai wave. Further west, Eriksen and Richman (1988) analyzed two-year long time series near 145°W and from 1500 and 3000 m, finding energy distributed over a broad band in frequency and a narrow band in zonal wavenumber. Although their error bars are large, they estimated that the motion was consistent with first-meridional-mode Rossby waves for periods of 45 days and longer and with Yanai waves for periods 30 days and shorter, both with zonal wavelength longer than 1000 km.

In the eastern Atlantic, Weisberg *et al.* (1979) and Weisberg and Horigan (1981) observed a monthly-periodic Yanai wave between 500 and 2000 m and near 3°W, with upward-propagating phase, an amplitude of about 15 cm s^{-1}, and a zonal wavelength of about 1200 km. They estimated a zonal phase speed of about 50 cm s^{-1} and a vertical wavelength centered at 1600 m (hereafter vertical wavelengths are given for a local Brunt-Väisälä frequency of 1 cph). Near 10°W, Bunge *et al.* (2006) reported that the meridional velocity V between 700 and 1600 m depth is dominated by

motions at the 14 and 60-day periods, although monthly-periodic motions are also found at most depths with an amplitude of about 10–20 cm s^{-1}.

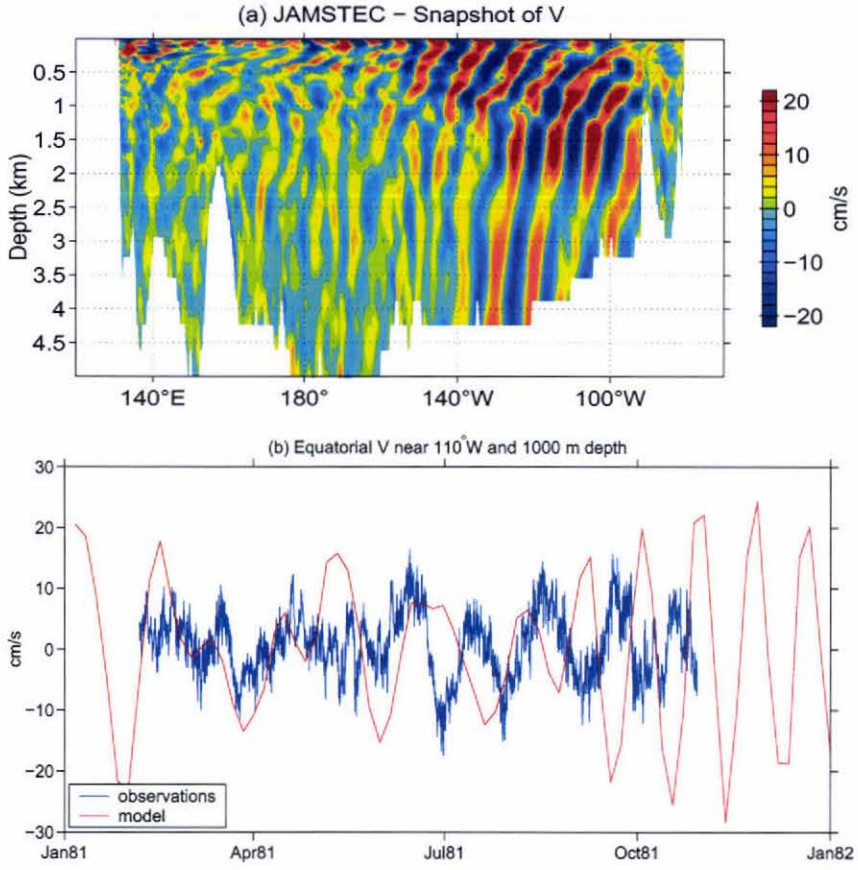

Figure 2.5: (a) Snapshot of equatorial V in JAMSTEC on Jan. 1, year 20 in the Pacific Ocean. (b) Time series of equatorial V near 110° W and 1000 m depth observed during 1981 from EPOCS and obtained for year 22 in JAMSTEC.

In numerical models of the tropical Pacific, Cox (1980) and Masina and Philander (1999) have observed deep motion radiating from the surface instabilities, consistent with first-meridional-mode Rossby and Yanai waves. Cox (1980) fitted the deep signal with a 1.1-month period and a 1000-km zonal wavelength waves, with the Rossby waves being nearly barotropic while the Yanai waves had a vertical

wavelength of about 1800 m. In Masina and Philander (1999), the waves were found to have zonal wavelengths of about 1200 and 900 km, respectively, for both Rossby and Yanai waves.

In JAMSTEC, as mentioned earlier, there is a beam composed mostly of Yanai waves radiating from the surface in the eastern Pacific down to the bottom. A snapshot of equatorial V is plotted in Fig. 2.5a, and its time series near 110°W and 1000 m depth is compared in Fig. 2.5b to the observed time series at about the same location from EPOCS (Tang *et al.* 1988). The zonal wavelength is about 1100 km, consistent with observations, and its vertical wavelength is about 1500 m, which is within the range of the observed estimates.

The period of the variability is also close to the observed dominant period. For instance, averaged power density spectra (PSD) in model equatorial V are compared to observed PSD from the PEQUOD program (Eriksen 1985) near 145°W (Fig. 2.6a) and from the EPOCS program near 110°W (Fig. 2.6b), all computed from moorings between 400 and 1000 m. It is fortunate that these moorings lie within the beam of the Yanai wave according to the JAMSTEC model (Fig. 1.2b). In both the model and observations, there is a peak near the monthly period. Although the low and high-frequency tails of the model spectra are consistent with the observations, the model overestimates the amount of energy available at the monthly period (Fig. 2.5b). In the model and observations, the variability is modulated annually, owing to the annual cycle of the surface instabilities that generate it (*e.g.*, Menkes *et al.* 2002; Lyman *et al.* 2007).

High-frequency equatorial waves are also observed in numerical models of the Atlantic. Li and Chang (1999) reported the full spectrum of equatorial waves present in their OGCM. In particular, the central part of the basin is dominated by monthly Yanai waves generated by the surface instabilities. In JAMSTEC, there is a well-

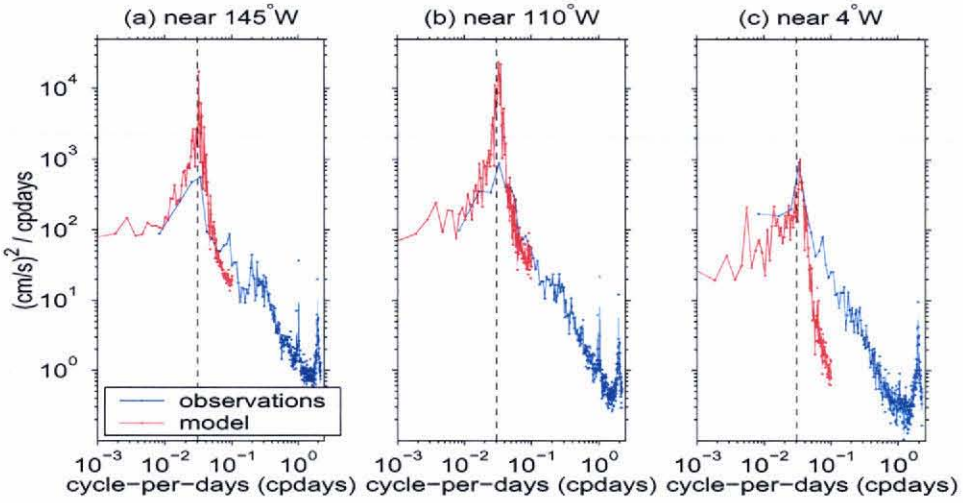

Figure 2.6: Averaged power spectrum density (PSD) in equatorial V from JAMSTEC (red) compared to observed ones (blue). The model PSD is obtained over years 20–22, averaged between 400 and 1000 m depth and over 148°W–138°W in (a), 111°W–110°W in (b) and 4°W–3°W in (c). Observations are near 145°W from PEQUOD during 1980–83 (Eriksen and Richman 1988) in (a), near 110°W from EPOCS during 1980–82 (Tang *et al.* 1988) in (b) and near 4°W from Weisberg and Horigan (1981) during 1977–78 in (c). Their exact locations are shown in Fig. 1.2b. All selected moorings are within 0.1° from the equator and between 400 and 1000 m depth. The dashed line shows the 1.1-month period.

defined beam of monthly Yanai waves starting at the surface near the western boundary and reaching 10°W at about 2000 m (Fig. 1.2b). A very similar beam is also found in a climatological run of the OGCM of the Earth Simulator model (Dutrieux, personnal communication; Masumoto *et al.* 2004).

If such high-frequency waves are present in both basins and if the working hypothesis is correct, a first question would be why the JAMSTEC model does not also reproduce the deep mean flows in the Atlantic (Fig. 1.2a). One possible reason

is that the level of energy at the monthly period reproduced in JAMSTEC in the Altantic is much weaker than in the Pacific (Fig. 2.6): the model overestimates the amplitude of the monthly signal in the Pacific but predicts the correct amplitude in the Atlantic. This situation may suggest that for some reason the JAMSTEC model, and maybe OGCMs in general, have to generate unrealistically strong monthly-periodic variability to reproduce the deep equatorial mean flows.

In any case, both observations and models show a robust feature of enhanced energy below the thermocline at high-frequency corresponding to Yanai and first-meridional-mode Rossby waves. We decided to test first the rectification of the monthly Yanai waves that dominate the variability, keeping in mind that other equatorial waves should be considered as well. Also, because of the variability and the annual modulation of the surface instabilities, the spectra in frequency and zonal wavenumber of the waves observed at depth are relatively broad. Thus both broad-band (BB) and narrow-band (NB) spectra in frequency and zonal wavenumber are considered in the present study, the former to test the hypothesis with a somewhat realistic variability, the latter in order to isolate the mechanism at play. The similarities in the oceanic response to these two types of spectrum, as well as to spectra centered at different periods and zonal wavelengths show, however, that the results are not critically sensitive to the exact shape and location of the spectra used to generate the high-frequency variability.

Chapter 3

Numerical solutions

3.1 Summary

In this chapter, the hypothesis that high-frequency Yanai waves can rectify into deep equatorial currents resembling the observations is directly tested in a numerical model. A beam of Yanai wave is forced by surface stress, and it is found that the beam indeed rectifies into a set of large-vertical-scale currents resembling the TEJs. For relatively strong amplitudes, the currents are found within and to the west of the beam, extending to the western boundary. Depending on the amplitude of the beam, structures resembling the EDJs are also found, but the present set of experiments does not enable us to conclude if they are real or an artifact of the way the model is forced.

3.2 Configuration of experiments

The Parallel Ocean Program (POP) model (*e.g.* Maltrud and McClean 2005) was usually configured with 100 levels uniformly spaced over the 5000-m water column (Fig. 3.1), except for three experiments to test the effect of the vertical resolution:

ENB0.5_LV with 50 levels, ENB0.5_HV with 200 levels and ENB0.5_VHVH with 400 levels. The horizontal resolution is 1/4° in both longitude and latitude as in the JAMSTEC model, except in two experiments (ENB0.5_HH and ENB0.5_VHVH) where the resolution is doubled. The basin is rectangular extending from 20°S to 20°N and is 72° long (about 8000-km; Fig. 3.2).

The basin has vertical walls and irregular bottom topography. The topography was designed to reduce the reflection of inertia-gravity (IG) waves generated. It is generated using a white wavenumber spectrum smoothly band-passed between 2.5 and 10° in both the zonal (x) and meridional (y) direction. Its central horizontal wavelength and averaged vertical extent are 4° and 800 m, respectively, matching the typical zonal and vertical wavelength of the IG waves. Bottom friction is also added using a quadratic bottom drag formula with a dimensionless coefficient of 2.10^{-3}.

Biharmonic mixing is used in the horizontal with dissipative coefficients for momentum and tracers of -2.10^{-10} m^4/s. The vertical mixing scheme of Pacanowski and Philander (1981; PP81), dependent on the Richardson number Ri, has been chosen with background dissipative coefficients of 1.10^{-5} m^2/s for both momentum and tracers. Each simulation starts from an ocean at rest and a uniform stratification with a Brunt-Väisälä frequency of $N = 2 \times 10^{-3}$ s^{-1}. The initial potential temperature gradient is constant (Fig. 3.1) and restored at the surface with a time scale of a month and salinity is uniform and constant at 35 psu. A nonlinear equation of state is chosen, but because the stratification stays relatively constant throughout the numerical simulations and salinity is constant, the numerical solutions are little sensitive to that choice.

Each simulation is run for 10 years and annual or monthly averages are archived for the entire run. In addition, 5-day averages have also been archived for the last 3 years of the top 6 experiments of Table 3.1 to study the Yanai beam.

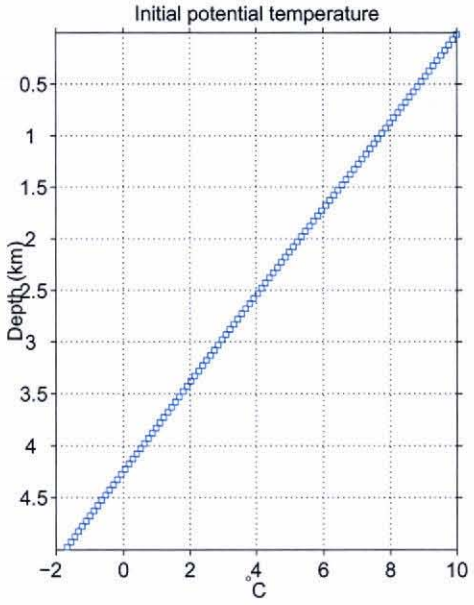

Figure 3.1: Initial potential temperature profile plotted on the 100-level grid.

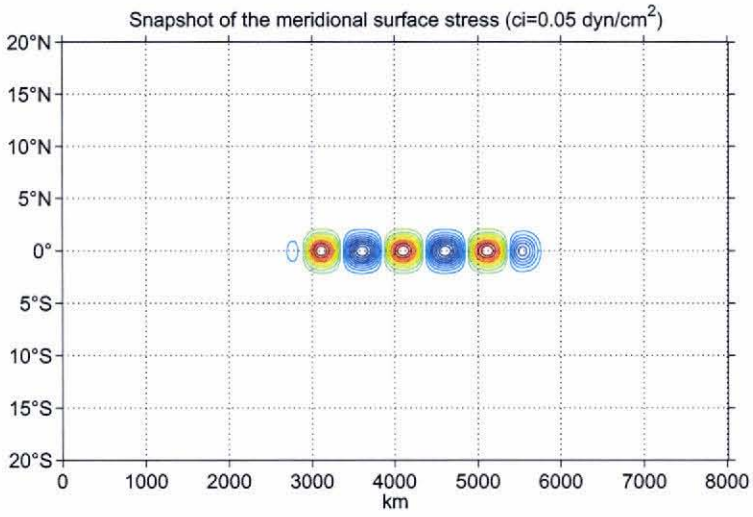

Figure 3.2: Snapshot of the meridional surface stress for the experiment EBB0.5. Contours every 0.05 dyn/cm^2.

In order to mimic the generation of monthly Yanai waves by instabilities of the equatorial current system, the ocean is forced with a stationary patch of meridional surface stress periodic in time and x (Fig. 3.2). The phase of the stress propagates westward within the patch in order to excite only westward-propagating waves. The patch is centered in the basin. It extends 20° in longitude with a 5° smoothed transition on each side. The meridional profile of the stress is a 6°-wide Blackman window centered on the equator, which excites primarily waves with a first-meridional mode such as the Yanai waves.

As discussed in Section 2.2, two types of spectrum in zonal wavenumber k and frequency ω are used: a broad-band (BB) and a narrow-band (NB), the former to mimic the variability and annual modulation of the instabilities, the latter to facilitate analysis of the dynamics. An example of time evolution for the two types of forcing is given in Fig. 3.3. Both types have a central period of 1.1 month and central zonal wavelength of 1000 km, which would excite a Yanai wave with a vertical wavelength of about 1700 m and a gravity wave speed C of about 53 cm s^{-1} (Fig. 3.4). The energy of such a Yanai wave reaches the 5000-m ocean bottom in about a year. The BB forcing is constructed using a white spectrum over an elliptical area A in frequency-wavenumber within $\Delta\omega = 5.1e-7$ 1/s and $\Delta k = 1.9e-6$ 1/m from the central frequency ω_0 and zonal wavenumber k_0, and zero everywhere else (Fig. 3.4). The BB forcing thus has frequencies varying from ω_{min} to ω_{max} corresponding to 43-day and 27-day periods, and negative zonal wavenumbers varying from k_{min} to k_{max} corresponding to 770-km and 1430-km zonal wavelengths; these ranges approximately span the ranges of observed values (see Section 2.2). The resulting temporal evolution (red in Fig. 3.3) is indeed qualitatively similar to that of the Yanai beam in the JAMSTEC model (Fig. 2.5b). The evolution in time of the BB forcing thus can be

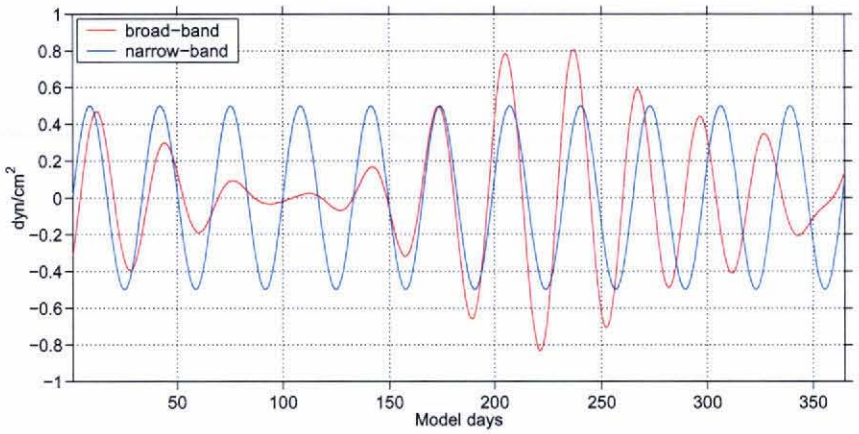

Figure 3.3: Time evolution of the BB and NB surface stress over the first year. Shown here are experiments EBB0.5 and ENB0.5, both with a standard deviation τ_0=0.5 dyn/cm^2.

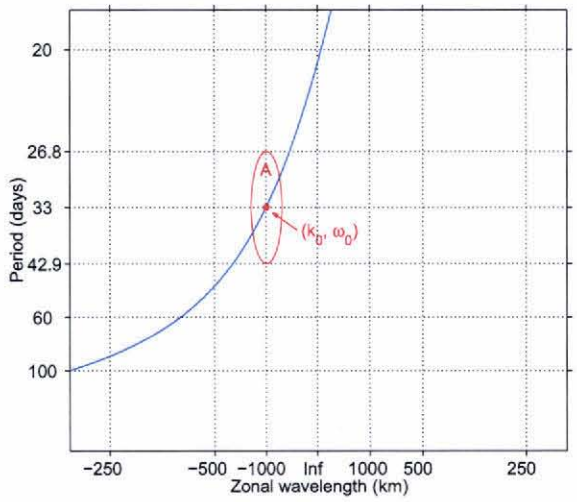

Figure 3.4: Dispersion relation for Yanai wave with a vertical wavelength of 1700 m (blue). Central zonal wavelength and period of the BB and NB surface stresses (red dot) and the area of the spectrum chosen to build the BB surface forcing (red ellipse).

name	type	τ (dyn/cm^2)	vertical levels	hor. resol. (in deg.)
EBB0.5	BB	τ_0 (0.5)	100	0.25
ENB0.5	NB	τ_0 (0.5)	100	0.25
ENB1	NB	$2\tau_0$ (1)	100	0.25
ENB0.25	NB	$\tau_0/2$ (0.25)	100	0.25
ENB0.125	NB	$\tau_0/4$ (0.125)	100	0.25
ENB0.05	NB	$\tau_0/10$ (0.05)	100	0.25
ENB0.5_LV	NB	τ_0 (0.5)	50	0.25
ENB0.5_HV	NB	τ_0 (0.5)	200	0.25
ENB0.5_HH	NB	τ_0 (0.5)	100	0.125
ENB0.5_VHVH	NB	τ_0 (0.5)	400	0.125
ENB0.05_HV	NB	$\tau_0/10$ (0.05)	200	0.25

Table 3.1: List of the different experiments with their name, the type (BB: broad-band or NB: narrow-band) of surface stress and its standard deviation τ, the number of vertical levels and the horizontal resolution. The top 6 experiments have identical resolution but different forcing while the next 4 have identical forcing but different resolution. The last experiment is the only one with different resolution *and* forcing. The code used to name each experiment is the following: 'E' stands for (numerical) experiment, followed by either 'BB' or 'NB' and by the value of τ. Optional suffixes include 'LV': low vertical resolution, 'HV': high vertical resolution, 'HH': high horizontal resolution and 'VHVH': very high vertical and horizontal resolution. Characteristics different from those in ENB0.5 are emphasized in bold green.

described by a finite sum of cosine functions,

$$\sum_n cos(k_n x - \omega_n t + \phi_n) \text{ for } t \geq 0, \tag{3.1}$$

with the pair (k_n, ω_n) within the area A and where ϕ_n, the phase for each pair, is chosen randomly. In the case of the NB forcing, the sum (3.1) is reduced to the single pair (k_0, ω_0) with $\phi_0 = 0$. It is not purely monochromatic, that is the spectrum has a peak with a non-vanishing width, because the forcing starts only at t=0.

A total of 11 experiments are presented here (Table 3.1). The first 6 experiments have identical vertical and horizontal resolution but different surface stresses. Experiment EBB0.5 is the only one with a BB forcing. Experiment ENB0.5 is similar to EBB0.5 except that it has NB forcing. The two are forced with a "standard" amplitude $\tau_0 = 0.5$ dyn/cm^2, and form the "standard runs" of the numerical investigation. Experiments ENB1, ENB0.25, ENB0.125 and ENB0.05 serve to study the sensitivity of solutions to the amplitude of the forcing. They are forced respectively with a "strong" ($2\tau_0 = 1$ dyn/cm^2), "moderate" ($\tau_0/2 = 0.25$ dyn/cm^2) and "weak" ($\tau_0/10 = 0.05$ dyn/cm^2 and $\tau_0/4 = 0.125$ dyn/cm^2) forcing. The next 4 experiments study the effect of changing the vertical and/or horizontal resolution, all with standard forcing. Experiments ENB0.5_LV and ENB0.5_HV serve to study the sensitivity to the vertical resolution, with half and twice the standard resolution respectively, while experiment ENB0.5_HH shows the effect of doubling the horizontal resolution from 1/4° to 1/8°. Experiment ENB0.5_VHVH combines very high vertical and horizontal resolution, with 400 levels and 1/8°. Finally, because a unique EDJ-like structure appears in ENB0.05, the last experiment ENB0.05_HV is performed, forced with the same weak forcing as in ENB0.05 but with twice the vertical resolution in order to test the robustness of these EDJs.

3.3 High-frequency variability

In this section, the high-frequency variability directly forced by the surface stress is studied in the top 6 experiments of Table 3.1. A description of other high-frequency motions not directly forced by the surface stress is deferred to Appendix A.1.

The high-frequency variability dominates the meridional motion V at the equator, and thus serves as a measure for that variability. In all experiments, a beam of Yanai waves is formed (Fig. 3.5), qualitatively similar to the one observed in the JAMSTEC model (Fig. 2.5a). The vertical wavelength is about 1700 m, with a phase propagating upward and to the west. Its energy propagates downward and eastward, reaching the bottom in about a year. With both BB (EBB0.5) and NB (ENB0.5 to ENB0.05) forcing, the beam is well-defined all over the water column and its slope is consistent with linear theory (Fig. 3.5; thick dashed lines). Due to the frequency range with BB forcing, the beam in EBB0.5 is expected to widen with depth (two light dashed lines in Fig. 3.5a). In the following, the thick dashed lines plotted in Fig. 3.5 serve also to define the locations of the two edges of the beam within which zonal averages are taken.

In all experiments, the beam encounters the bottom and the eastern boundary. Because of the topography, only part of the Yanai wave energy is reflected; it thens propagates upward and to the east and reaches the eastern boundary below about 2250 m. At the eastern boundary, the Yanai wave reflects into coastal Kelvin waves as expected by theory (McCreary 1984). These coastal Kelvin waves propagate all along the basin boundaries and in theory would reach the equator at the western boundary in less than a year. In all the experiments, however, little energy is found there (see for instance in Fig. 3.5); the coastal Kelvin waves have a Rossby radius of less than 0.1° along the northern and southern boundaries and are rapidly dissipated by the explicit lateral mixing.

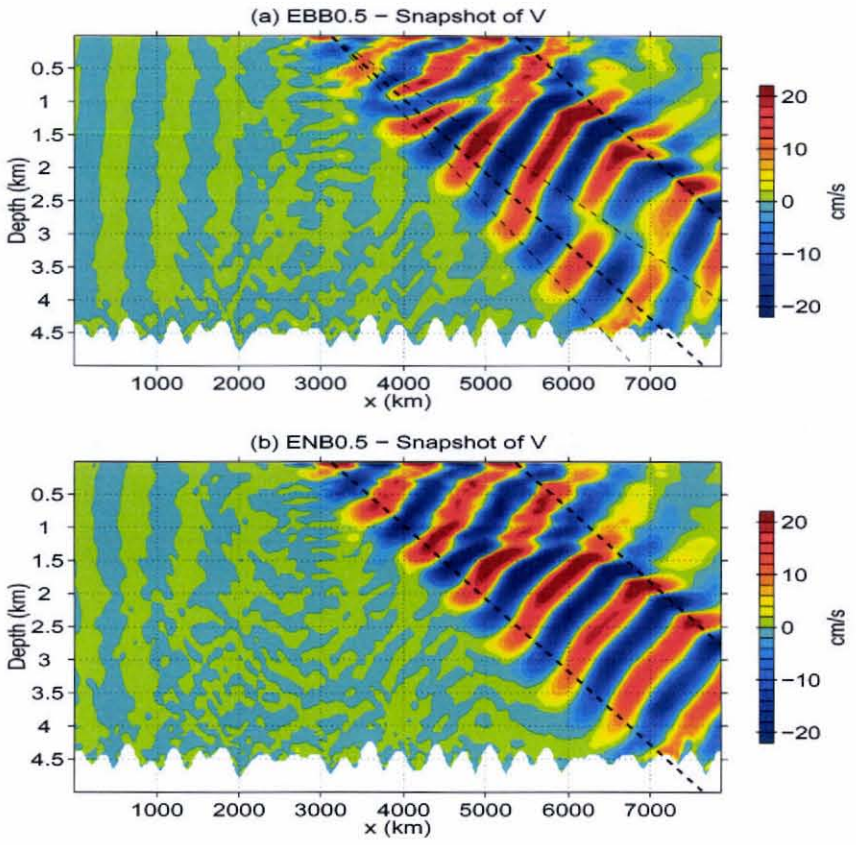

Figure 3.5: Equatorial V on Jan. 1, year 01 in (a) EBB0.5 and (b) ENB0.5. The thick dashed lines show the theoretical ray slope for a Yanai wave of frequency ω_0 within a stratification N. The additional light dashed lines in (a) are for waves with frequency ω_{min} and ω_{max}. With uniform stratification, the higher the frequency, the steeper the slope.

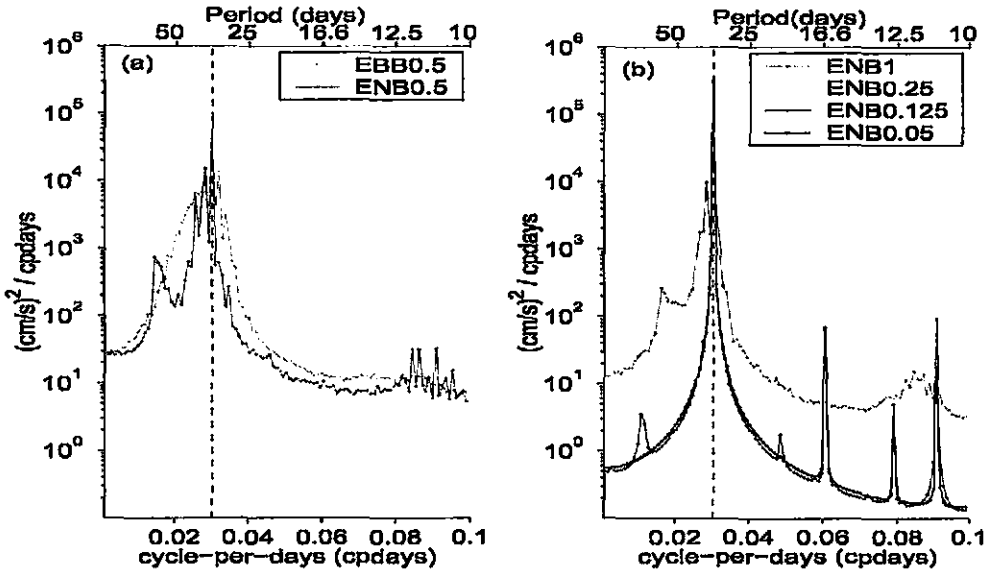

Figure 3.6: Averaged PSD in equatorial V in (a) EBB0.5 and ENB0.5 and (b) ENB1, ENB0.25, ENB0.125 and ENB0.05. In (b) the spectra have been normalized by τ_0/τ. The spectra have been obtained over model years 7–9, and averaged between 1000 and 3000 m depth and between the two edges of the beam. The dashed line indicates the 1.1-month period.

The meridional velocity V at the equator characterizes the high-frequency variability and its spectrum has in all experiments its largest peak centered at the 1.1-month period (Fig. 3.6). Vertical profiles of beam amplitude $\mathcal{V}(z)$ can then be defined as the amplitude of equatorial V at this period zonally averaged between the two edges of the beam. The dimensionless quantity $\epsilon(z) = \mathcal{V}(z)/\mathcal{C}$, where $\mathcal{C}$ is the gravity wave speed of the central Yanai wave introduced in Section 3.2, is a measure of the amount of nonlinearity and can be considered as a meridional Froude number (Gill 1974; Hua08).

Profiles of $\epsilon(z)$ for ENB0.05 to ENB1 are shown in Fig. 3.7a. For weak forcing (ENB0.05 and ENB0.125), the profiles are nearly constant with depth and the

Froude number is less than 0.15, suggesting that nonlinearities are weak. At moderate (ENB0.25), standard (ENB0.5) and strong (ENB1) forcing, the profiles are significantly attenuated with depth and the stronger the forcing, the stronger the attenuation. In ENB1, the Froude number reaches 0.5 suggesting that nonlinear terms are similar in magnitude.

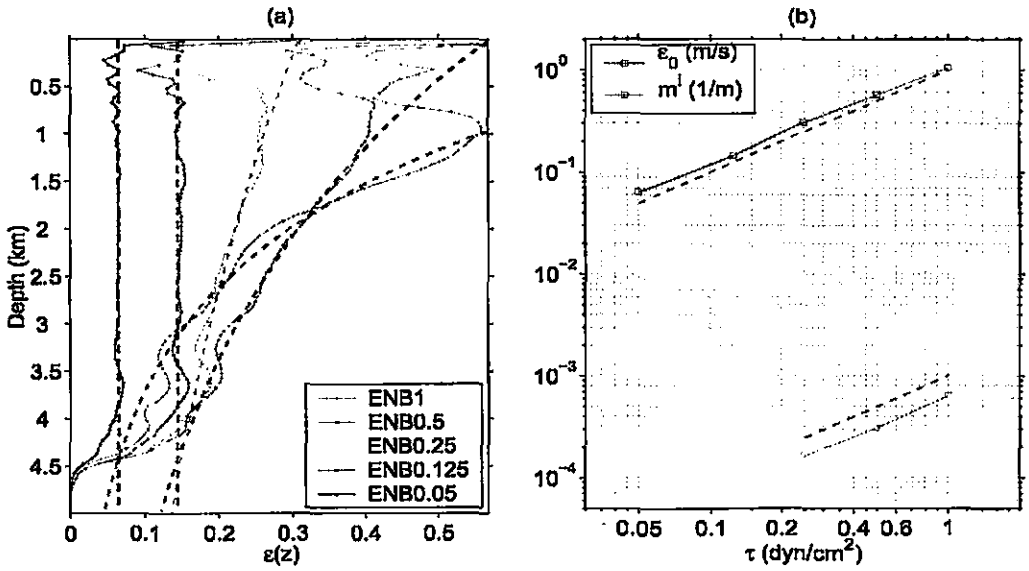

Figure 3.7: (a) Vertical profiles of beam amplitude $\mathcal{V}(z)$ in the NB runs. To construct these profiles, the amplitude of V at the 1.1-month period has been extracted along the equator and averaged within the beam. In dashed lines are plotted the exponential fits (see text). (b) Dimensionless amplitude ϵ_0 at $z = 0$ (blue) and damping rate m^i (red) plotted against the standard deviation τ of the surface stress. The axes are logarithmic and the dashed dark lines show the slopes corresponding to linear relationships. m^i in ENB0.05 and ENB0.125 are found to be virtually zero and thus do not appear in (b).

The cause of the attenuation as well as its increase with the forcing amplitude is related to the presence of other low and high-frequencies waves, the structure and

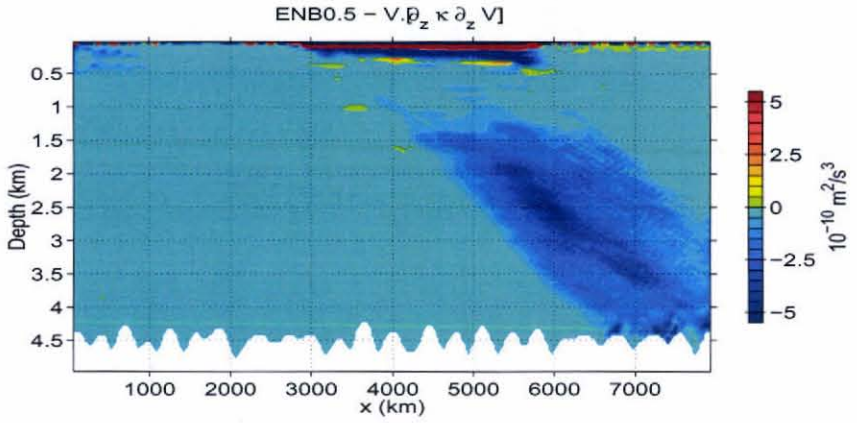

Figure 3.8: Work of the vertical momentum mixing in the meridional direction at the equator and averaged over years 7–9 in ENB0.5.

generation of which are discussed in Appendix A.1. In particular, it is argued that these waves are the result of several cascades of nonlinear interactions starting from the Yanai beam. These cascades would be responsible for the irreversible loss of the energy of the beam toward small-scale waves where it is dissipated. Most of the dissipation indeed occurs within the beam mainly *via* vertical mixing (Fig. 3.8). Such transfer is expected to be more efficient for stronger-amplitude Yanai beam, consistent with the increase of beam dissipation with forcing amplitude.

The draining of energy from the Yanai beam *via* nonlinear interactions can be parameterized as an "effective dissipation". The attenuation of the amplitude with depth is approximated by an exponential decay (dashed lines in Fig. 3.7a):

$$\epsilon(z) \approx \epsilon_0 e^{-m^i z} \tag{3.2}$$

where ϵ_0 is the dimensionless amplitude of the exponential profile at $z = 0$ and m^i is the damping rate with depth. These exponential profiles correspond to the approximate analytical solution of the profile of a beam of Yanai waves *dissipated by Rayleigh friction* and discussed further in Chapter 4. In this case, m^i corresponds

also to the imaginary part of the vertical wavenumber of the central Yanai wave forming the beam. The damping rate m^i varies proportionally with the Rayleigh friction coefficient r in the present regime of frequency and attenuation ($r \ll \omega$; see Appendix B.1).

The dimensionless amplitude ϵ_0 varies almost linearly with the forcing amplitude (Fig. 3.7b). This means that if there were no loss of energy in the vertical, the amplitude of the wave would be proportional to the forcing. The damping rate m^i (and the strength of the Rayleigh friction r) is virtually zero for weak forcing (ENB0.05 and ENB0.125; Fig. 3.7b) and then increases with the forcing amplitude (ENB0.25, ENB0.5 and ENB1). Surprisingly, the increase seems also to be almost linear in the forcing. Thus the effective dissipation acting on the beam in these three runs can be parameterized by the horizontal momentum dissipation:

$$\vec{\mathcal{D}} = -r(\tau)\vec{u} \tag{3.3}$$

where $\vec{u}$ is the horizontal velocity field and $r(\tau)$ is a linear function of forcing amplitude. It is remarkable that the effective dissipation, possibly being the end result of a series of nonlinear processes can be parameterized so simply. Chapter 4 develops the analytical solution of a Yanai wave damped by $\vec{\mathcal{D}}$ and shows that this damping suffices to explain the generation of the mean currents described in Section 3.4.

Another effect of increasing the forcing amplitude is a broadening of the meridional profile of the Yanai beam. In Fig. 3.9 are plotted the normalized meridional profiles of the amplitude of equatorial V at the 1.1-month and at 2000 m in ENB0.5, ENB0.25 and ENB0.05. They are compared to a profile obtained from the analytical solution of the damped Yanai beam (dashed black line): only one analytical profile is plotted because, unlike in the numerical experiments, it is nearly independent of the forcing (see Appendix B.1). While the profile with weak forcing (ENB0.05) fits well the analytical solution, those with moderate (ENB0.25) and standard (ENB0.5)

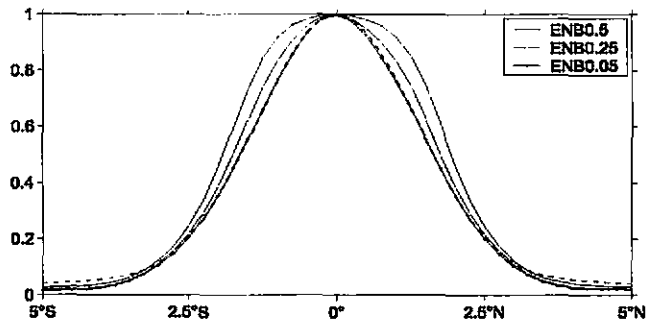

Figure 3.9: Meridional profile of the amplitude of equatorial V at the 1.1-month period, 2000 m depth and averaged within the beam in ENB0.5, ENB0.25 and ENB0.05. The profiles have been normalized by their maximum amplitude. The dashed black line shows the same profile but for one analytical solution of the damped Yanai beam.

forcing widen together with a flattening of the tip of the jet. The stronger the wave, the larger the effect, suggesting that some type of nonlinear process is occuring but it is not clear which type and how. Furthermore, although the effect is relatively small, it cannot be explained by the same dissipative scheme suggested for the vertical decay of the beam and will thus not be taken into account in the analytical solutions of Chapter 4.

Finally, experiment ENB0.05 with weak forcing is the only experiment where another wave directly forced by the surface forcing is found. A snapshot of equatorial V at the beginning of year 7 and for small-vertical scales is plotted in Fig. 3.10. The excited wave is close to a second-meridional-mode IG wave with near-zero horizontal group velocity. Using the dispersion relation of such a wave with the central frequency and zonal wavenumber of the forcing, one finds a vertical wavelength of about 130 m, shorter than the 190-m wavelength observed in ENB0.05. In a similar run but with twice the vertical resolution (ENB0.05_HV), a similar wave is also excited except that its vertical wavelength (160 m) and its meridional structure are closer to those

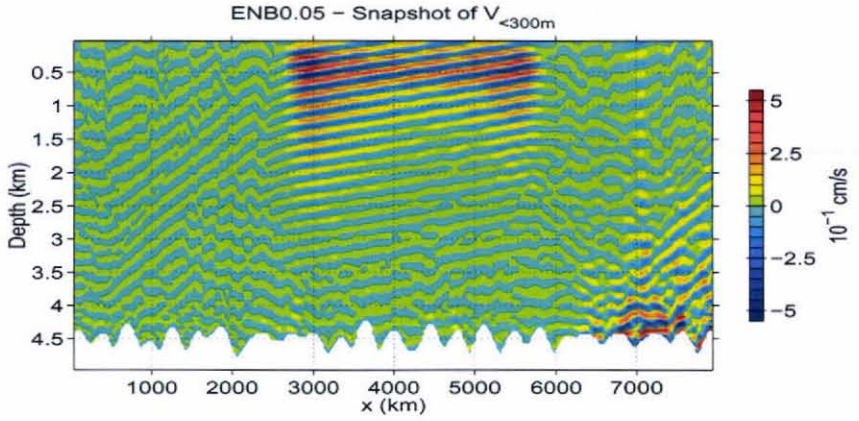

Figure 3.10: Equatorial V with vertical wavelength shorter than 300 m on Jan. 1, year 07 in ENB0.05. The vertical profiles have been smoothed at top and bottom with a 6% cosine-taper.

of the theoretical second-meridional IG wave, suggesting that even higher resolution might be needed to reproduce the wave accurately. In both cases, however, the wave energy is propagating nearly vertically but at such a slow rate (about 950 m/year) that it appears to be dissipated before reaching the bottom, thus precluding the formation of a vertical mode.

The IG wave is shown in Section 3.4.2 and Appendix A.2 to interact with the Yanai beam and generate a structure resembling the EDJs. It is not clear why the wave is absent in experiments with stronger forcing. The stronger surface currents may interfere with its formation or downward propagation, or *via* the deformation of the upper stratification (not shown).

3.4 Low-frequency motion

3.4.1 Standard runs

Significant mean zonal currents are obtained in the standard runs EBB0.5 and ENB0.5. These currents share qualitative and quantitative features with the TEJs of the observations and JAMSTEC model. In the following, only flows below 1000 m are considered: their mean, defined as the temporal average over the last three years of each run (model years 7 to 9), and their low-frequency (after smoothing over a 6-month period) components obtained in EBB0.5 and ENB0.5 are described and compared to the observations and JAMSTEC.

Mean flows resembling the EDJs are also obtained within the upper 1000 m. It is not clear, however, if these currents are genuine EDJs, and their description is therefore deferred to Appendix A.2.

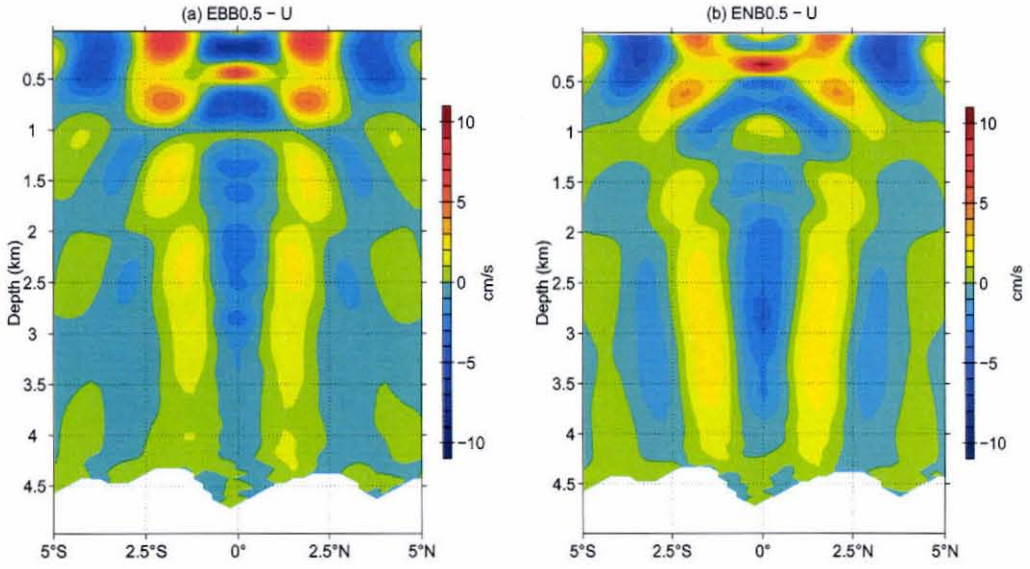

Figure 3.11: Mean zonal velocity U at $x = 2000$ km and averaged over model years 7–9 in experiment in (a) EBB0.5 and (b) ENB0.5.

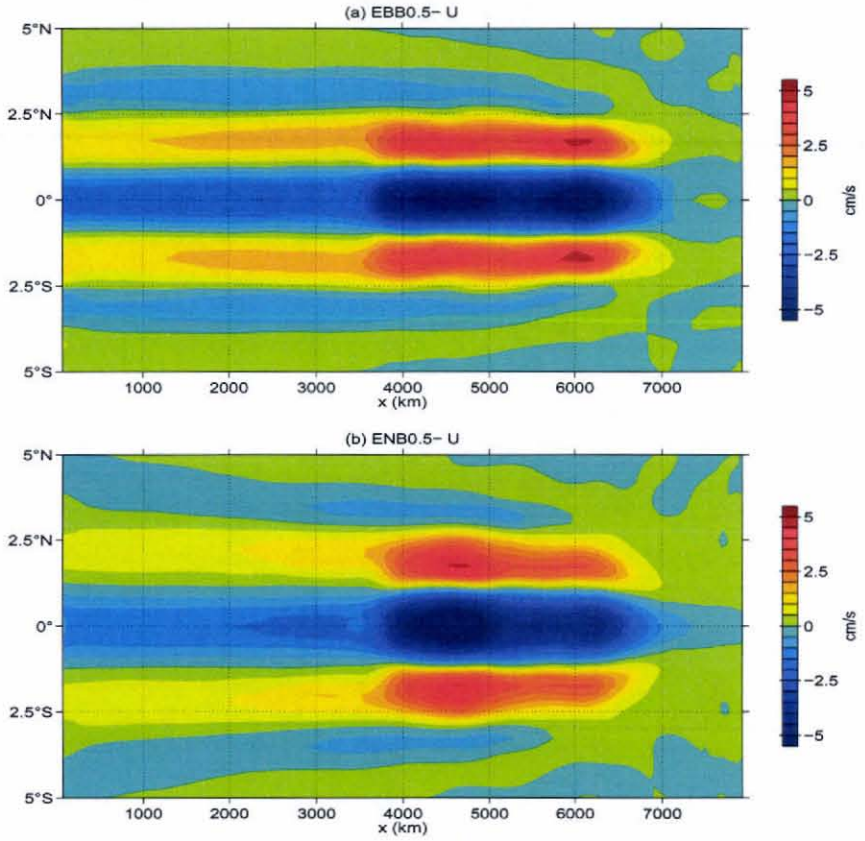

Figure 3.12: Mean U along-beam averaged (see text) between z_{max} and z_{min} in (a) EBB0.5 and (b) ENB0.5 over model years 7–9.

The mean zonal velocity U in experiments EBB0.5 and ENB0.5 at a meridional section west of the Yanai beam ($x = 2000$ km) is plotted in Fig. 3.11. Below 1000 m, there is a set of large-vertical-scale currents alternating with latitude which are comparable to the TEJs. It is composed of westward flows near 3° from the equator, eastward flows near 2° from the equator and a westward equatorial current. These TEJs are present throughout the water column except around 1000 m where the currents reverse in sign. In particular, they extend down to the bottom, unlike the currents in the observations and JAMSTEC which are found only above 2000 m

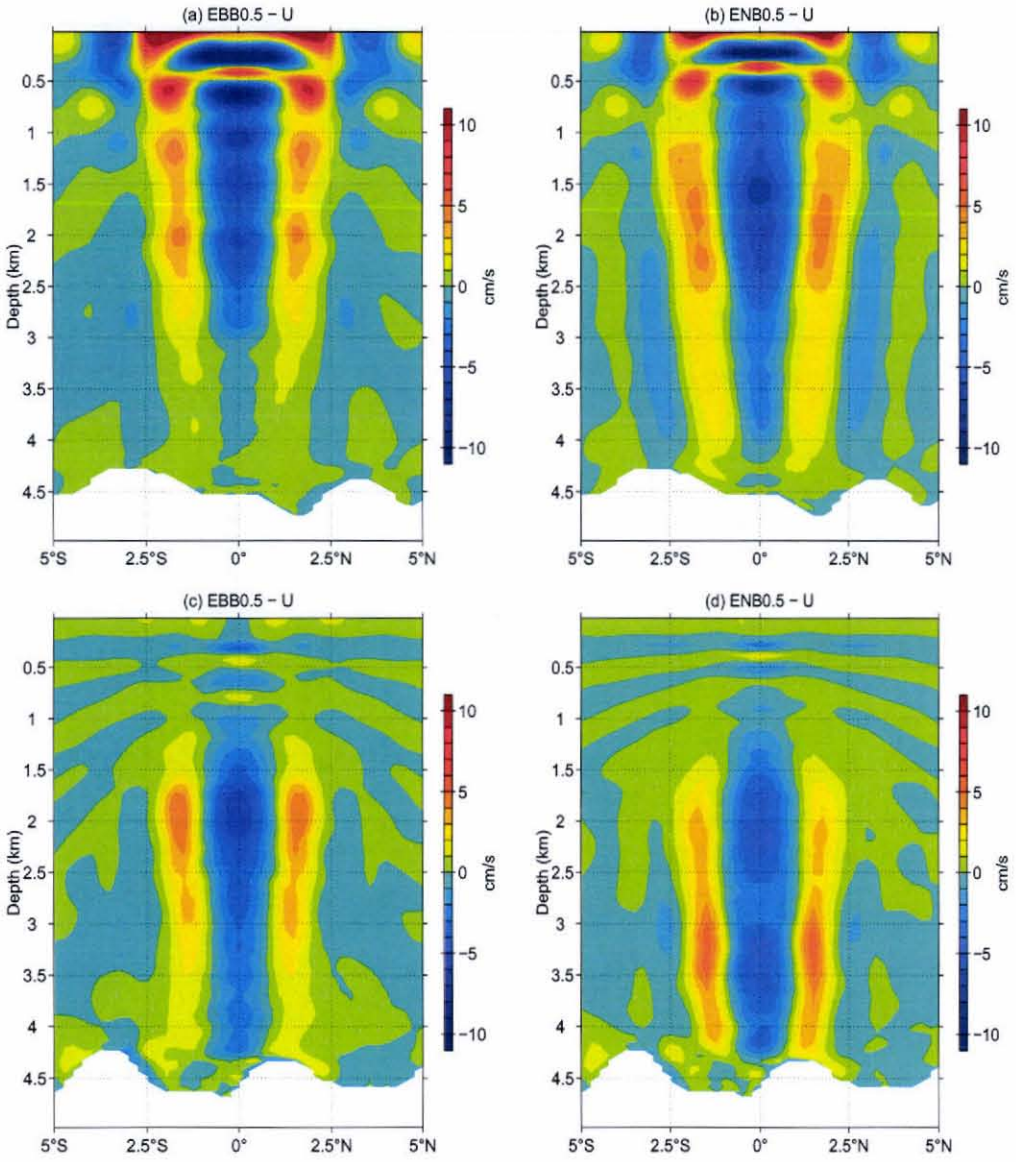

Figure 3.13: Mean U averaged over model years 7–9 in EBB0.5 and ENB0.5 at $x = 5000$ km in (a) and (b) and at $x = 7500$ km in (c) and (d).

(Fig. 1.1). The standard deviation of the mean flow at this longitude is nearly uniform in the vertical and is maximum at the equator where it never exceeds 5 cm s^{-1} (not shown); the ratio of the magnitude of the mean currents to that of their variability is, however, about the same as that in the observations and the JAMSTEC model of Fig. 1.1.

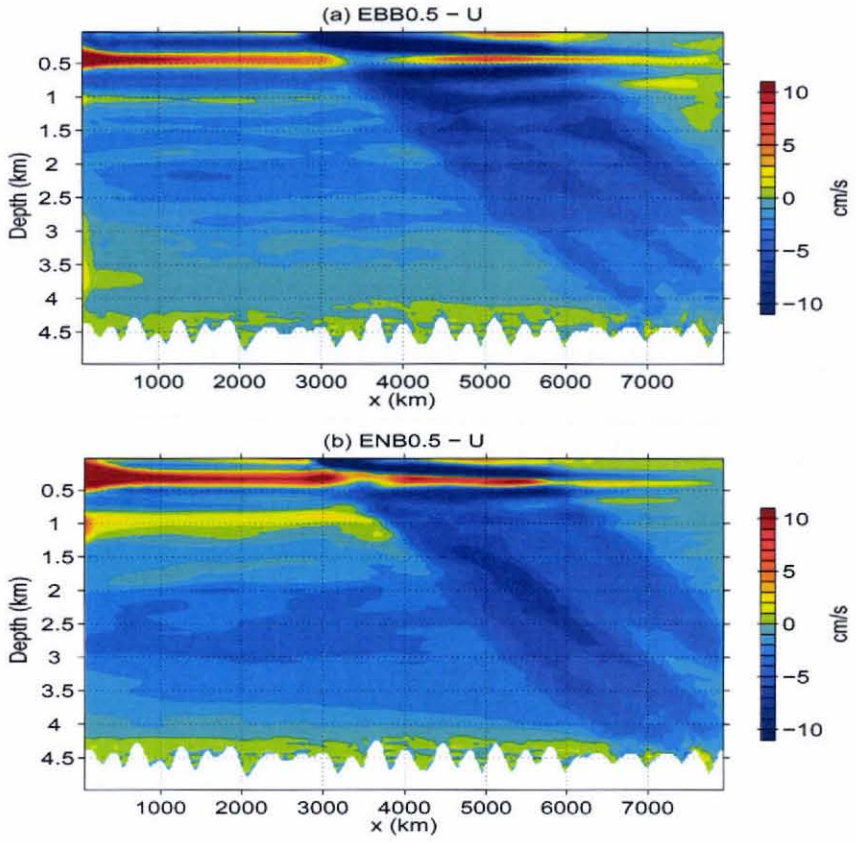

Figure 3.14: Mean equatorial U in (a) EBB0.5 and (b) ENB0.5 over model years 7–9.

The TEJs in EBB0.5 and ENB0.5 are found everywhere within and to the west of the Yanai beam, but not to its east. They are thus basin-scale currents consistent with observations and JAMSTEC. Hereafter, an "along-beam" average is defined

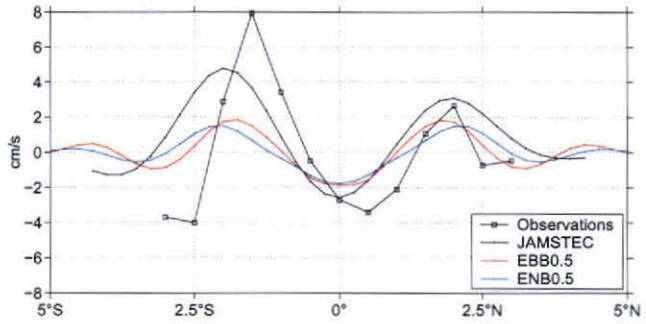

Figure 3.15: Mean U: from the observations at 159°W of Fig. 1.1a but averaged vertically between 400 and 1500 m, from JAMSTEC at 159°W calculated as in Fig. 2.1a and from EBB0.5 and ENB0.5 at $x = 3000$ km over model years 7–9 and after being averaged along the beam between z_{max} and z_{min} depth.

between $z_{max} = -1000$ and $z_{min} = -2250$ m where the average is performed along the main direction of propagation of the beam given by the thick dashed lines of Fig. 3.5b; the subsequent averaged is then plotted *versus* x (z_{max}). Such average between z_{max} and z_{min} reveals the horizontal structure of the TEJs as shown in Fig. 3.12. To the west of the beam, the circulation is zonally coherent with a magnitude outside the western boundary layer of about 2–3 cm s^{-1}. The TEJs within the beam (from about $x = 4000$ to 6300 km) more than double in amplitude and, unlike those in the west, their vertical structure is uninterrupted from 500 m down to the bottom (see at $x = 5000$ km in Fig. 3.13a and b). To the east of the beam, no significant mean flows are found in either EBB0.5 or ENB0.5. This is revealed for instance in Fig. 3.12 as well as in sections at $x = 7500$ km, the upper 1500 m of which is to the east of the beam (Figs. 3.13c and d). Finally, an interesting property appearing at all longitudes except near the eastern boundary is that the meridional scale of the TEJs seems to vary with their strength: the stronger the TEJs, the larger their meridional scale, seen for instance in the vertical sections of Figs. 3.11 and 3.13a and b. Similar

observations have been made in the Atlantic Ocean by Gouriou *et al.* (2001).

The equatorial section of the mean U in EBB0.5 and ENB0.5 illustrates well the zonal and vertical structure of the TEJs below z_{max} (Fig. 3.14). In particular, the westward equatorial TEJ is found maximum within the Yanai beam along bands of maxima nearly parallel to the direction of the beam. The maxima are generally shallower in EBB0.5 than in ENB0.5. To the west of the beam, the flow is weaker and its maximum amplitude is reached between 2000 and 3000 m in both experiments.

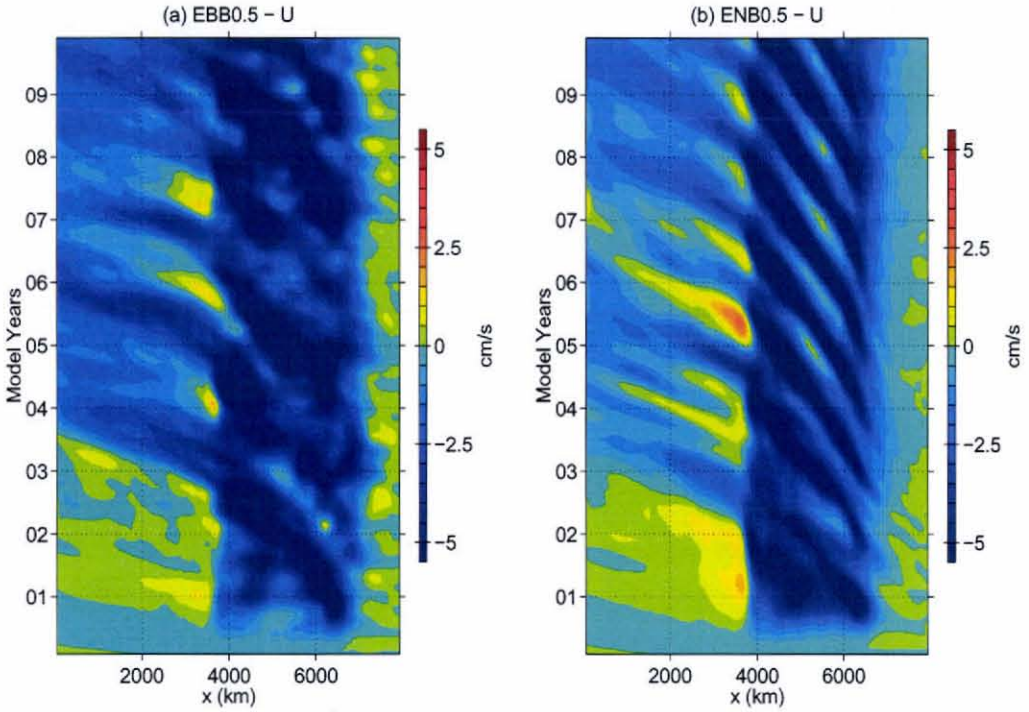

Figure 3.16: Zonal velocity U at the equator along-beam averaged between z_{max} and z_{min} in (a) EBB0.5 and (b) ENB0.5. The monthly-averaged time series have been smoothed by a running Blackman filter with a 6-month width.

The meridional structure of the TEJs to the west of the beam in EBB0.5 and ENB0.5 is qualitatively similar to that in the observations and JAMSTEC but they are in general weaker and there are differences in the exact position of the jets

(Fig. 3.15). The northern eastward TEJ in both EBB0.5 and ENB0.5 are consistent in magnitude and location with the observations. The southern eastward TEJ is consistent with the one in JAMSTEC in latitude, but is shifted south relative to the observations; the magnitude in both experiments is weaker by a factor of 4 than the observed jet. The magnitude of the equatorial westward TEJ is weaker by a factor of 2 than the observed one. Finally, the off-equatorial TEJs are as weak as for JAMSTEC compared to the observations, and their positions vary from one simulation to another. Although the jets within the beam have the same positions as those to its west in EBB0.5 and ENB0.5, their magnitude is 2 to 3 times larger: the comparison with the observations and JAMSTEC in term of magnitude is thus better for all TEJs.

The low-frequency component of the circulation is defined as the monthy-averaged time series smoothed by a running Blackman filter with a 6-month width. The low-frequency component of the westward TEJ at the equator is studied as a proxy for the low-frequency variability of the TEJs in general. Its along-beam average between z_{max} and z_{min} all along the equator is plotted in Fig. 3.16, and its vertical profile within the beam ($x = 5000$ km) is plotted in Fig. 3.17 for the two experiments.

In both EBB0.5 and ENB0.5, the zonal flow reaches a statistically steady state within 4 years (Fig. 3.16). The flow within the beam is set up within a year at 1000 m and 4 years below 3000 m (Fig. 3.17). To the west of the beam, the initial response of the ocean is a westward-propagating eastward current but after year 4, it is mostly replaced by the westward flow (Fig. 3.16). There the variability is dominated in both cases by westward-propagating anomalies, suggesting that the flow is set up by Rossby waves, as in the case of the classic Sverdrup circulation.

In both experiments, the low-frequency motion within the beam appears as a strong near-annual oscillation. Phase propagates westward (Fig. 3.16) and down-

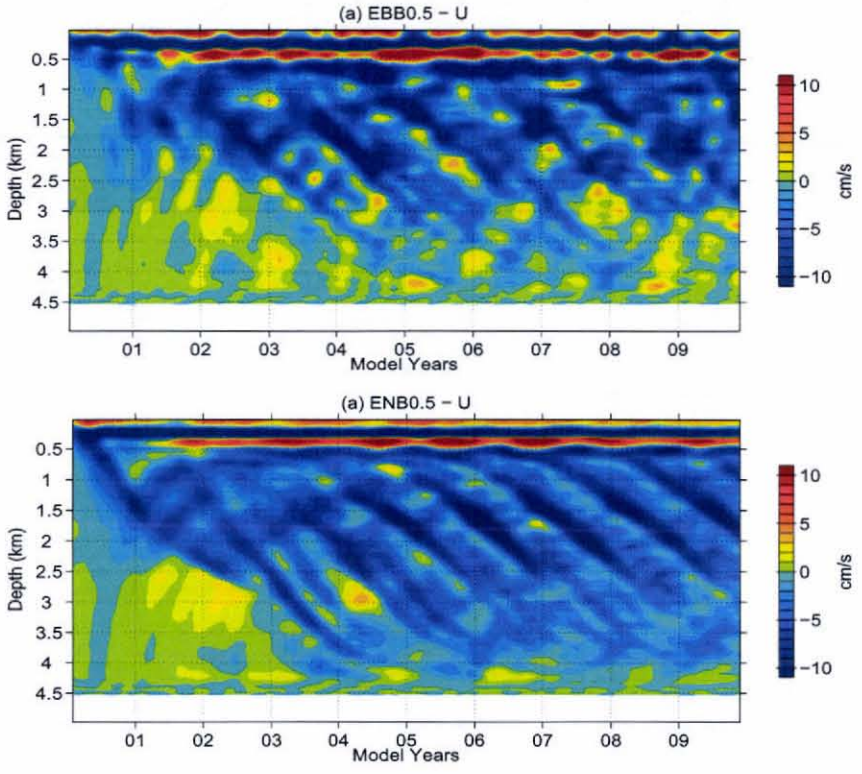

Figure 3.17: Zonal velocity U at $x = 5000$ km and on the equator in (a) EBB0.5 and (b) ENB0.5. The monthly-averaged time series have been smoothed by a running Blackman filter with a 6-month width.

ward (Fig. 3.17), suggesting a Rossby wave with energy propagating *upward*. The oscillation is irregular with a period of about 1.3 year in ENB1 and regular with a period of about 1 year in ENB0.5. In the latter case, the zonal and vertical wavelengths are respectively about the same as and half those of the central Yanai wave forming the beam suggesting westward-energy propagation. Together with the meridional profile of the velocity field, such characteristics thus point toward a long first-meridional Rossby wave. The energy seems, however, to follow about the same angle as the Yanai beam (Fig. 3.18): only a Rossby wave with a meridional mode 5 could follow that angle inconsistent with the actual meridional profile. One has to

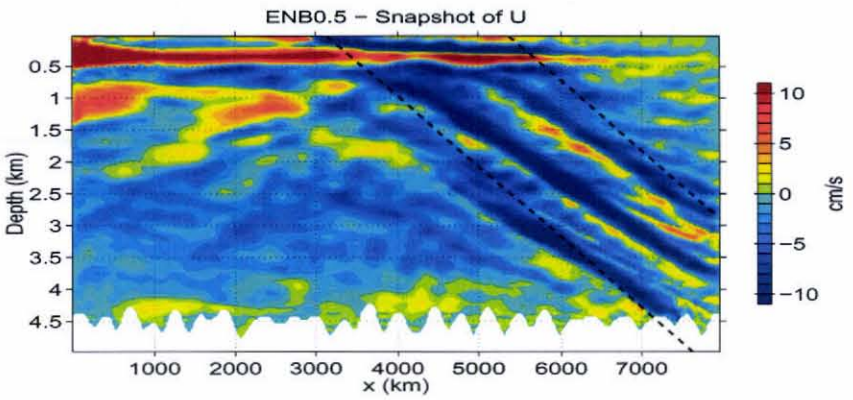

Figure 3.18: Monthly-averaged equatorial U in ENB0.5 during January 07.

conclude that the oscillation is not a free wave of the system but is rather a locally forced response.

Other forced motions have been identified. It is argued in Appendix A.1 that the low-frequency motion plays the central role in the transfer of energy from the Yanai beam toward these other motions. It is not clear, however, why such motion arises and more work is needed to answer this question.

3.4.2 Sensitivity to forcing amplitude

Mean flows similar to those in EBB0.5 and ENB0.5 are also obtained in experiments ENB1 to ENB0.05 (Fig. 3.20) where the strength of the forcing is changed. The main tendencies found are that the TEJs have an amplitude increasing quasi-quadratically with the amplitude of the beam and they are found to the west of the beam only when the beam amplitude is large enough.

Along with the zonal extent, the amplitude of the TEJs is the characteristic most sensitive to the amplitude of the forcing. Because it is believed that the mean flows are triggered by the second-order rectification of the Yanai beam, the amplitude of the westward equatorial TEJ and northern eastward TEJ is plotted in Fig. 3.19a against

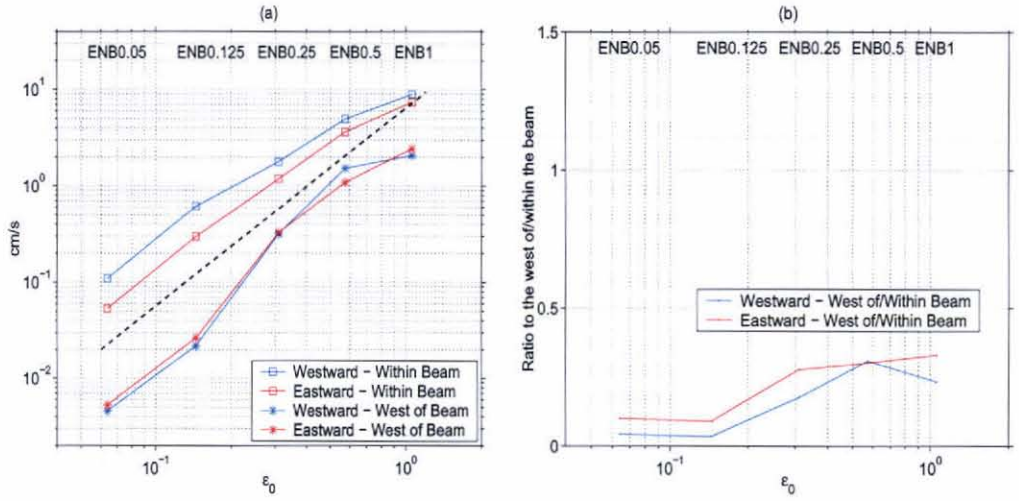

Figure 3.19: (a) Amplitude of the TEJs within (square) and to the west of (star) the beam in the numerical solutions ENB0.05 to ENB1. It is defined as the maximum speed of the velocity along-beam averaged between z_{max} and z_{min} and between $x =$ 1000 and 3000 km for the region to the west of the beam and between the two edges of the beam for the region within. (b) Ratio of the amplitude of the TEJs to the west of/within the beam. In both panels, red corresponds to the eastward TEJ north of 1°N and blue to the westward equatorial TEJ within 1° from the equator. The dashed line in (a) shows the slope corresponding to a quadratic evolution.

the dimensionless amplitude of the beam ϵ_0 of Fig. 3.7b. Both TEJs strengthen with the beam amplitude within and to the west of the beam. Within the beam, the increase is close to a quadratic law; for stronger forcing, the amplitude of the TEJs is weaker than expected based on a quadratic relationship. In Chapter 4, it is shown that such deviation from a quadratic law is due to the increase of the dissipation with the beam amplitude: if the dissipation would have been constant between the experiments, the evolution would have been quadratic. The evolution of the TEJs outside the beam is more erratic although it loosely follows a quadratic law

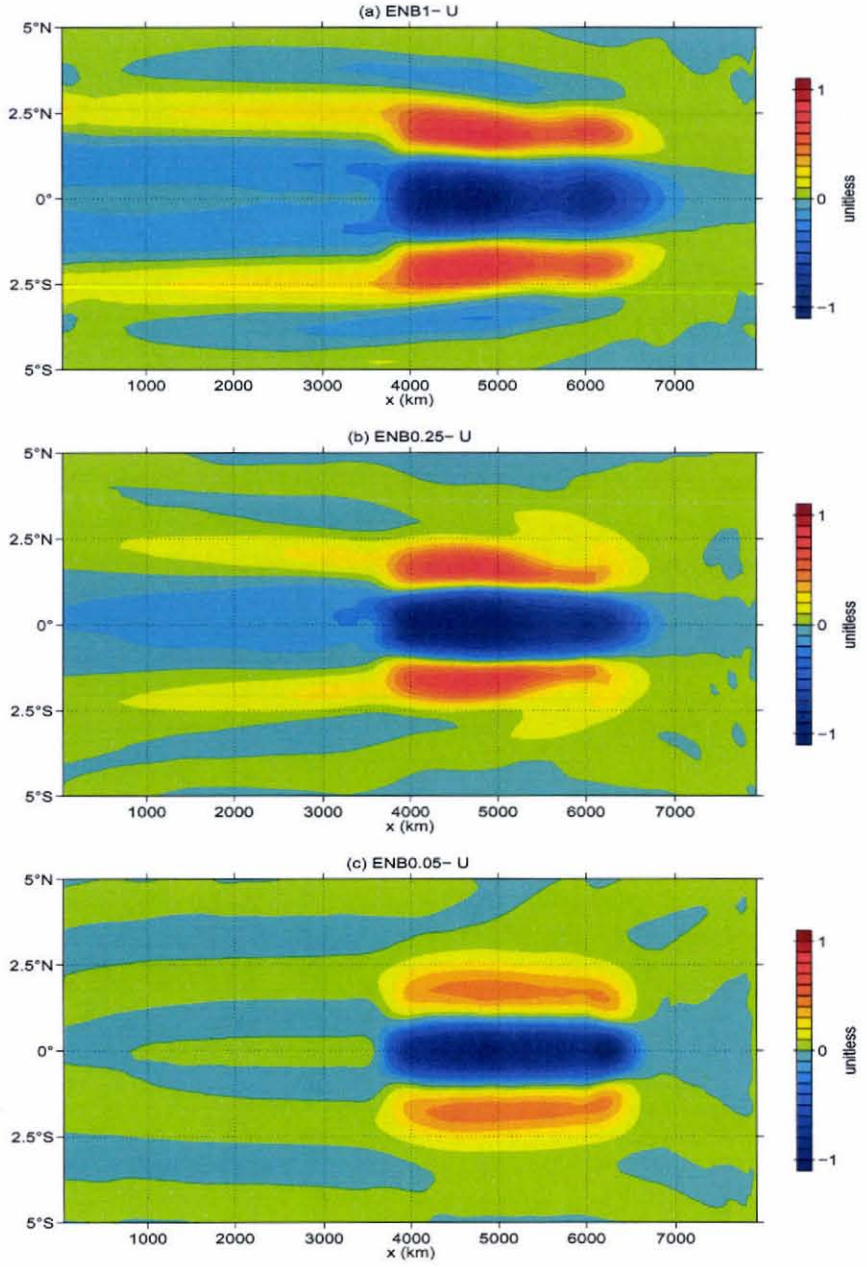

Figure 3.20: Mean U over model years 7–9 and along-beam averaged between z_{max} and z_{min} in (a) ENB1, (b) ENB0.25 and (c) ENB0.05. The averaged velocity has been normalized by its maximum amplitude.

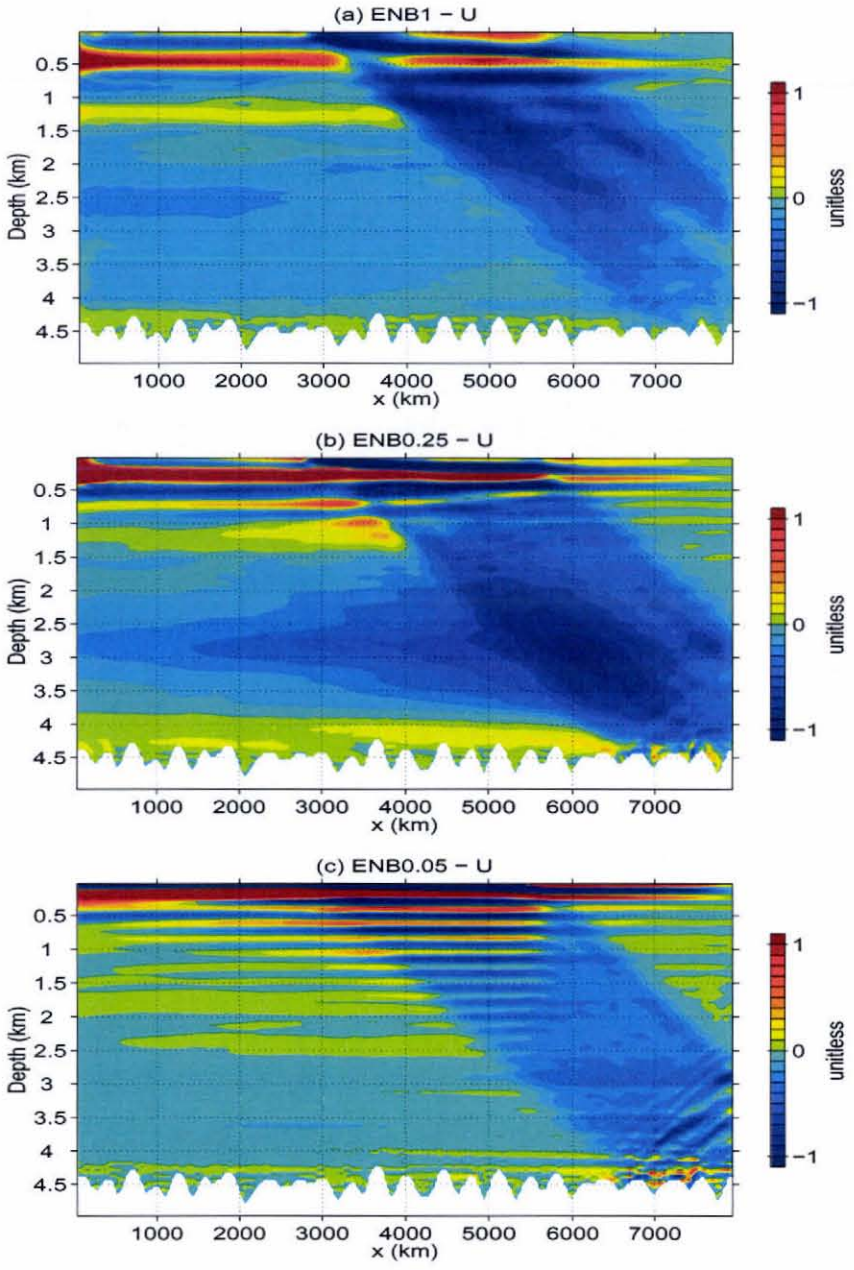

Figure 3.21: Mean equatorial U normalized by its maximum absolute value between 1000 and 3000 m in (a) ENB1, (b) ENB0.25 and (c) ENB0.05 over model years 7–9.

as well. The weak amplitudes found west of the beam with weak forcing (ENB0.05 and ENB0.125) do not correspond to mean flows resembling the TEJs (Fig. 3.20c) and may be the result of rectifications involving other high-frequency variability such as the weak barotropic signal found in the west in all simulations (Fig. 3.5). The amplitude of the flows to the west of the beam relative to those within the beam globally increases with the beam amplitude (Fig. 3.19b): it is about 5–10% for the experiments with weak forcing, increasing to 15–30% for the experiments with moderate, standard and strong forcing. The low ratio found with weak forcing is again consistent with the idea that the mean flows found to the west of the beam in these cases are not genuine TEJs.

The zonal structure is the second most sensitive characteristic to beam amplitude (Fig. 3.20). The TEJs are found to the west of the beam only in the experiments with moderate, standard and strong forcing. They are thus obtained only when the beam amplitude is strong enough, that is when the Froude number reaches about 1/4.

The vertical structure of the westward equatorial TEJ varies significantly between the experiments (Fig. 3.21). Although bands of maximum speed within the beam and nearly parallel to the direction of the beam are still obtained in the experiments with moderate, standard and strong forcing, their locations and width vary, being shallower and finer, for instance, with strong forcing. These bands are, however, absent in the experiments with weak forcing (ENB0.05 and ENB0.125). The westward equatorial TEJ to the west of the beam is found only in the experiments with moderate, standard and strong forcing. In all these, the maximum is reached between 2000 and 3000 m but it varies in zonal extent and intensity; for instance, a tongue of maximum speed extending from the beam to the western boundary near 2750 m depth is observed in ENB0.25 but not in ENB0.5 and ENB1.

In experiment ENB0.05, virtually no TEJs are found to the west of the beam. However, the EDJ-like structure observed only near the surface in the other experiments extends in ENB0.05 as deep as 2000 m. This structure is described in more detail in Appendix A.2.

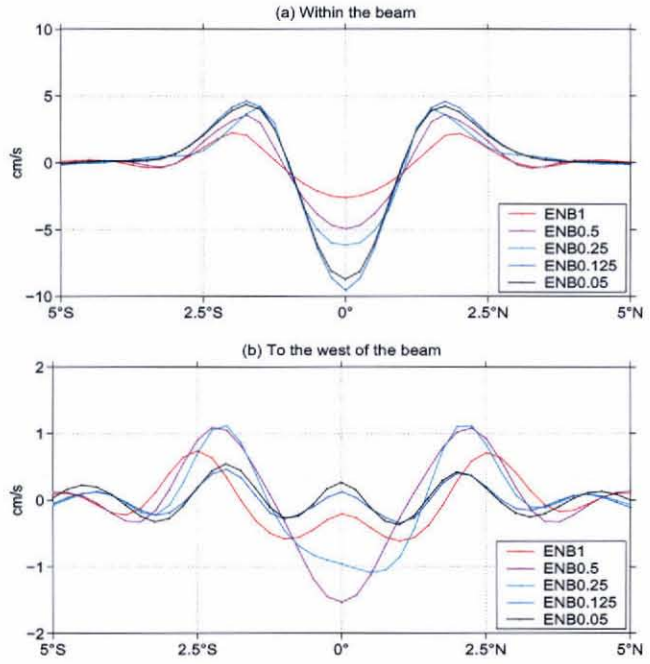

Figure 3.22: Mean U from ENB0.05 to ENB1 along-beam averaged between z_{max} and z_{min}, then averaged over model years 7–9 and within the beam in (a), and between $x = 1000$ and 3000 km in (b). Profiles have been multiplied by $(\epsilon_{0,ENB0.5}/\epsilon_{0,i})^2$ where $\epsilon_{0,Ei}$ is the absolute amplitude of the beam in experiment Ei (from Fig. 3.7b).

The meridional structure of the TEJs within the beam is not highly sensitive to the beam amplitude but there are some differences (Fig. 3.22a). The significant change is in the latitudinal positions of the eastward TEJs near 2° off the equator: those TEJs are at the same latitude in ENB0.05 and ENB0.125, displaced by 1/4° closer to the equator in ENB0.25 and displaced poleward by 1/4–1/2° in ENB0.5

and ENB1. Notice also that the off-equatorial westward TEJs appear only in the experiments with moderate and strong forcing (ENB0.5 and ENB1). The tendency in the *normalized* amplitude of the TEJs observed in Fig. 3.22a is in accord with Fig. 3.19: the amplitude in the experiments with stronger forcing is weaker than expected from a quadratic relation.

The meridional structure of the TEJs to the west of the beam differs much more among the experiments (Fig. 3.22b). In ENB0.25 and ENB0.5, the structure is similar to that within the beam although the eastward off-equatorial TEJs are located more poleward by 1/4–1/2°and the westward off-equatorial TEJs are relatively stronger. As argued earlier, the mean flows obtained in the experiments with weak forcing (ENB0.05 and ENB0.125) are the result of rectifications involving other high-frequency motions and do not correspond to TEJs. The interesting change occurs in the experiment with strong forcing (ENB1) where a minimum in the westward velocity is found at the equator and the off-equatorial TEJs are displaced poleward by 1/2° .

3.4.3 Sensitivity to model resolution

The TEJs are still present when the vertical resolution is either decreased by half (ENB0.5_LV) or doubled (ENB_HV), when the horizontal resolution is doubled (ENB0.5_HH), or when both the vertical and horizontal resolution are increased (ENB0.5_VHVH). Significant differences arise between the experiments, however, in terms of amplitude and vertical and meridional structure.

One way to rationalize how the amplitude varies with respect to the horizontal resolution Δx and the vertical one Δz is to plot the amplitude of the TEJs against $\Delta x/\Delta z$. This is done in Fig. 3.23a for the equatorial westward TEJ and northern eastward TEJ both within and to the west of the basin. ENB0.5_HV and

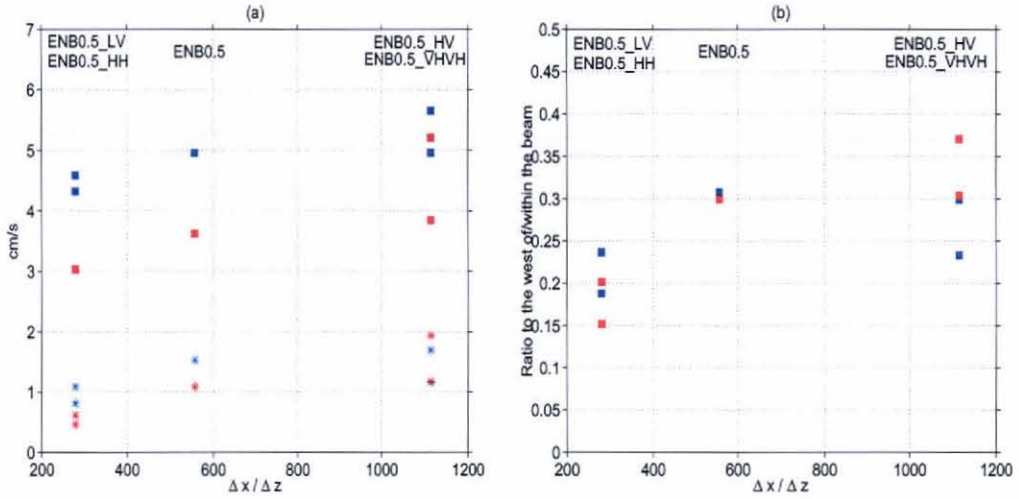

Figure 3.23: (a) Amplitude of the TEJs within (square) and to the west of (star) the beam for ENB0.5, ENB0.5_LV, ENB0.5_HV, ENB0.5_HH and ENB0.5_VHVH. The amplitude is defined as in Fig. 3.19. (b) Ratio of the amplitude of the TEJs to the west of/within the beam. In both panels, red corresponds to the eastward TEJ north of 1°N and blue to the westward equatorial TEJ within 1° from the equator and the horizontal axes represents the ratio $\Delta x/\Delta z$, where Δx is the horizontal resolution and Δz is the vertical one. The eastward off-equatorial TEJ and westward equatorial TEJ to the west of the beam in ENB0.5_VHV have the same amplitude: the red star of the former thus masks the blue star of the latter in the lower right corner in (a).

ENB0.5_VHVH have the highest $\Delta x/\Delta z$ ratio, while ENB0.5_LV and ENB0.5_HH have the lowest ratio. Except for the case of the equatorial westward TEJ to the west of the beam in ENB0.5_VHVH, the tendency is toward an increase in the amplitude of the TEJs as $\Delta x/\Delta z$ increases. In other words, TEJs are stronger both within and to the west of the beam when the vertical resolution is favored compared to the horizontal one. However, although ENB0.5_HV and ENB0.5_VHVH have the same $\Delta x/\Delta z$ ratio, the TEJs in ENB0.5_VHVH are systematically weaker

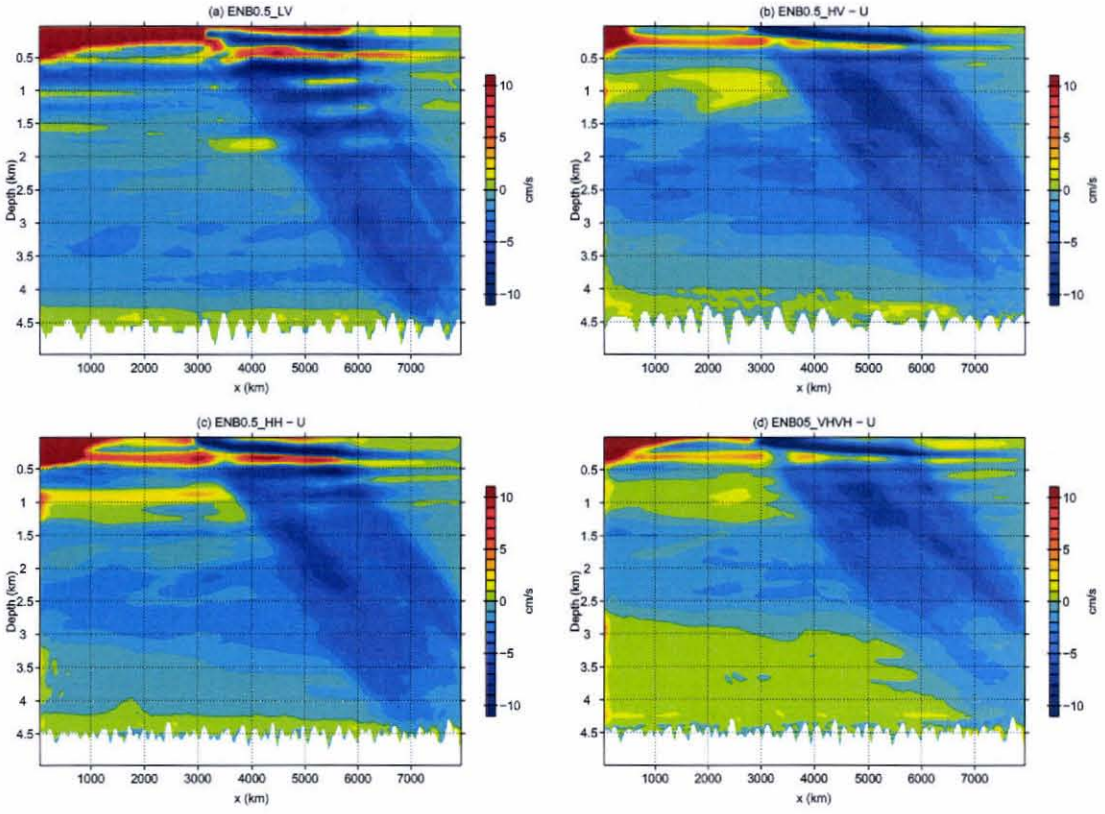

Figure 3.24: As in Fig. 3.14 but for (a) ENB0.5_LV, (b) ENB0.5_HV, (c) ENB0.5_HH and (d) ENB0.5_VHVH.

than in ENB0.5_HH, suggesting that the strength of the TEJs does not depend only on $\Delta x/\Delta z$. Similarly, the amplitude of the TEJs to the west of the beam relative to those within the beam is either stationary or increases with $\Delta x/\Delta z$ (Fig. 3.23b), with the exception, again, of the equatorial TEJ in ENB0.5_VHVH, the relative amplitude of which is weaker than in experiments with smaller $\Delta x/\Delta z$.

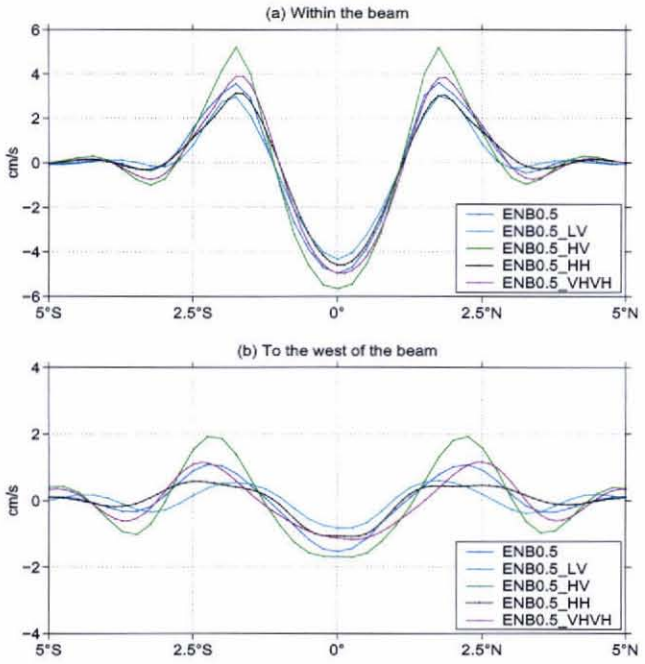

Figure 3.25: As in Fig. 3.22 but for ENB0.5, ENB0.5_

highest vertical resolution (Fig. 3.24d). Another difference is the EDJ-like structure embedded within the beam in ENB0.5_LV (3.24a), but the low vertical resolution used in this experiment suggests that this structure may be a numerical artifact.

The meridional structure of the TEJs within the beam does not vary much (Fig. 3.25a): the shapes and locations of the TEJs are about the same from one experiment to another. Larger variations occur in the structure of the TEJs to the west of the beam (Fig. 3.25b). The higher the vertical resolution, the more poleward the eastward TEJs. The eastward TEJs in ENB_HH are also flattened compared to the other experiments.

3.5 Mean potential vorticity balance

In this section, the mean PV balance is analyzed in the standard experiment ENB0.5. It confirms the conclusion found from the analysis in Section 2.1 for the JAMSTEC model that the Yanai wave dominates the mean eddy PV balance but it also illustrates the sensitivity of such analysis to noise, either real or computational, and the difficulty in quantifying the effect of eddies on the mean flow using this diagnostic.

The velocity field is computed along the isopycnals spanning the 1000–2250 m depth range. For every quantity a, one considers only two components, its 3-year time-mean $\overline{a}$ over years 7–9 and its Yanai-wave (or "eddy") component a' defined as the band-pass filtered version of a between the 32-day and 34-day periods. The results are not sensitive to the choice of the filter.

The mean eddy PV fluxes have patterns similar to those observed in the JAMSTEC model (Figs. 2.1 and 3.26). They are spatially limited to the Yanai beam with the zonal flux G_x and the meridional flux G_y being antisymmetric and symmetric, respectively, about the equator. The G_x field is more zonally coherent within the

MISSING
PAGE
NO.

75, 76, 77

AT THE TIME OF
MICROFILMING

Scanning

It is noteworthy that the analysis of the mean PV balance reproduces a mean flow, that is barely consistent with the model output, even in the present idealized situation where the main variability is due to the Yanai beam only. The comparison is worse to the west of the beam where the eddy-induced zonal velocity is an order of magnitude stronger than the output velocity (Fig. 3.28b). It is not clear if such differences are due to an error in our calculation or an integrated effect of the noise arising from the calculation. The latter possibility is supported by the fact that the eddy-induced mean zonal flow is deduced from the eddy-induced mean meridional velocity, which is less than 1 cm s^{-1} in ENB0.5. Indeed, small errors in the calculation of the mean meridional velocity can be amplified by taking its divergence and applying the zonal integration needed in Eq. (2.5). Although we have taken care in calculating those terms, it is not clear what further conditions are needed to obtain a satisfactory result. Some possible improvements may be obtained by using a smaller time step for the ouput and/or a better vertical and horizontal resolution. Unfortunately, we did not keep 5-day averages in, for instance, ENB0.5_HH to perform such sensitivity analysis of the mean PV balance. The case shown here, however, illustrates already the difficulty in diagnosing the effect of eddies in a more realistic context.

3.6 Conclusions

The conclusions from the numerical study are:

- *the numerical experiments support the idea that a beam of monthly-periodic Yanai waves can rectify itself into a set of currents resembling the observed TEJs in terms of zonal, meridional and vertical structures;*
- *TEJs are found within the beam for all beam amplitudes: however, they are found everywhere to the west of the beam only when the beam amplitude is*

strong enough, that is for a Froude number reaching about 1/4;

- *the amplitude of the TEJs within the beam is as large as the observed amplitude and that of the TEJs to the west of the beam is weaker by a factor of 2; in both regions, the amplitude varies roughly quadratically with the beam amplitude, suggesting that the TEJs are a result of a second-order nonlinear rectification;*

- *the presence of TEJs to the west of the beam is also correlated with an effective dissipation of the Yanai beam in the vertical, believed to be the by-product of multiple nonlinear interactions cascading the beam energy mainly toward small vertical scales;*

- *TEJs are still present when model resolution is increased and/or decreased by at least two-fold, but their amplitude tends to increase when a higher vertical rather than horizontal resolution is used;*

- *even in this idealized case, the mean flows deduced from the divergence of the eddy PV fluxes are barely consistent with the flows obtained from the model ouput, illustrating the difficulty in diagnosing the effect of eddies on the mean flows in observations and OGCMs;*

- *finally, a structure resembling the EDJs is also found in the upper 1000 m but its dynamical cause and its relation, if any, to the observed EDJs are not clear.*

In the next chapter, the problems of a Yanai plane wave and of a Yanai beam dissipated by either Rayleigh friction or Newtonian damping are studied analytically. The second-order nonlinear rectification of a Yanai beam can explain the formation of mean flows resembling the TEJs in the numerical simulations.

Chapter 4

Analytical solutions

4.1 Summary

We propose in this chapter to exploit a classic mechanism of wave-mean flow interaction to explain the formation of the TEJs in the previous numerical experiments. According to this mechanism, the TEJs are the $O(\epsilon_0^2)$ rectification of a monthly-periodic Yanai beam dissipated in the vertical, with ϵ_0 being the dimensionless amplitude of the beam at the surface. Without dissipation, the mean flow is constrained to the beam; it cancels exactly the Stokes drift due to the Yanai beam, yielding a zero mean Lagrangian flow and stationnary water parcels over a wave cycle. With dissipation, the decay of the Yanai beam in the vertical provides a source of PV resulting in a Lagrangian component of the mean flow found to the west of the beam. This component forms a basin-wide gyre with meridional flow and water parcels moving meridionally within the beam.

4.2 Previous work

The following analytical solution is based on processes that have already been well described by the theory of wave-mean flow interaction (*e.g.* McPhaden *et al.* 1986, McPhaden and Ripa 1990). One important piece of this theory is the so-called non-interaction or non-acceleration theorem (*e.g.*, Andrews and McIntyre 1976; Boyd 1976; Dunkerton 1980), developed in meteorology for the case of zonally-averaged and *periodic* flows; it stipulates that *a conservative wave field cannot accelerate or decelerate an Eulerian mean flow.* How does this theorem translate into the oceanographic context of a basin with meridional boundaries? A partial answer is given by Moore (1970) who found the general theorem valid both in either configuration that *a conservative wave field cannot generate a mean Lagrangian flow if there are no closed geostrophic contours.*

In the case of the zonally-periodic flat-bottom ocean, any (Eulerian) geostrophic mean zonal flow can be added to the solution. The non-acceleration theorem tells us that the conservative wave field does not exchange energy with this flow. Because the geostrophic contours are closed, a Lagrangian mean flow is allowed according to Moore's theorem. This Lagrangian flow is the sum of the Stokes drift associated with the wave field plus the undetermined mean Eulerian flow.

In the case of the flat-bottom ocean limited by meridional boundaries, there are no closed geostrophic contours and Moore's theorem adds the new constraint that the mean Lagrangian flow has to be zero. Thus, if the Stokes drift associated with the conservative wave field is non-zero in the interior, it has to be cancelled everywhere by a mean Eulerian flow; at the boundaries, the Lagrangian, the Eulerian and the Stokes drift all go individually to zero. Although, as in the channel case, the wave field is not accelerating or decelerating that mean Eulerian flow, it is still the presence of the wave field together with the boundary conditions that are the cause of the

mean Eulerian flow in the interior. Thus, although the wave field does not exchange energy with the Eulerian mean flow in the steady state, one might argue that it does "interact" with it *via* the boundary conditions. The difference with the channel case is subtle but important in the oceanographic context.

The non-acceleration theorem further details the three main mechanisms for a wave field to be non-conservative and to start to accelerate/decelerate an Eulerian mean flow: 1) dissipation, 2) absorbtion at critical layers or 3) non-stationarity. Those mechanims are valid independent on the geometry of the problem. We are dealing in this study entirely with the case of wave dissipation. The dissipation of oceanic equatorial waves by Rayleigh friction and Newtonian damping has already been studied, in particular by Yamagata and Philander (1985) in the case of one baroclinic mode and by Gent (1987) in the case of a vertically propagating wave, but in neither case was the $O(\epsilon_0^2)$ rectification computed. Extensive work has been performed in the oceanographic context to study the effect of $O(1)$ and x-independent background zonal flow with vertical and meridional shears on damped equatorial waves and the resulting wave-induced $O(\epsilon_0^2)$-acceleration of the mean flow. For instance, McPhaden *et al.* (1986) and Proehl (1990) studied Kelvin and long Rossby waves respectively, considering a single baroclinic mode. In a fashion similar to the present solution, Rothstein *et al.* (1988) studied the case of a Kelvin *beam* propagating into the deep ocean. All these studies, however, focused on the upper ocean, and none of them considered the $O(\epsilon_0^2)$-effect of the damped wave or beam in the simpler case of *no background flow*. The latter situation is what we study here for the case of a Yanai wave and a Yanai beam.

4.3 $O(\epsilon_0)$-solution: dissipated wave and beam

Two cases are considered: a single plane wave and a beam. In both cases, the ocean is considered infinite in the y and z directions. It is also infinite in x in the wave case, but is semi-infinite for the beam with an eastern boundary at x_{EB}. It has a constant stratification given by its Brunt-Väisälä frequency N. The *in-situ* density is decomposed into a mean value, a mean vertical profile and an anomaly, $\rho_{tot}(x,y,z,t) = \rho_0\,[1+\overline{\rho}(z)+\rho(x,y,z,t)]$, and the pressure field in a similar way. The equator is located at $y = 0$ and in the following only solutions that decrease toward the poles are considered. The linearized set of equations at $O(\epsilon_0)$ (*e.g.*, McCreary 1985) is

$$\partial_t u - fv + \partial_x p = -ru, \tag{4.1}$$

$$\partial_t v + fv + \partial_y p = -rv, \tag{4.2}$$

$$-1/N^2\partial_{zzt}p + \partial_x u + \partial_y v = \lambda/N^2\partial_{zz}p, \tag{4.3}$$

where u and v are the zonal and meridional velocities respectively and p is the pressure anomaly divided by ρ_0. The first two equations are the zonal and meridional momentum equations. In these, the term on the right-hand side (rhs) corresponds to linear Rayleigh friction with damping time scale $1/r$. The third equation is the continuity equation where the vertical velocity w has been written as a function of pressure using the linearized density equation

$$\partial_t \rho - \frac{N^2}{g} w = -\lambda\rho, \tag{4.4}$$

where g is gravity and λ is inverse of the Newtonian damping time scale. The hydrostatic approximation

$$\partial_z p = -\rho g \tag{4.5}$$

has also been used.

Solutions of Eqs. (4.1)-(4.3) have the general form

$$(u,v,p) \propto \mathcal{C}\epsilon_0 \Re\left[(\widetilde{u},\widetilde{v},\widetilde{p})(y)e^{i(kx+mz-\omega t+\varphi)}\right] \text{ with } (k,\omega,\varphi) \in \mathbb{R}, m \in \mathbb{C}, \qquad (4.6)$$

describing equatorially-trapped waves propagating zonally and vertically. The wave frequency, wavenumbers and phase can be grouped into the vector $\vec{\varphi} = (\omega, k, m, \varphi)$ where ω is the frequency, k and m are the zonal and vertical wavenumbers, and φ is the phase. For a vertically propagating wave, k and ω are kept real while $m = m^r + im^i$ is considered complex, that is, the wave is damped with a rate m^i while propagating vertically with a vertical wavelength $|2\pi/m^r|$. In Eq. (4.6), $\mathcal{C} = |N/m^r|$ is the velocity scale and corresponds to the gravity-wave speed in the inviscid case, and ϵ_0 the dimensionless wave amplitude at $z = 0$. Variables $\widetilde{u}$, $\widetilde{v}$ and $\widetilde{p}$ are the dimensionless meridional profiles of u, v and p and depend only on y. Defining the complex number $c = \pm N/m$, the system of Eqs. (4.1)-(4.3) becomes

$$\partial_t u - fv + \partial_x p = -ru, \qquad (4.7)$$

$$\partial_t v + fv + \partial_y p = -rv, \qquad (4.8)$$

$$\frac{1}{c^2}\partial_t p + \partial_x u + \partial_y v = -\frac{\lambda}{c^2}p. \qquad (4.9)$$

Thanks to the simplification of constant stratification, this new system is z-independent and is equivalent to the system already solved by Yamagata and Philander (1985). Eliminating u and p in Eqs. (4.7)-(4.9) and substituting Eq. (4.6), one obtains the v-equation

$$\frac{d^2\widetilde{v}}{dy^2} + \left[\frac{(\omega+i\lambda)(\omega+ir)}{c^2} - k^2 - \frac{\beta k}{\omega+ir} - \frac{\omega+i\lambda}{\omega+ir}\frac{f^2}{c^2}\right]\widetilde{v} = 0. \qquad (4.10)$$

The meridional profile in v for a Yanai wave is a Gaussian centered on the equator,

$$\widetilde{v}(y) = e^{-\frac{\beta}{2c}\left[\frac{y}{A}\right]^2}, \qquad (4.11)$$

where

$$A = \left[\frac{\omega+ir}{\omega+i\lambda}\right]^{1/4}. \qquad (4.12)$$

The constraint that the solutions need to be equatorially trapped imposes the sign of c in order that

$$L_{eq}^2 \equiv \Re\left[\frac{2cA^2}{\beta}\right] \geq 0. \tag{4.13}$$

L_{eq} can then be considered as an equatorial Rossby radius. In Appendix B.1, it is shown that for the regime explored here where $(r, \lambda) \ll \omega$, the meridional profile in Eq. (4.11) is not too different from the inviscid case and L_{eq} nearly equals its inviscid value $\sqrt{2C/\beta}$.

The dispersion relation obtained by plugging Eq. (4.11) into Eq. (4.10) is

$$k = -\frac{1}{2}\frac{\beta}{\omega + ir} \pm \frac{1}{2}\left[\frac{\beta}{\omega + ir} - 2\frac{(\omega + i\lambda)^{1/2}(\omega + ir)^{1/2}}{c}\right]. \tag{4.14}$$

The solution with + corresponds to the Kelvin wave and that with − to the Yanai wave. Thus, the dispersion relation for the Yanai wave is

$$k = -\frac{\beta}{\omega + ir} + \frac{(\omega + i\lambda)^{1/2}(\omega + ir)^{1/2}}{c}. \tag{4.15}$$

With $m = \pm N/c$, Eq. (4.15) provides the relation for m

$$m = \pm N\frac{k + \frac{\beta}{\omega + ir}}{(\omega + i\lambda)^{1/2}(\omega + ir)^{1/2}}. \tag{4.16}$$

Given k and ω, there are two solutions for a Yanai wave, one with upward propagating phase ($m^r \geq 0$) which is the + solution in Eq. (4.16), the other downward. In the following, only the upward-phase-propagating solutions (downward energy propagation) are considered.

The solution for a single, equatorial, plane wave is then,

$$v = C\epsilon(z)\,\Re\left[\widehat{v}_{\vec{\varphi}}\right], \tag{4.17}$$

$$u = C\epsilon(z)\,\Re\left[(i/c)\,(\omega + i\lambda)^{1/2}(\omega + ir)^{1/2}\,(y\,\widehat{v}_{\vec{\varphi}})\right], \tag{4.18}$$

$$p = C\epsilon(z)\,\Re\left[i\,(\omega + ir)\,(y\,\widehat{v}_{\vec{\varphi}})\right], \tag{4.19}$$

$$\rho = C\epsilon(z)\,\Re\left[(m/g)\,(\omega + ir)\,(y\,\widehat{v}_{\vec{\varphi}})\right], \tag{4.20}$$

$$w = C\epsilon(z)\,\Re\left[-i\,(m/N^2)\,(\omega + i\lambda)(\omega + ir)\,(y\,\widehat{v}_{\vec{\varphi}})\right], \tag{4.21}$$

where $\widehat{v}_{\vec{\varphi}} = e^{-\frac{\beta}{2c}\left[\frac{y}{A}\right]^2} e^{i(kx+m^r z-\omega t+\varphi)}$, and $\epsilon(z) = \epsilon_0 e^{-m^i z}$ is the vertical profile of the dimensionless wave amplitude.

To form a beam, a set of single plane wave solutions with wave frequency, wavenumbers and phase $\vec{\varphi_n} = (\omega, k_n, m_n, \varphi_n)$, dimensionless amplitude $\epsilon_n(z) = \epsilon_{0,n} e^{-m_n^i z}$ and velocity scale $\mathcal{C}_n = |N/m_n^r|$ is summed, with n being the index of each wave and ω being fixed for each wave. For each k_n, the vertical wavenumber m_n is computed using Eq. (4.16); again, only upward-phase-propagating beams are considered. The beam solution for v is then

$$v = \sum_n v_n = \sum_n \mathcal{C}_n \epsilon_n(z) \, \Re\left[\widehat{v}_{\vec{\varphi_n}}\right], \tag{4.22}$$

and similarly $u = \sum_n u_n$, etc.

In the case studied here, the beam solution Eq. (4.22) can be represented within the beam by the solution of a dominant single wave with $\vec{\varphi} = (\omega, k, m, \varphi)$ and velocity scale $\mathcal{C}$, and one can then define a dimensionless amplitude for the beam, $\epsilon(z)$, such as

$$v \approx \mathcal{C}\epsilon(z) \, \Re\left[\widehat{v}_{\vec{\varphi}}\right]. \tag{4.23}$$

In this case as in the case of the single wave, $\epsilon(z) = \mathcal{V}(z)/\mathcal{C}$ where $\mathcal{V}(z)$ is the amplitude of the meridional flow at z. It is the measure of the amount of nonlinearity introduced in Section 3.3 and corresponds in the inviscid case to the meridional Froude number introduced by Hua08.

In Sections 4.6 and 4.7, analytical solutions for the case of a beam are constructed to replicate the numerical solutions. The value of ϵ_0 and m^i used in $\epsilon(z)$ of Eq. (4.23) are obtained by fitting $\epsilon(z)$ to the vertical amplitude profile of each numerical solution and plotted in Fig. 3.7b. The relative magnitude of each wave, $[\mathcal{C}_n\epsilon_n(z]/[\mathcal{C}\epsilon(z)]$ as well as the wave properties (k_n, φ_n) are obtained from the Fourier decomposition in

x of the normalized zonal profile of the meridional surface stress used to generate the Yanai beam in the numerical solutions (Section 3.2).

4.4 $O(\epsilon_0^2)$-solution: Eulerian mean

The nonlinear advective terms neglected in Eqs. (4.1), (4.2) and (4.4) appear at $O(\epsilon_0^2)$. Composed of products of $O(\epsilon_0)$-terms, they can be considered as forcing terms of the $O(\epsilon_0^2)$-problem. If a single plane wave is considered, these forcing terms have only two components: one with zero frequency (time-mean) and zonal wavenumber (x-independent), the other with twice the frequency and zonal wavenumber. In the case of a beam, more components appear, always made of the sum or difference of frequencies and zonal wavenumbers, and in particular there is always a time-mean component. Here, only the time-mean component is considered. The $O(\epsilon_0^2)$-system providing the time-mean solution is then

$$-fV_E + \partial_x P = F_x, \tag{4.24}$$

$$+fU_E + \partial_y P = F_y, \tag{4.25}$$

$$\partial_x U_E + \partial_y V_E = g/N^2 \partial_z F_\rho, \tag{4.26}$$

where U_E and V_E are the Eulerian time-mean $O(\epsilon_0^2)$ zonal and meridional velocities, and P the time-mean $O(\epsilon_0^2)$ pressure normalized by ρ_0. The terms on the rhs are derived from the advective terms neglected in Eqs. (4.1), (4.2) and (4.4), that is,

$$\begin{bmatrix} F_x \\ F_y \\ F_\rho \end{bmatrix} = -\overline{(\vec{u} \cdot \vec{\nabla}) \begin{bmatrix} u \\ v \\ \rho \end{bmatrix}}, \tag{4.27}$$

where the overbar is a time average over a wave period. In Eq. (4.27), F_x and F_y are minus the advection of zonal and meridional momentum, F_ρ is minus the advection

of density, u, v and ρ are from the $O(\epsilon_0)$-solution and $\vec{u}.\vec{\nabla} = u\partial_x + v\partial_y + w\partial_z$. Dissipation is an essential ingredient at $O(\epsilon_0)$ to obtain detuning between the phase of the wave components, but it plays only a secondary and standard role for the time-mean solution at $O(\epsilon_0^2)$. It also makes the resolution of the $O(\epsilon_0^2)$-problem needlessly more complicated. In consequence, the viscous terms have been neglected for simplicity in Eqs. (4.24)-(4.26).

The system of Eqs. (4.24)-(4.26) is solved straightforwardly. The solution for the velocity is

$$W_E - W_a = 0 - \frac{g}{N^2}F_\rho, \tag{4.28}$$

$$V_E = \frac{1}{\beta}\vec{\nabla}_H \times (F_x, F_y) - \frac{g}{N^2} y\, \partial_z F_\rho, \tag{4.29}$$

$$U_E - U_{EB} = \int_x^{x_{EB}} \frac{1}{\beta}\partial_y \left\{\vec{\nabla}_H \times (F_x, F_y)\right\} - \frac{g}{N^2}\left\{2\partial_z + y\,\partial_{yz}\right\} F_\rho dx, \tag{4.30}$$

where W_E is the Eulerian time-mean $O(\epsilon_0^2)$ vertical velocity and $\vec{\nabla}_H = (\partial_x, \partial_y)$. The first terms on the rhs correspond to the solution due only to advection of momentum. This solution is mathematically similar to the Sverdrup circulation with V_E being proportional to the curl of the forcing and U_E to the zonal integral of the meridional derivative of that curl. In this case, the flow is strictly horizontal ($W_E = 0$). The second terms on the rhs correspond to the solution due only to the advection of density. The corresponding three-dimensional flow is buoyancy-driven and is equivalent to a beta-plume circulation (*e.g.* Pedlosky 1996).

Because only the z-derivative of W_E enters the system of Eqs. (4.24)-(4.26), W_E is known only within an arbitrary z-independent vertical circulation $W_a = W_a(x, y)$. In the next section, it is shown that in the main case studied here of no Newtonian damping, $W_a = W_L$ where W_L is the mean vertical Lagrangian flow. By imposing $W_L = W_a = 0$, we assure that there is no mean vertical transport of mass, the water parcels staying stationary in the vertical over a wave cycle, and the stratification is

kept constant.

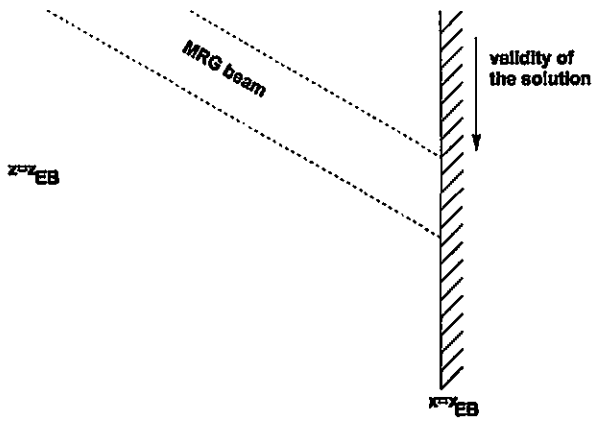

Figure 4.1: Locations in x and z of the validity of the analytical solution in the case of a downward-energy-propagating Yanai beam.

Similarly, because of the zonal integral in Eq. (4.30), U_E is known only within an x-independent zonal flow $U_{EB} = U_E(y, z; x_{EB})$, given by the solution U_E at $x = x_{EB}$. U_{EB} is an arbitrary zonal geostrophic flow which can be added to any solution of Eqs. (4.24)-(4.26). In the case of a single plane wave, the ocean has to be infinite in x, otherwise the reflection of the wave at an eastern boundary has to be considered: there is no constraint on U_{EB} and no unique solution. In this situation, only the solution with $U_{EB}(y, z) = 0$ is considered. In the case of the beam, an eastern boundary can be added which then assures that the solution is unique with $U_{EB}(y, z) = 0$. The solution is, however, valid only for the portion of the water column where the beam has not yet reached the boundary. For a downward-propagating-energy beam, the solution is valid for $z > z_{EB}$, z_{EB} being the depth where the beam starts to reflect (Fig. 4.1). For $z \leq z_{EB}$, the reflection of the Yanai beam at the eastern boundary would have to be taken into account; at the monthly period, the Yanai beam reflects into β-plane Kelvin waves (Moore 1968; McCreary 1984), the energy of which propagates downward and away from the equator. Furthermore, any interactions

between the beam and the Kelvin waves can result in motions affecting only the portion $z \leq z_{EB}$, assuring the complete validity of the solution for $z > z_{EB}$.

4.5 $O(\epsilon_0^2)$-solution: Lagrangian mean

The solution $\overrightarrow{U_E} = (U_E, V_E, W_E)$ presented above corresponds to the Eulerian mean flow, that is the flow time-averaged at a fixed location. Tracers, however, follow the Lagrangian mean flow $\overrightarrow{U_L}$, which is the flow time-averaged *following a tracer*. In the absence of waves, $\overrightarrow{U_L} = \overrightarrow{U_E}$. Otherwise, the two quantities differ at $O(\epsilon_0^2)$ by what is called the wave-induced Stokes drift $\overrightarrow{U_S}$ (Longuet-Higgins 1969; Moore 1970),

$$\overrightarrow{U_S} = \overrightarrow{U_L} - \overrightarrow{U_E}, \tag{4.31}$$

where

$$\overrightarrow{U_S} = \overline{\left[\int_0^t \overrightarrow{u}(\overrightarrow{x}, t')dt' \cdot \overrightarrow{\nabla}\right] \overrightarrow{u}}, \tag{4.32}$$

$\overrightarrow{u} = (u, v, w)$ is the $O(\epsilon_0)$-flow associated with the wave, and $\overrightarrow{x} = (x, y, z)$ is the vector position. The $\overrightarrow{U_E}$, $\overrightarrow{U_L}$ and $\overrightarrow{U_S}$ velocities are thus all accurate to $O(\epsilon_0^2)$. Once $\overrightarrow{U_S}$ and $\overrightarrow{U_E}$ are computed, $\overrightarrow{U_L}$ is known.

The vertical Stokes drift W_S can be related to F_ρ in the case of no Newtonian damping ($\lambda = 0$). Because in both the plane wave and beam cases, every quantity q is periodic with the same frequency ω and period T, the following properties result:

$$q(\overrightarrow{x}, t + \frac{T}{4}) = q(\overrightarrow{x}, \frac{T}{4}) - \omega \int_0^t q(\overrightarrow{x}, t')dt', \tag{4.33}$$

$$q(\overrightarrow{x}, t + \frac{T}{4}) = \frac{1}{\omega}\, \partial_t q(\overrightarrow{x}, t). \tag{4.34}$$

Thus

$$F_\rho = -\overline{\left[\vec{u}(\vec{x},t)\cdot\vec{\nabla}\right]\rho(\vec{x},t)}, \tag{4.35}$$

$$= -\overline{\left[\vec{u}(\vec{x},t+\frac{T}{4})\cdot\vec{\nabla}\right]\rho(\vec{x},t+\frac{T}{4})}, \tag{4.36}$$

$$= -\overline{\left[\vec{u}(\vec{x},\frac{T}{4})-\omega\int_0^t\vec{u}(\vec{x},t')dt'\right]\frac{1}{\omega}\,\partial_t\rho(\vec{x},t)}, \tag{4.37}$$

which becomes using Eq. (4.4) with $\lambda = 0$,

$$F_\rho = -\frac{N^2}{g}\overline{\left[\vec{u}(\vec{x},\frac{T}{4})-\omega\int_0^t\vec{u}(\vec{x},t')dt'\right]\frac{1}{\omega}\,w(\vec{x},t)}, \tag{4.38}$$

$$= +\frac{N^2}{g}\overline{\left[\int_0^t\vec{u}(\vec{x},t')dt'\right]\,w(\vec{x},t)}, \tag{4.39}$$

$$= +\frac{N^2}{g}W_S. \tag{4.40}$$

It then follows from Eqs. (4.28) and (4.31) that $W_a = W_L$.

4.6 Applications

4.6.1 Inviscid single Yanai wave

To compute the forcing terms in Eq. (4.27) and the Stokes drift in Eq. (4.32), two properties are used: 1) for any periodic quantities a and b which are 90° out-of-phase, $\overline{ab} = 0$, and 2) any x, z or time derivative shifts the phase by 90° so that, for instance, $\overline{a\,\partial_x a} = 0$. A third property, that a y-derivative does not change the phase, holds only in the inviscid case ($r = 0$, $\lambda = 0$).

In the inviscid case of a single plane Yanai wave, u, p and w are 90° out-of-phase with v and ρ. Thus $F_x = -(\overline{u\,\partial_x u + v\,\partial_y u + w\,\partial_z u}) = 0$. Furthermore, F_ρ and F_y are uniform in x and z so that all terms on the rhs in Eqs. (4.29) and (4.30) are zero and $U_E = V_E = 0$. In consequence, the only non-zero Eulerian circulation is the mean

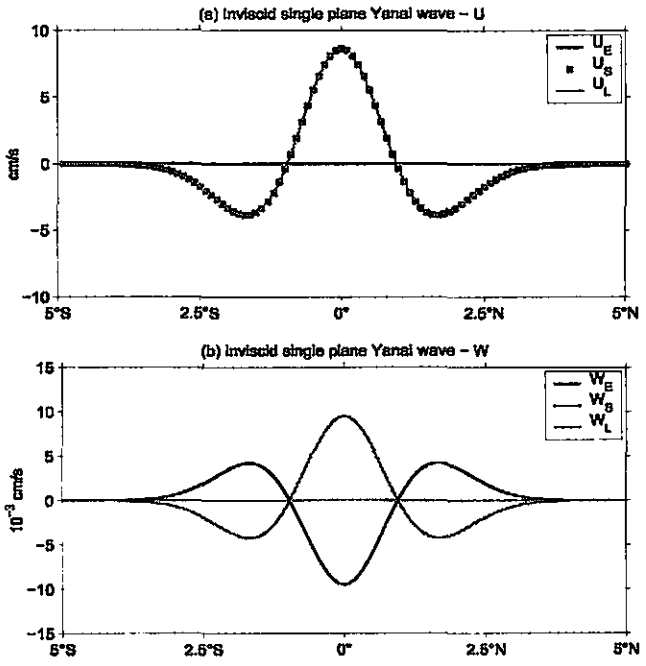

Figure 4.2: Eulerian-mean, Stokes-drift and Lagrangian-mean zonal and vertical components in the case of an inviscid single plane Yanai wave ($\epsilon_0 \approx 0.57$; $C \approx$ 53 cm s^{-1}; 1.1-month period and 9° zonal wavelength; $r = \lambda = 0$). There is no meridional flow in this case and the circulation is x and z-independent.

MISSING PAGE NO.

93

AT THE TIME OF MICROFILMING

SCANNING

vertical one triggered by F_ρ (Fig. 4.2b). It is x and z independent with a positive vertical Eulerian velocity at the equator and a negative one off the equator.

The Stokes drift has zonal and vertical components, mainly arising from the meridional gradient of u and w (Fig. 4.3): eastward and downward at the equator and the reverse off the equator. On the other hand, the mean Eulerian velocity is zero in the zonal direction and exactly cancels the Stokes drift in the vertical direction (Fig. 4.2) so that although parcels do move eastward at the equator and westward off the equator, they stay stationary on the vertical. The reason for the broken symmetry between the horizontal and vertical components comes from the different boundary conditions taken *via* W_a and U_{EB}: $W_a = 0$ imposes $W_L = 0$ while $U_{EB} = 0$ does not correspond to $U_L = 0$.

4.6.2 Viscid single Yanai wave

The addition of dissipation perturbs the phase relationships among the variables. For instance, if a and b were 90° out of phase and $\overline{ab} = 0$ in the inviscid case, the phase difference between a and b can deviate from 90° and $\overline{ab}$ no longer zero in the viscid case.

With Rayleigh dissipation, the mean circulation, both Eulerian and Lagrangian, is qualitatively changed. Both the wave and the resulting circulations decay exponentially with depth as $e^{-m^i z}$ and $e^{-2m^i z}$ respectively, but all components are still x-independent except for U_E and U_L. Meridional profiles are plotted in Fig. 4.4. U_S and all components of W (W_E, W_S and W_L) are qualitatively similar to the inviscid case. A first difference with the inviscid case is that V now has non-zero components. The mean Eulerian and Lagrangian flows are equatorward and the Stokes drift is poleward. A second difference is U_E being non-zero and larger in amplitude than U_S: the resulting zonal Lagrangian flow is reversed from the inviscid case. More

MISSING PAGE NO.

95, 96

AT THE TIME OF MICROFILMING

SCANNING

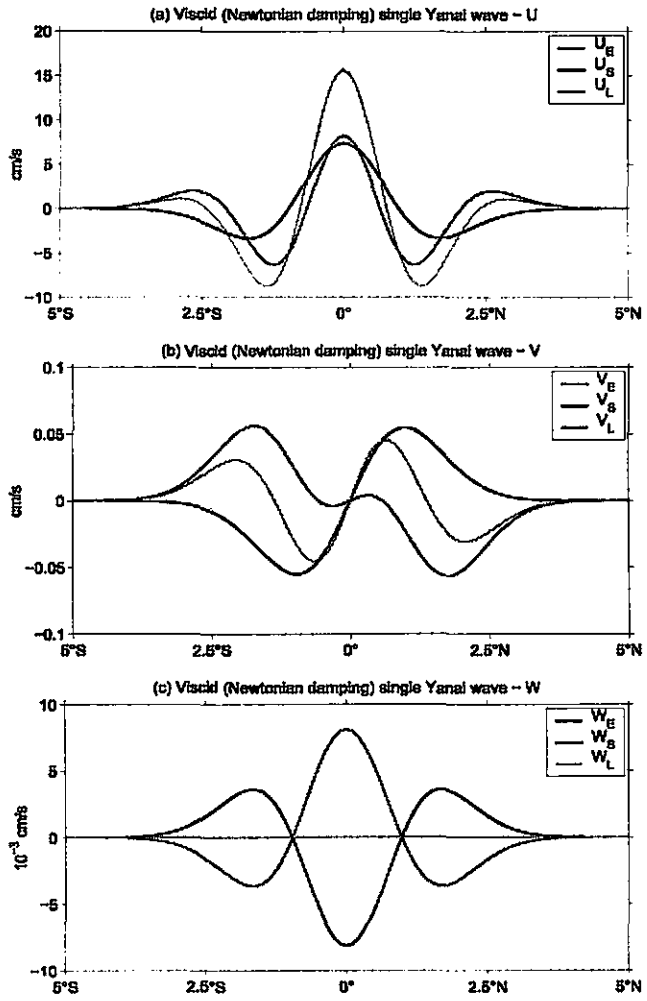

Figure 4.6: Eulerian-mean, Stokes-drift and Lagrangian-mean components in the case of a single plane Yanai wave dissipated by Newtonian damping ($\epsilon_0 \approx 0.57$; $C \approx 53$ cm s^{-1}; 1.1-month period and 9° zonal wavelength; $r = 0$, $\lambda \approx 0.027\omega$) and plotted at $z = -1500$ m. Except for U_E and U_L, all components are x-independent. U_E and U_L have been computed by integration from $x_E = 8000$ km westward, and their profiles plotted here are those at $x = 0$.

U_E cancels U_S near $x = 6500$ km, and farther west it dominates U_L with westward flow at the equator. Because all vertical profiles are decaying exponentially with z, the rate at which U_E increases to the west decreases downward (not shown) and the location where U_E cancels U_S is shifted westward with depth, but the overall pattern of Fig. 4.5 is maintained. U_L is zonally divergent where U_E cancels U_S.

In the case of Newtonian damping, the mean Eulerian and Lagrangian zonal flows are reversed and are inconsistent with the structure of the TEJs (Fig. 4.6). Changes also appear with the components of V which are much weaker and/or have a more complex meridional structure. Furthermore, for a diffusion time scale of Newtonian damping similar to the diffusion time scale used in the case of Rayleigh friction, all components decay much less rapidly with depth than in the case of Rayleigh friction (not shown), consistent with the approximate analytical solutions described in Appendix B.1. Solutions with Rayleigh friction *and* Newtonian damping of similar ($Pr = r/\lambda = 1$) or realistic ($Pr \sim 10$) strength trigger in both cases flows that are resembling the TEJs. This study of the dissipated single plane Yanai wave suggests that mean flows resembling the TEJs can be obtained analytically by using Rayleigh friction alone and mainly this case will be considered hereafter.

4.6.3 Inviscid Yanai beam: application to ENB0.05

In this section, the analytical solution called ANB0.05 for the case of an inviscid Yanai beam is considered and compared to the numerical solution of experiment ENB0.05 where it has been shown that virtually no dissipation of the beam occurs (see Section 3.3). It is shown here that the beam geometry allows mean Eulerian horizontal flows within the beam even without dissipation, unlike the case of the inviscid single plane wave.

The values of $\epsilon_0 \approx 0.064$, $C \approx 53$ cm s^{-1} and $r = \lambda = 0$ are used to replicate the

MISSING PAGE NO.

99, 100

AT THE TIME OF MICROFILMING

SCANNING

sign from one edge to the other. It acts as a source of divergence at the equator and convergence off the equator. Its vertical structure along the equator is given in Fig. 4.9. In Fig. 4.9, a structure with a small vertical scale appears in ENB0.05 but not in ANB0.05, and is associated with the unique EDJ-like structure described in the Appendix A.2, which is not considered in the analytical solution.

The mean Eulerian zonal and vertical flows are compared in Fig. 4.10 between the numerical and analytical solutions. Again, the analytical solution successfully reproduces the amplitude and spatial structure of the numerical solution; the comparison in terms of a vertical and zonal average across the beam is nearly perfect (Figs. 4.12a and c). In both cases, the flows are confined within the beam. As described in Section 3.4.2, U_E has a meridional structure resembling the TEJs with a westward equatorial flow and eastward off-equatorial ones. Not discussed previously is the existence of a mean vertical flow W_E, which appears as an equatorial "upwelling" and off-equatorial "downwelling". The mean meridional flow V_E is not part of the comparison because the analytical solution is several orders of magnitude weaker than the numerical one which is dominated by noise from the 3-year averaging of the Yanai variability.

The meridional and vertical structure of U_E and W_E within the beam are compared in Fig. 4.11. The analytical solution does not include the EDJ-like motion near the surface. It does, however, explain the amplitude and the large-vertical-scale structure of the TEJs of the numerical solution.

The analytical solution also provides the Stokes drift and Lagrangian mean components (Fig. 4.12). In both the zonal and vertical components, the mean Eulerian flow nearly cancels the Stokes drift so that the mean Lagrangian components are nearly zero, while all mean meridional components are nearly zero: averaging over a wave cycle the water parcels are thus nearly stationary in the horizontal and vertical.

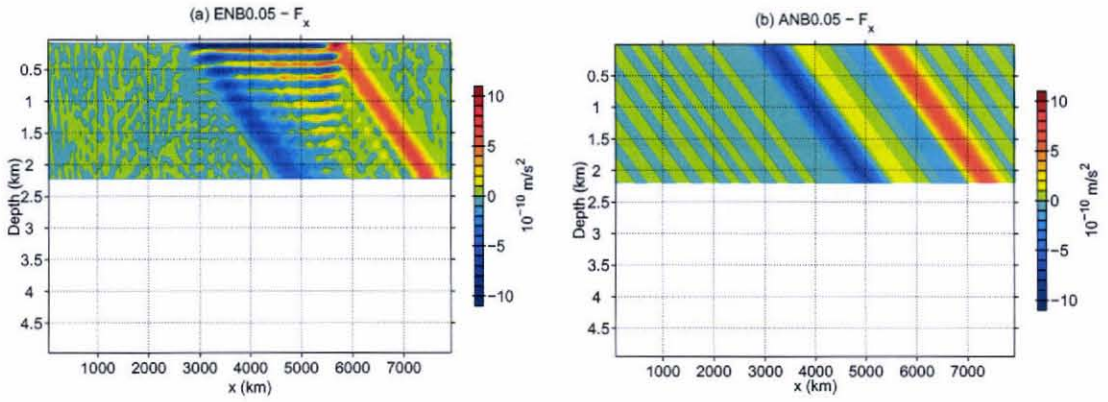

Figure 4.9: Zonal nonlinear term F_x from years 7–9 in ENB0.05 (left) and ANB0.05 (right).

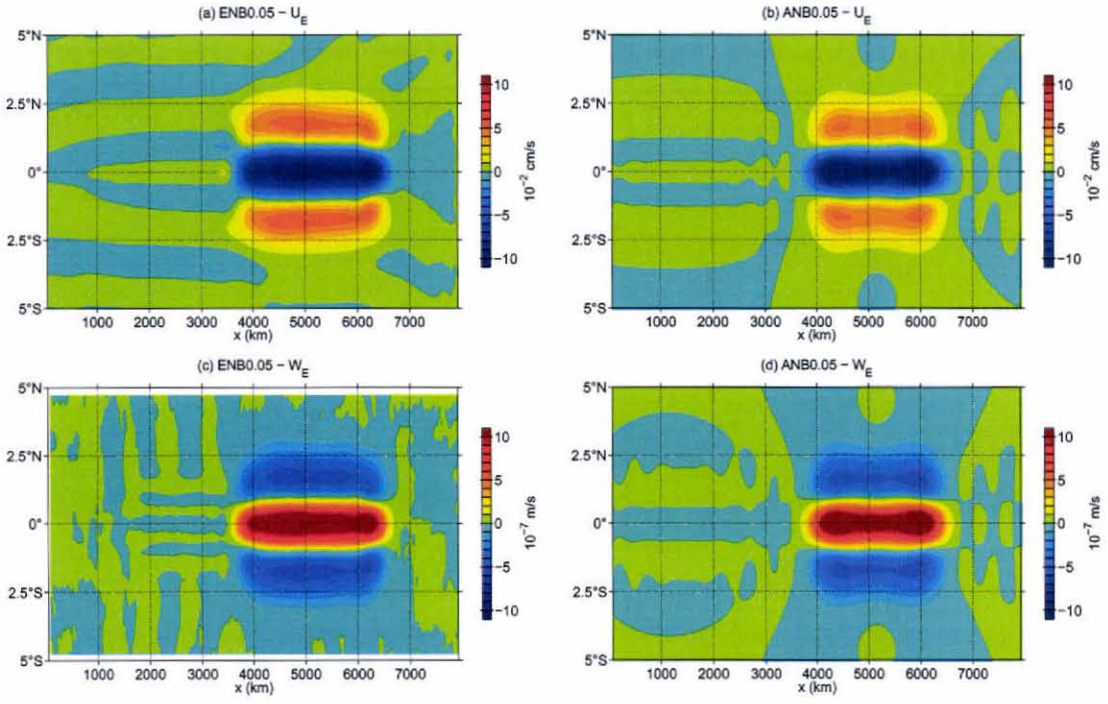

Figure 4.10: Mean Eulerian velocity field along-beam averaged between z_{max} and z_{min} and from years 7–9 in ENB0.05 (left) and ANB0.05 (right): U_E (upper) and W_E (lower).

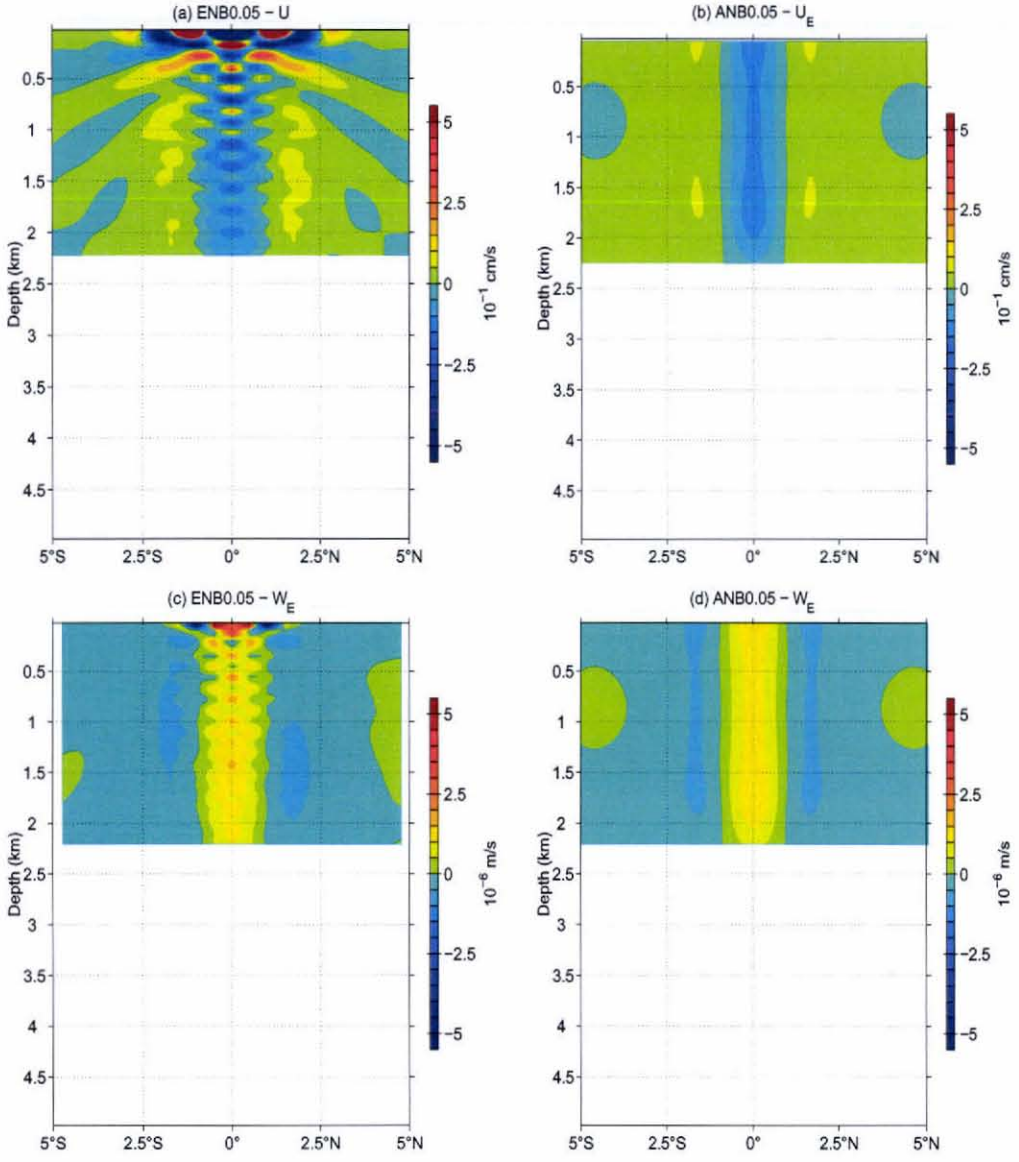

Figure 4.11: Mean Eulerian velocity field at $x = 5000$ km and from years 7–9 in ENB0.05 (left) and ANB0.05 (right): U_E (upper) and W_E (lower).

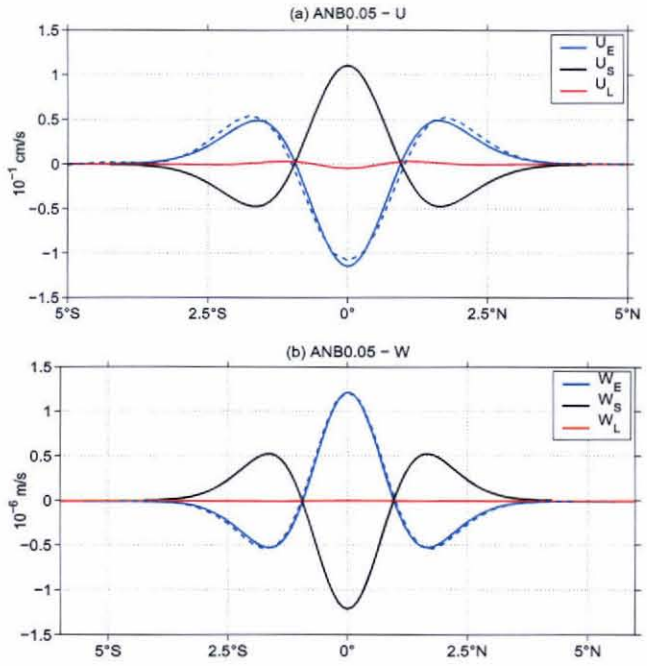

Figure 4.12: Eulerian-mean, Stokes-drift and Lagrangian-mean components in ANB0.05 along-beam averaged between z_{max} and z_{min} as well as between the two edges of the beam. The mean Eulerian zonal and vertical components from ENB0.05 are plotted with dashed blue lines.

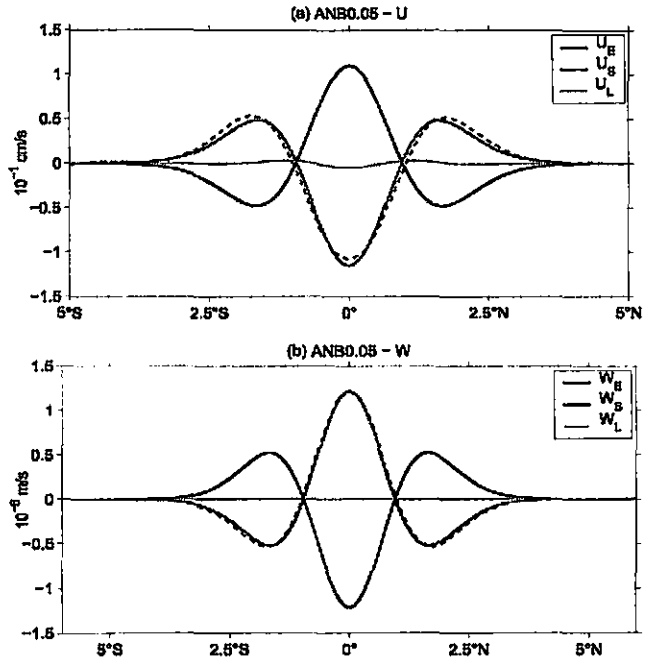

Figure 4.12: Eulerian-mean, Stokes-drift and Lagrangian-mean components in ANB0.05 along-beam averaged between z_{max} and z_{min} as well as between the two edges of the beam. The mean Eulerian zonal and vertical components from ENB0.05 are plotted with dashed blue lines.

MISSING PAGE NO.

105

AT THE TIME OF MICROFILMING

SCANNING

4.6.4 Viscid Yanai beam: application to ENB0.5

In this section, the analytical solution ANB0.5 in the case of a viscid Yanai beam is considered and compared to the numerical solution ENB0.5. Unlike the previous case, Rayleigh friction is used to cause the decrease of the beam amplitude with depth. The values $\epsilon_0 \approx 0.57$, $C \approx 53$ cm s^{-1} , $r \approx 0.027\omega$ and $\lambda = 0$ are used, corresponding to a damping time scale of about 200 days.

The along-beam average between z_{max} and z_{min} of the nonlinear terms of Eq. (4.27) are plotted in Fig. 4.13. The analytical solution succeeds again to reproduce these terms although it tends to underestimate their magnitude as well as their meridional scale. The spatial structure is similar to that in the inviscid beam case, the main changes being notable differences in amplitude between the two edges of the beam in F_x, F_y and F_ρ. As noted in Section 4.6.3, such imbalance between the two edges of the beam is enough to produce mean zonal flows to the west of the beam.

The resulting mean Eulerian zonal and vertical flows are compared in Fig. 4.14 between the numerical and analytical solutions. The analytical solution predicts the overall shape of the mean flows of the numerical solution. In particular, the addition of dissipation is essential in getting mean zonal flows outside the beam. In the analytical solution, the zonal flows to the west of the beam are independent of x, but in the numerical simulation they decay slowly to the west.

The vertical structure of U_E and W_E between z_{max} and z_{min} is similar between the analytical and numerical solutions within the beam (Fig. 4.15). The main difference is that although the amplitude in the analytical solution simply decays with depth, that in the numerical solution has local maxima near 1500 m. Outside the beam, the mean zonal Eulerian flow between 1400 and 2250 m in the analytical solution is consistent with the numerical solution (Fig. 4.17); it misses however the complex meridional and vertical structure appearing above 1400 m depth.

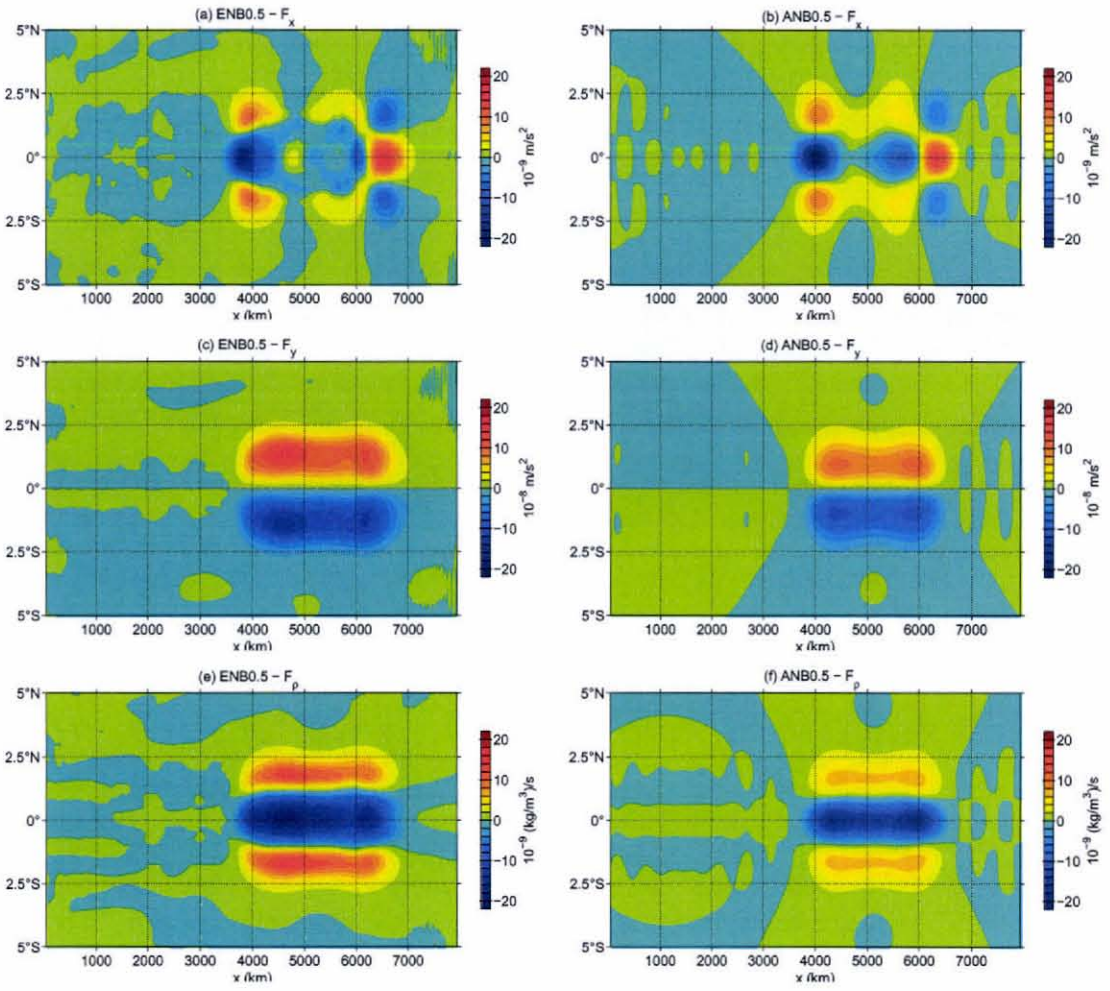

Figure 4.13: Mean nonlinear terms of Eq. (4.27) along-beam averaged between z_{max} and z_{min} and from years 7–9 in ENB0.5 (left) and ANB0.5 (right): F_x (upper), F_y (middle) and F_ρ (lower).

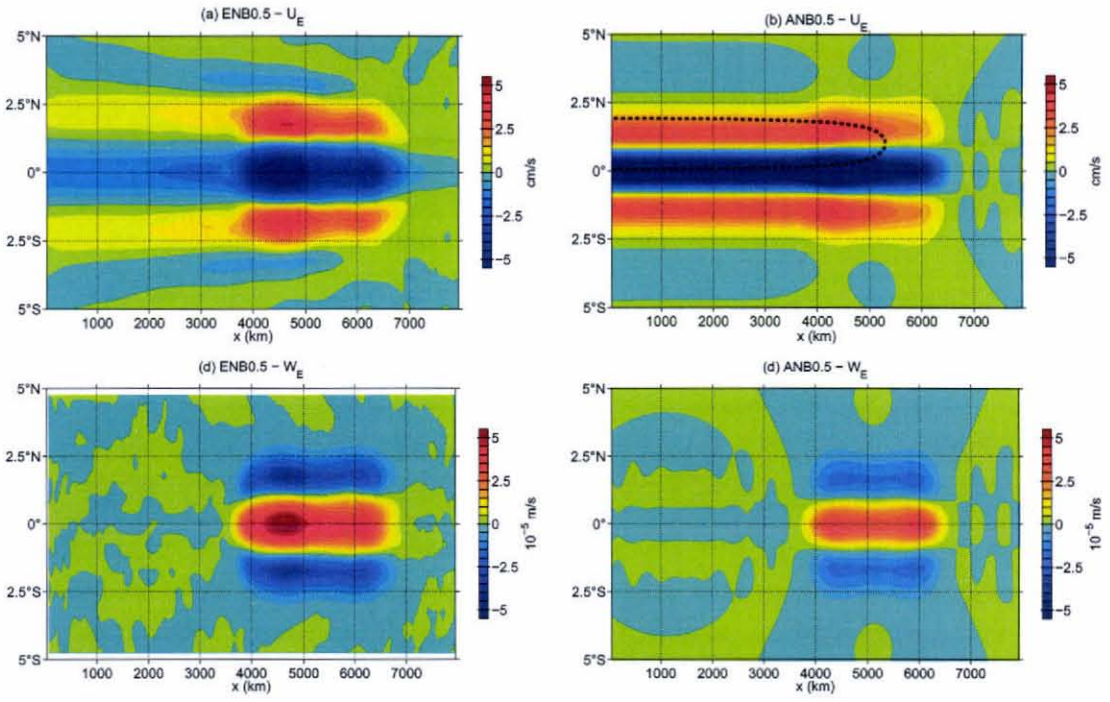

Figure 4.14: Mean Eulerian velocity field along-beam averaged between z_{max} and z_{min} and from years 7–9 in ENB0.5 (left) and ANB0.5 (right): U_E (upper) and W_E (lower). The dashed black line in (b) shows an example of a trajectory of a water particle smoothed over the time scale of the Yanai wave.

There are differences and similarities also in the amplitude and meridional structure between the TEJs in the analytical solution and those in the numerical one. The amplitudes of the zonal and vertical Eulerian components obtained in the analytical solution within the beam are similar to those found in the numerical solution (Fig. 4.15), the difference visible in the along-beam average (Fig. 4.16) being mainly due to the difference in vertical structure. The meridional Eulerian component is, however, significantly overestimated in the analytical solution. The eastward TEJs are also found closer to the equator by about $1/4°$ in the analytical solution. Outside the beam, the analytical solution overestimates the mean zonal Eulerian component

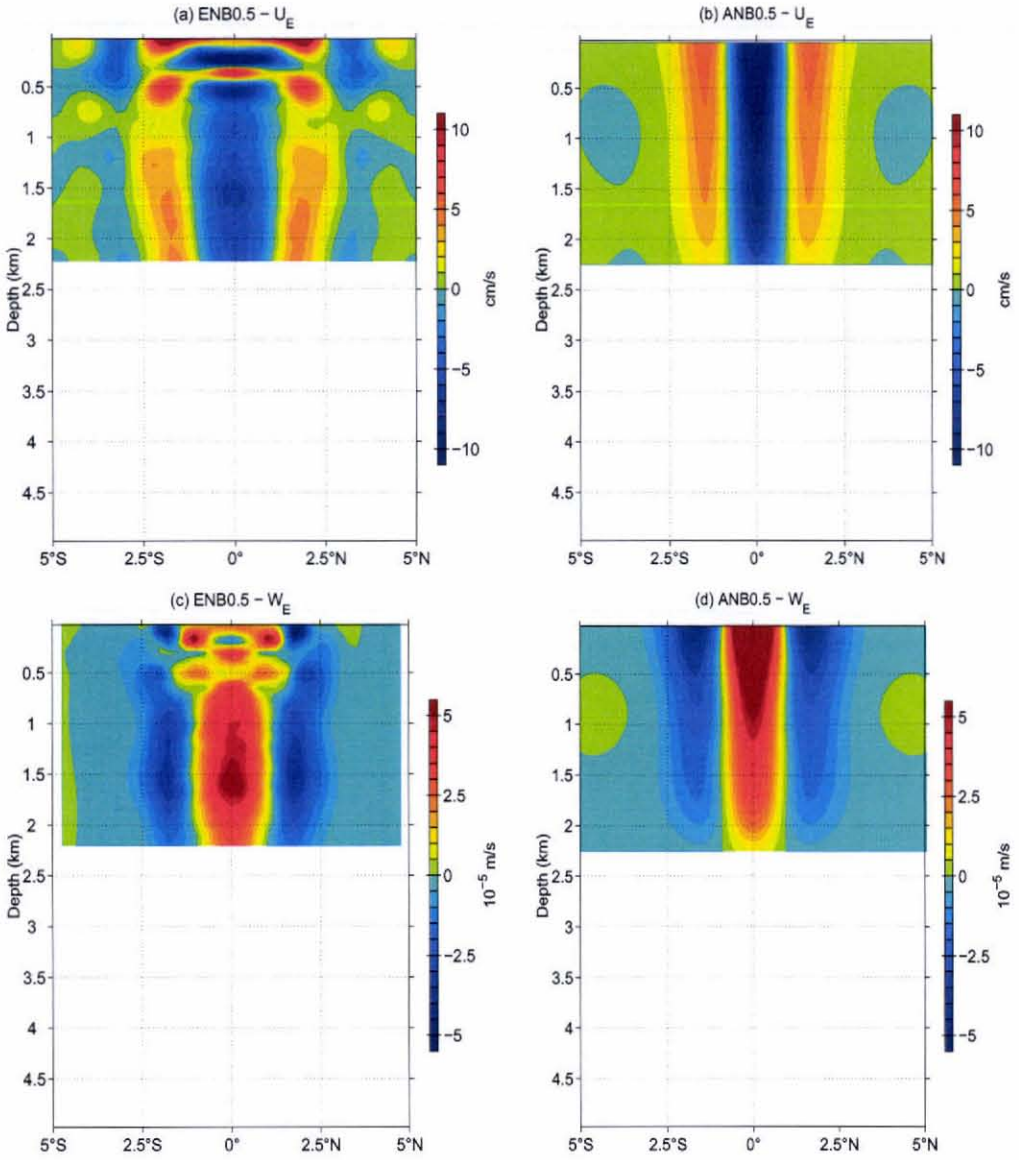

Figure 4.15: Mean Eulerian velocity field at $x = 5000$ km (within the beam) and from years 7–9 in ENB0.5 (left) and ANB0.5 (right): U_E (upper) and W_E (lower).

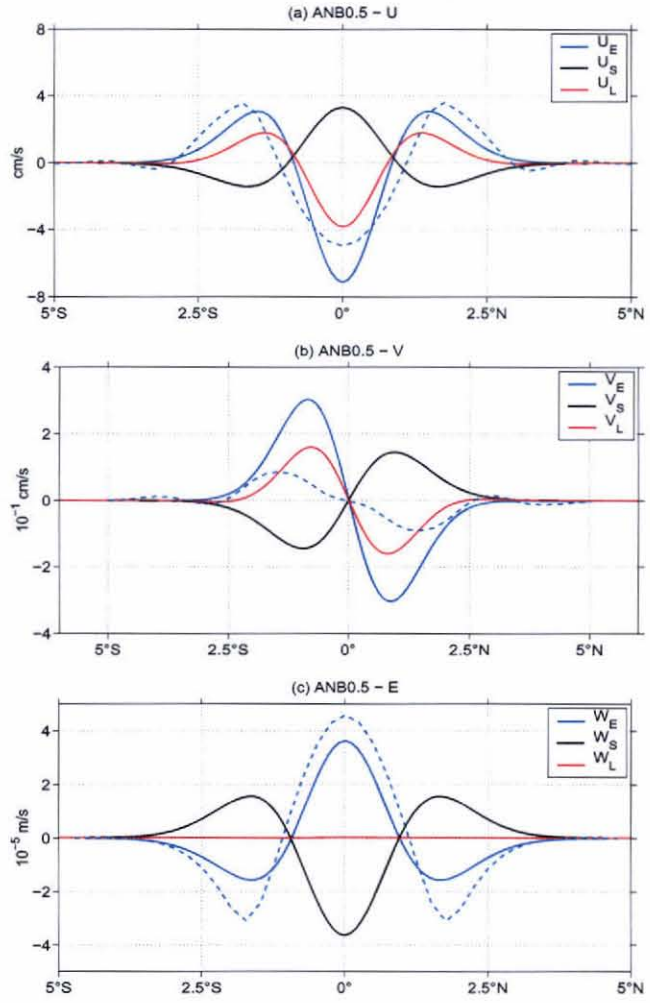

Figure 4.16: Eulerian-mean, Stokes-drift and Lagrangian-mean components in ANB0.5 along-beam averaged between z_{max} and z_{min} as well as within the beam. The mean Eulerian components from ENB0.5 are plotted with dashed blue lines.

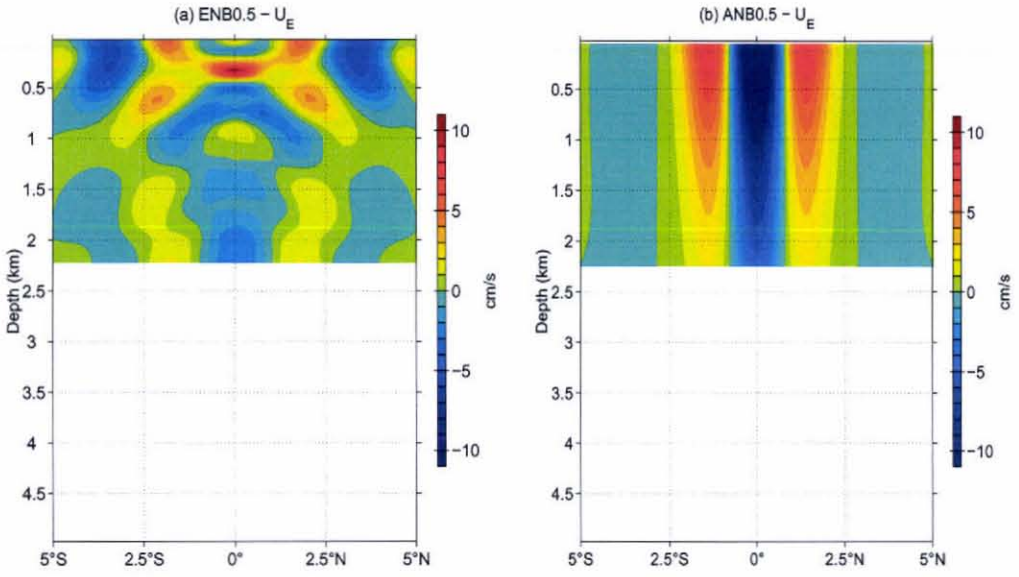

Figure 4.17: Mean Eulerian zonal velocity U_E at $x = 2000$ km (west of the beam) and from years 7–9 in ENB0.5 (left) and from ANB0.5 (right).

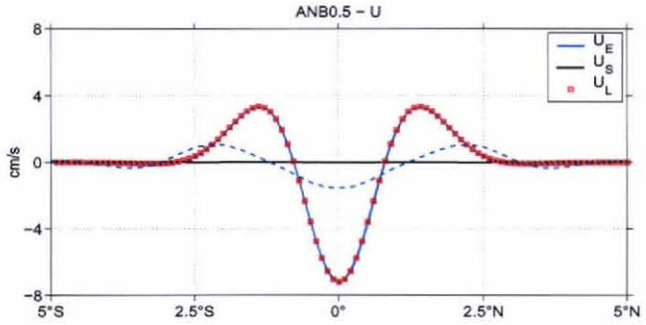

Figure 4.18: Zonal Eulerian-mean, Stokes-drift and Lagrangian-mean components in ANB0.5 along-beam averaged between z_{max} and z_{min} and between $x = 1000$ and 3000 km (outside the beam). The mean Eulerian zonal component from ENB0.5 is plotted with a dashed blue line.

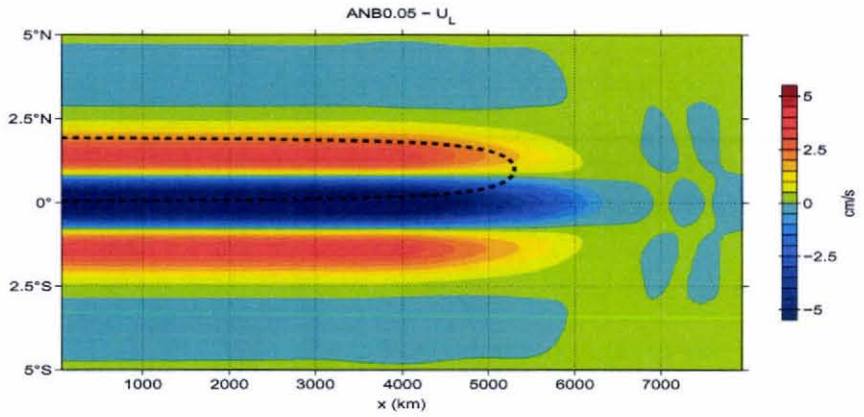

Figure 4.19: Mean zonal Lagrangian flow along-beam averaged between z_{max} and z_{min} in ANB0.5. The dashed line is the same as in Fig. 4.14b.

by more than a factor of 3 and the positions of the eastward TEJs are also closer to the equator by about 0.7° (Fig. 4.18).

Unlike in the case of the inviscid beam, the dissipation of the Yanai beam provides a source of PV which enables water parcels to change latitude and to form a gyre closed within the beam (Fig. 4.19). The gyre can then be closed at the western boundary as in the case of the Sverdrup circulation. A typical trajectory for a water particle *smoothed over the time scale of the Yanai wave* is plotted in Figs. 4.14b and 4.19. The particle moves eastward in one of the eastward TEJs without changing its PV; once within the beam, the particle changes its PV and slowly migrates meridionally where it can join one of the westward TEJs; it then escapes the beam and moves westward again at constant PV. In Appendix B.2, a Lagrangian point of view based on the work by Andrews and McIntyre (1978) is adopted and enables to deduce an explicit relation between the meridional displacement V_L and the dissipation. In particular, it is shown that V_L is negatively proportional to the Lagrangian mean of ζ/h where ζ is the relative vorticity and h the thickness of the water column. One component of that quantity is ζ_L, the Lagrangian mean relative vorticity which is

the averaged relative vorticity of a water parcel over a wave cycle due to the presence of the mean flow and the wave field. It is further shown that V_L can be deduced in first approximation from the first-order inviscid wave solution.

Because, in the regime of weak dissipation studied, the structure of the Stokes drift $\overrightarrow{U_S}$ is nearly the same with or without dissipation, $-\overrightarrow{U_S}$ can still be seen as the mean Eulerian component without dissipation $\overrightarrow{U_E}^{inviscid}$. The mean Eulerian flow obtained in the viscid case can then be interpreted as the sum of the Eulerian component without dissipation plus a new mean Lagrangian component entirely due to the presence of dissipation:

$$\overrightarrow{U_E}^{viscid} \approx \overrightarrow{U_E}^{inviscid} + \overrightarrow{U_L}. \tag{4.42}$$

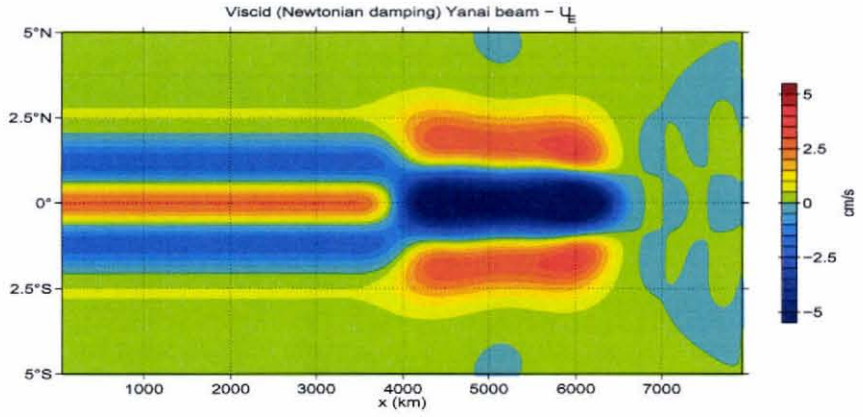

Figure 4.20: Mean zonal Eulerian flow along-beam averaged between z_{max} and z_{min} in the case of a Yanai beam dissipated by Newtonian damping ($r = 0$ and $\lambda \approx 0.027\omega$).

When Newtonian damping alone is used, mean zonal Eulerian flows are found within and to the west of the beam as in the case of Rayleigh friction (Fig. 4.20). The mean zonal Eulerian flow outside the beam does not, however, resemble the TEJs and is rather consistent with the mean zonal Eulerian flow found in the case of the Yanai wave dissipated by Newtonian damping (Section 4.6.2), suggesting again

that dissipation of momentum and not of heat is the key to produce TEJ-like currents all across the basin.

4.7 Sensitivity

In this section, the sensitivity of the analytical solution in the case of the Yanai beam dissipated by Rayleigh friction is explored. Fig. 4.21a shows the evolution of the meridional profile of the mean Eulerian zonal flow U_E to the west of the beam at 1500 m depth when the coefficient of Rayleigh friction increases. All other values are those used in ANB0.5. Without friction ($r = 0$), there is no flow outside the beam consistent with the non-acceleration theorem. With increasing dissipation, the mean flow strenghtens until an optimal value r_{opt} is reached. The time scale associated with r_{opt} corresponds to about 175 days at 1500 m, decreasing exponentially for shallower depths. For stronger dissipation, the mean flow decreases until it completely vanishes for larger values of dissipation. The particular value of dissipation r_{opt} corresponds thus to a balance where dissipation is strong enough to provide the change of PV within the beam and trigger zonal flows outside the beam but not too strong to allow enough energy of the beam to reach the deep ocean.

The amplitude of the westward off-equatorial TEJs stays weak for all values of dissipation. Also, the meridional structure is relatively insensitive to the strength of dissipation. Thus, the noticeable deviations in the amplitude and meridional structure of the TEJs between the analytical and numerical solutions cannot be explained by a poor estimate of the strength of the Rayleigh friction.

Figs. 4.21b and c show the sensitivity of the solution to the central zonal wavelength and central period of the beam respectively. A shorter zonal wavelength or period corresponds to a lower baroclinic mode, that is a larger C. Thus for the same absolute amplitude $C\epsilon_0$, a Yanai wave with a shorter zonal wavelength or period has

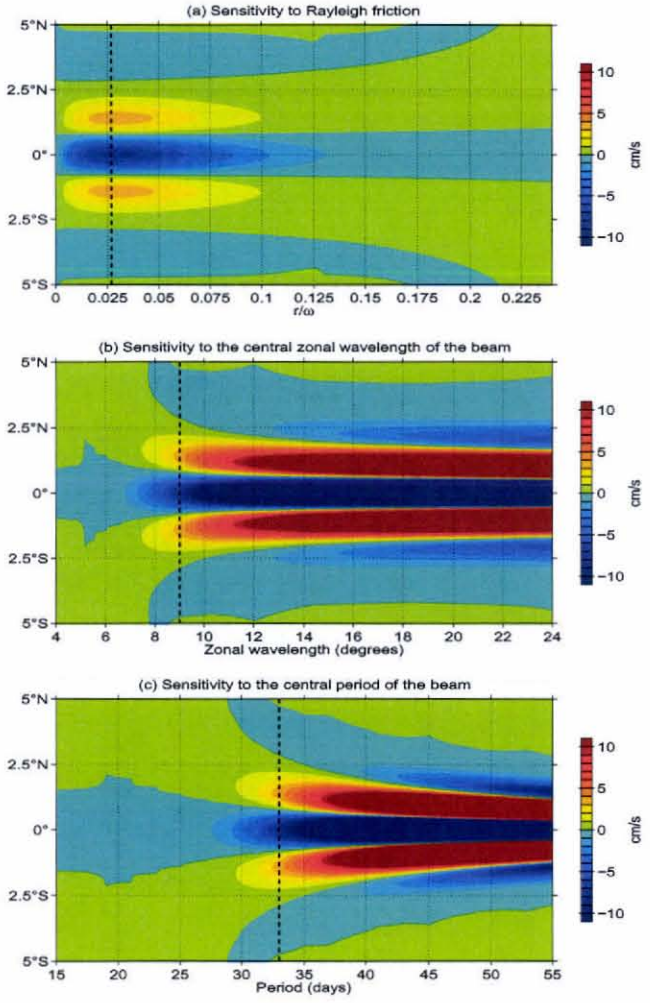

Figure 4.21: Sensitivity of the Eulerian mean zonal flow at $x = 0$ (west of the beam) and 1500 m to the values of (a) the coefficient of Rayleigh friction, (b) the central zonal wavelength of the beam and (c) the central period of the beam. In (a), all other values are those used for the solution ANB0.5. It is also the case in (b) and (c) except that the value of ϵ_0 is adjusted to keep the absolute amplitude $\mathcal{C}\epsilon_0$ constant, $\mathcal{C}$ varying with the wave frequency and zonal wavenumber. The solution ANB0.5 is shown by a black dashed line in every case.

a weaker ϵ_0: it is thus less nonlinear and triggers weaker zonal flows. With longer central zonal wavelength or period, the amplitude of the mean flows increases, in particular the westward off-equatorial TEJs which exceed several cm s^{-1} for a zonal wavelength of at least 24° or a period of a least 55 days. The meridional position of the TEJs moves equatorward with longer central zonal wavelength and period.

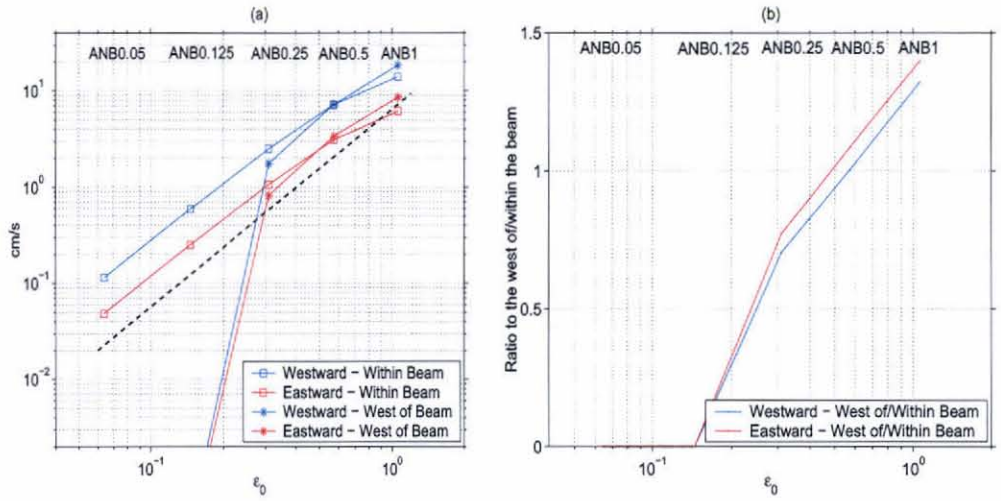

Figure 4.22: (a) Amplitude of the TEJs within (square) and to the west of (star) the beam in the analytical solutions ANB0.05 to ANB1. The amplitude is defined as in Fig. 3.19. (b) Ratio of the amplitude of the TEJs to the west of/within the beam. In both panels, red corresponds to the eastward TEJ north of 1°N and blue to the westward equatorial TEJ within 1° from the equator. The dashed line in (a) shows the slope corresponding to a quadratic evolution. Compare to Fig. 3.19.

Overall, it is possible that the differences in amplitude and meridional positions of the TEJs between the analytical and numerical solutions may be explained by the presence of other waves in the latter. Indeed, in ENB0.5, a heterogenous and large set of high-frequency waves exists (see Appendix A.1) and may have contributed to these differences.

In Section 3.4.2, it was observed that the amplitude of the TEJs within the beam evolves quadratically with the amplitude of the beam for weak forcing, but weaker than expected based on a quadratic relationship for stronger forcing (Fig. 3.19a). The evolution of the amplitude of the westward equatorial TEJ and northern eastward TEJ within the beam for the series of analytical solutions following the series of numerical solutions are plotted in Fig. 4.22a; in each case, the value of the dissipation has been adjusted so that the analytical profile of the Yanai beam fits the numerical one. The evolution is qualitatively similar to that in the numerical case (Fig. 3.19), especially in the change from quadratic to quasi-quadratic evolution between the cases with weak and strong forcing. The same calculation varying the amplitude of the beam but keeping the dissipation constant between the solutions results in a quadratic relationship everywhere suggesting that the deviation from the quadratic law is due entirely to the increase of the dissipation with the beam amplitude.

Because virtually no effective dissipation is found for the cases with weak forcing (ENB0.05 and ENB0.125), the amplitude of the TEJs to the west of the beam in the corresponding analytical solutions are exactly zero (ANB0.05 and ANB0.125). This is consistent with the idea that the mean flows to the west of the beam in ENB0.05 and ENB0.125 should not be regarded as genuine TEJs.

In the cases with moderate, standard and strong forcing, although the amplitude of the TEJs to the west of the beam obtained in the analytical solutions overestimate those obtained in the numerical solutions, the evolution is qualitatively similar: the increase in amplitude between the moderate and standard cases is larger than between the standard and strong cases as in the numerical experiments (Fig. 3.19a).

The amplitude of the TEJs to the west of the beam relative to those within the beam differs, however, from the numerical cases (Figs. 3.19b and 4.22b). Although it reaches only 15 to 30% of the amplitude of the TEJs within the beam in the numerical

cases, it reaches 75 to 140% in the analytical case. An amplitude larger to the west than within the beam is surprising. It does not appear in the horizontal structure of Fig. 4.14b and is simply an artifact of the zonal average performed within the beam which smears out the large values near the western edge with the weak values of the eastern edge.

4.8 Conclusions

The conclusions from the analytical study are:

- *the second-order mean Eulerian and Lagrangian flows and associated Stokes drift resulting from a Yanai wave dissipated in the vertical, either in the configuration of a single plane wave or a beam, have been derived; mean Eulerian flows resembling the TEJs are found with Rayleigh friction, but not with Newtonian cooling;*

- *the mean flows are constrained to the beam without dissipation but are found within and everywhere to the west of the beam when dissipation is included; such dependence on the presence of dissipation is in accord with the non-acceleration theorem;*

- *the inviscid analytical solution ANB0.05 fits nearly perfectly the numerical solution ENB0.05 where the effective dissipation of the beam is negligible, while the viscid analytical solution ANB0.5 fits only qualitatively the numerical solution ENB0.5 where the effective dissipation is relatively strong;*

- *in the latter case, the analytical solution deviates significantly from the numerical solution in terms of amplitude and meridional positions of the jets; in particular, the TEJs to the west of the beam are stronger and closer to the*

equator than those obtained in the numerical solution; these differences may be due to the heterogeneous set of high-frequency waves found in the numerical solution but not included in the analytical one;

- *the analytical solution is, however, robust with respect to the values of Rayleigh friction and the central zonal wavelength and period of the Yanai beam; as long as the dissipation is independent of the beam amplitude, the amplitude of the TEJs increases quadratically with the beam amplitude; the increase of the dissipation with the beam amplitude could thus explain the deviation from a quadratic law observed in the numerical experiments at strong forcing.*

The model shortcomings as well as possible improvements are discussed in Chapter 5.

Chapter 5

Discussion and conclusion

This study shows that a monthly-periodic, westward-propagating and moderate-zonal-wavenumber Yanai beam produces a set of large-vertical-scale currents resembling the TEJs. The TEJs have two components. One component exactly cancels the Stokes drift of the Yanai beam. It exists only within the beam and is not associated with any transport of mass. A second component exists only for realistic amplitude. In that case, an instability occurs within the beam, draining energy toward mostly small vertical scales where it is dissipated. Such dissipation of the beam in the vertical triggers the second component that has a similar meridional profile than the first one. The associated currents are found within and everywhere to the west of the beam. Equatorward transport of mass within the beam connects the eastward transport near 2° from the equator to the westward transport at the equator. The currents are robust to changes in model configuration and forcing. In particular, the Yanai beam does not have to be perfectly harmonic but can have a broad spectrum in space and time. Finally, the currents can be predicted analytically from the second-order rectification of the linear Yanai beam solution.

The Yanai beam is believed to be generated by the instabilities of the surface equatorial currents, but we are aware of no detailed study of this process. The

few available observations and numerical studies all support the presence of such a Yanai beam in the Pacific Ocean; evidence of a Yanai beam in the Atlantic is less clear. Moored current meter observations below the thermocline over several years show a peak at the monthly period in meridional velocity in the eastern Pacific and Atlantic oceans that investigators have associated with Yanai waves. A Yanai beam has been identified in regional numerical models of the tropical Pacific. We confirm here the presence of a broad, robust and energetic beam in the eastern Pacific of an OGCM, the JAMSTEC model, along with with the presence in that basin of a large-vertical-scale circulation resembling the TEJs. Analysis of the turbulent PV equation reveals that the eddy PV fluxes are indeed dominated by the fluctuations due to the Yanai beam. In the eastern Atlantic, a Yanai beam has also been deduced from the few available observations but it appears as a much narrower and weaker beam located in the *western* Atlantic in numerical models. In the JAMSTEC model, that weak beam coincides with the absence of a TEJ-like structure, consistent with the idea that the Yanai beam might be one important source for the TEJs. More generally, the absence or weakness of the Yanai beam in OGCMs could simply explain the absence or weakness of the TEJs in OGCMs. A thorough comparison of the high-frequency meridional motions below the thermocline and their relation to the deep mean circulation between different OGCMs would be needed to verify of that explanation.

The study also explores several effects of model configuration on the structure of the TEJs. First, TEJs are found to be robust with respect to the grid resolution. Their amplitude increases only weakly with the ratio $\Delta x/\Delta z$, but the proportional increase is greater for flow to the west of the beam than for the stronger flow within the beam. It is not clear why the amplitude correlates better with $\Delta x/\Delta z$ than with Δx or Δz individually. The grid resolution may probably play a role in the

instability of the beam and its subsequent dissipation. Unfortunately, we did not archive enough output of the simulations with different grid resolutions to study such a relation.

We have also studied briefly the sensitivity of the numerical solution to the strength of the explicit dissipation. Two other numerical simulations not reported here have also been performed: they are similar in all aspects to ENB0.5_LV except that the background coefficient for the vertical diffusion of momentum was multiplied by 10 and 0.1 respectively, while keeping the same coefficient for the diffusion of tracers. With weaker diffusivity, the mean flows are virtually identical to those obtained in ENB0.5_LV. With stronger diffusivity, the mean flows are 10 to 20% weaker but their meridional structure is unchanged, within and to the west of the beam. Hence, the process generating the mean flows is insensitive to the level of explicit vertical diffusion of momentum. Sensitivity to vertical diffusivity of heat was not tested, however; because the stratification stays constant over most of the water column in all numerical simulations, we do not expect that vertical heat diffusion plays any significant role.

The advective term is a key to the transfer of energy and PV toward small scales. It has been shown recently that OGCMs with different advective schemes can produce different mean circulations (Barnier *et al.* 2006; Penduff *et al.* 2007); in particular a model with a scheme conserving energy *and* potential enstrophy was shown to reproduce a more realistic circulation in regions of strong eddy-topography interactions than a model with a scheme conserving the energy alone. The equatorial circulation is, however, not significantly different between the two models (Penduff, personal communication 2008). This result suggests that the choice of the advective scheme may not be critical to the formation of the TEJs but a similar comparison for the present idealized simulations would ne needed to confirm this conclusion.

A drawback of the present numerical solutions is that they underestimate the amplitude of the TEJs even in the experiments forced with the strongest beam amplitude, and that amplitude is itself higher than observed. A possible explanation is that the numerical model fails to handle correctly the actual instability and subsequent dissipation of the beam, suggested for instance by the weak dependence of the TEJs amplitude on the grid resolution. Another explanation could be the presence of other equatorial waves that contribute to the formation of the TEJs but have not been included here. One example is the first-baroclinic and first-meridional mode Rossby wave that is also present in observations and numerical studies. It could be interesting to study its nonlinear rectification alone and in combination with the Yanai beam.

The instability of the Yanai wave, which is essential to spread the energy toward small vertical scales in the numerical simulations, is described in detail in Appendix A.1 but its nature and cause have not been identified. Although dOrg07 and Hua08 describe an instability of a Yanai wave, the secondary high-frequency motions involved in their study are different from those observed in the present numerical simulations. It might still be that the instability analysed in these previous works is similar in principle to the one observed in the present study but differences arise because a *vertical mode*, that is *the sum of two waves propagating in opposite direction in the vertical*, is considered in the former case, while a *vertically-propagating beam*, that is *the sum of waves propagating nearly in the same direction*, is considered in our case. Such a difference could explain also why dOrg07 and Hua08 did not observe the instability of the Yanai wave for moderate zonal wavenumber as we did.

The study did not address the variability of the TEJs. Observations in the central Pacific suggest that the TEJs are superimposed on the annual Rossby wave

propagating downward along a shallow angle (Firing 1987). Until recently, mean TEJs in the Altantic had been inferred from synoptic sections sparse in time and were suspected to be the result of a bias from seasonal Rossby waves (Jochum and Malanotte-Rizzoli 2003), which would have explained their absence in numerical models. Unbiased datasets now show, however, that the mean TEJs exist and are superimposed on the seasonal Rossby waves (Ollitrault *et al.* 2006; Brandt *et al.* 2008). In both the Pacific and Atlantic oceans, the seasonal variability propagates downward from the surface, making it more difficult to test the prediction of the present theory that the annual variability of the Yanai beam would cause annual variability of the TEJs.

Finally, as described in Appendix A.2, the numerical simulations reproduce a set of mean currents resembling the EDJs in the upper 1000 m of the water column. In the runs with moderate, standard and strong forcing, the EDJs-like currents appear at the transition zone between the surface and 1000 m depth over which the Yanai beam deviates significantly from exponential decay. At those depths, nonlinear processes are responsible for the EDJs but their cause have yet to be clarified. In the experiments with weak forcing, the set of EDJs that is found down to 2000 m seems to be related to the presence of IG waves. Preliminary results support the hypothesis that the Yanai beam and the IG wave interact to produce a mean flow resembling the EDJs. Indeed, the theory correctly predicts the different vertical wavelength obtained for the EDJs in the experiments. For both the cases of weak and stronger forcing, however, the proximity of the surface, which has to be considered as an artificial boundary here, prevents us from concluding if these currents are genuine EDJs or not.

This study motivates several possible projects. Two observational programs could be imagined to test the present theory. First, a moored current meter array could

measure the characteristics of the Yanai wave activity and test the prediction of a vertical decay in amplitude and a cascade of energy toward mostly small vertical scales. This observational program would also measure the activity of IG waves and their possible role in the formation of the EDJs. Second, a deployment of isopycnal RAFOS floats could test the prediction that transports are connected by equatorward flow within the Yanai beam. From the theoretical point of view, it would be interesting to apply the present theory to other equatorial waves such as the first-baroclinic and first-meridional Rossby mode seen in observations and numerical models and to understand the nature and cause of the Yanai beam instability in light of Hua08's work. Finally, from a modelling point of view, analysis of the Yanai wave activity and its relation to model configuration and the presence or not of the TEJs in different numerical models would help to understand the necessary and sufficient ingredients to reproduce the TEJs in OGCMs.

Appendix A

Numerical solutions

A.1 Cause of beam dissipation with depth

In this section, it is shown that the decay of the beam in the vertical is caused by other low and high-frequency waves which arise from a complex set of nonlinear interactions starting with the Yanai beam. Some of the beam energy flows to small vertical and horizontal scales where it is dissipated. The dissipation occurs mainly within the beam (Fig. 3.8). In the analytical solution, those waves have not been taken into account and only their net effect, that is the vertical decay of the beam, has been considered and parameterized by the simple Rayleigh friction $\vec{\mathcal{D}}$ (Section 3.3 and Chapter 4).

In the experiments with weak forcing (ENB0.05 and ENB0.125) the amount of kinetic energy found outside the forcing frequency represents less than 2% of the total kinetic energy (Fig. A.1). With moderate, standard and strong forcing (ENB0.25, ENB0.5, ENB1), however, this amount rises to 17, 23 and 30% respectively. While the energy is distributed continuously over the frequency and wavenumber space in experiments with standard and strong forcing (Fig. 3.6), it appears over a set of *discrete* peaks with moderate forcing (ENB0.25). As shown below, these peaks are

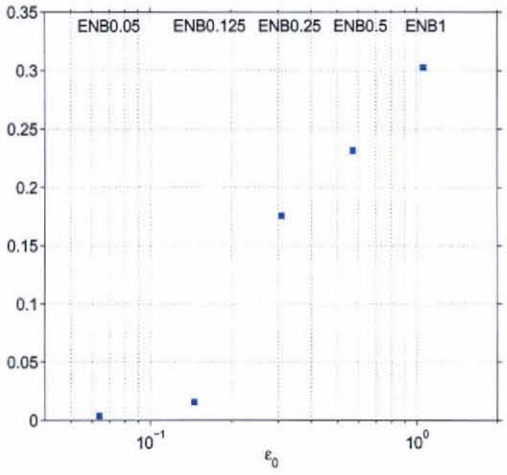

Figure A.1: Ratio of the kinetic energy found outside the frequency band 0.025–0.035 cpdays to the total kinetic energy (corresponding to about 28.6–40 day periods) over years 7–9 at the equator and averaged between the two edges of the beam and between 1000 and 3000 m.

associated with different families of either low or high-frequency motions. Therefore, ENB0.25 exposes the nonlinear interactions responsible for the spread of energy over time and space.

Fig. A.2 shows the 2D spectra in zonal wavenumber and frequency and those in vertical wavenumber and frequency for equatorial U and V. The self-interaction of the Yanai wave directly forced by the surface stress (Fig. A.2; red dot) yields a mean flow (black dot) as shown analytically in Chapter 4.

Another component of the self-interaction is a "$2\omega_0$" wave with twice the frequency and wavenumber of the Yanai beam (Fig. A.2; green dot) consistent with nonlinear triad interactions (Ripa 1982). A snapshot of equatorial U (Fig. A.3) illustrates its structure. It is a westward-propagating IG wave with the energy propagating downward at about 900 m/month and to the west. Its meridional structure

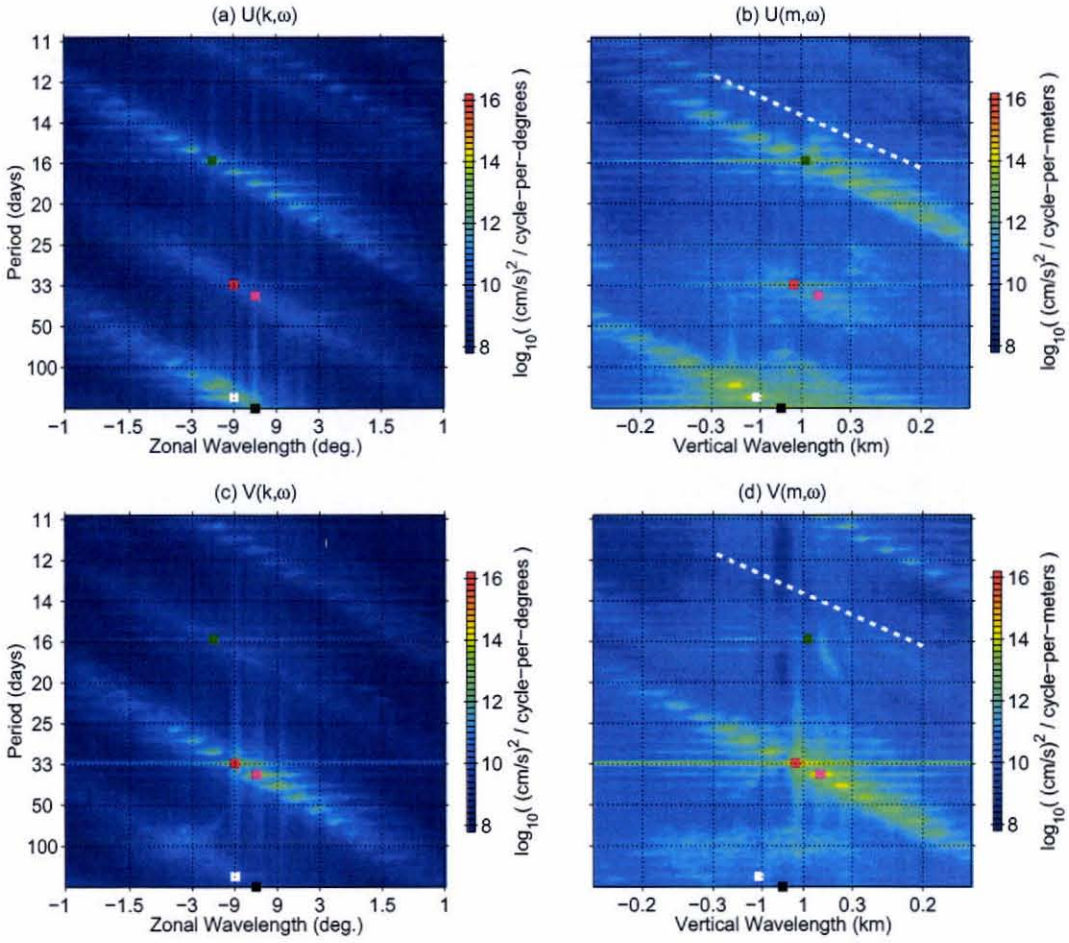

Figure A.2: Power spectra in k-ω (left) and m-ω (right) of equatorial U (top) and V (bottom) over years 7 to 9 in experiment ENB0.25. The k-ω spectra have been averaged between 1000 and 3000 m and the m-ω spectra between $x = 4000$ and 7000 km. The dots correspond to the wave motions described in the text: directly-forced Yanai wave (red), 36-day Yanai wave (magenta), $2\omega_o$ wave (green), low-frequency wave (white). The black dot corresponds to the mean uniform flow and the dash white line in (b) is a parallel to the wavevector of the low-frequency motion.

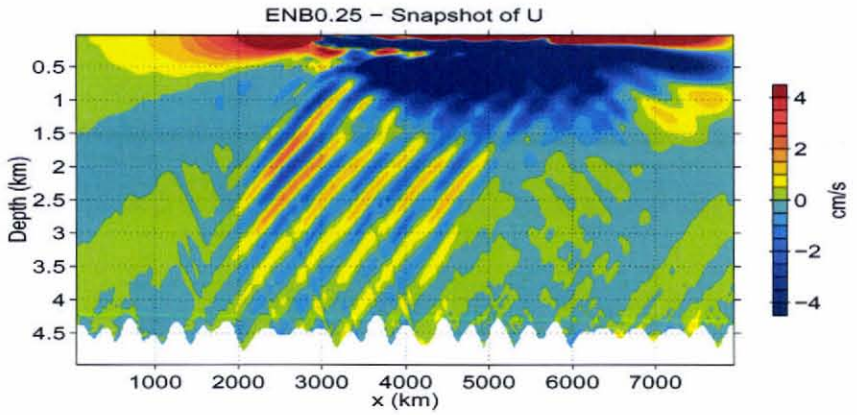

Figure A.3: Equatorial U in ENB0.25 on May 1, 00, about one month after the beam has reached the bottom. The velocity has been multiplied by τ_0/τ.

corresponds to an odd meridional mode, symmetric in U about the equator so it appears in the equatorial U spectra (Figs. A.2a and b) but not in equatorial V. The irregular bottom topography described in Section 3.2 reduces the reflection of this IG wave (Fig. A.3).

The energy of the $2\omega_0$ wave has also spread along a band in the frequency and wavenumber spectra, the slope of which is plotted with a dashed white line in Figs. A.2b and d. Within that band, the energy is concentrated in discrete peaks mostly toward lower frequencies and higher vertical wavenumbers. Unlike the $2\omega_0$ wave, these peaks do not correspond to any free wave.

Another band of energy is centered at the peak of the directly-forced Yanai wave (Figs. A.2c and d). It is distributed over a set of peaks aligned along the same slope as the previous band. The strongest peak is shown by the magenta dot in Fig. A.2. It corresponds to a Yanai wave of 36-day period, about 550-m vertical wavelength, and near zero zonal wavelength (Fig. A.4). Because the frequency of the 36-day Yanai wave is close to that of the directly-forced Yanai wave, both propagate energy along nearly the same slope in the x-z plane. The difference in frequencies between

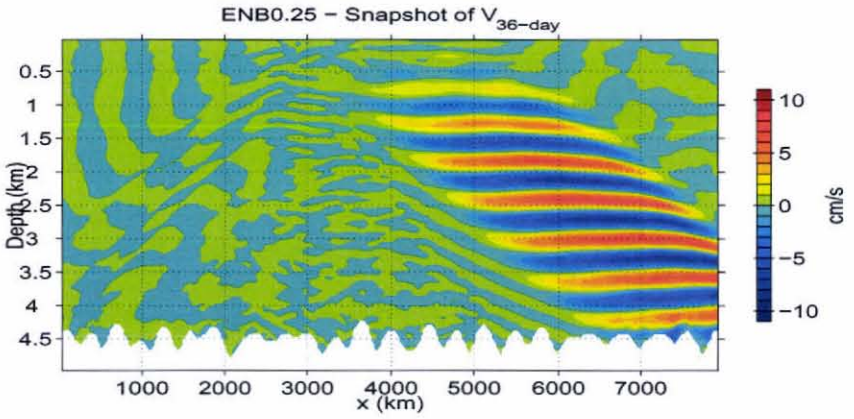

Figure A.4: Equatorial V in ENB0.25 on January 1, 07, for the frequency band near the 36-day period. The velocity has been multiplied by τ_0/τ.

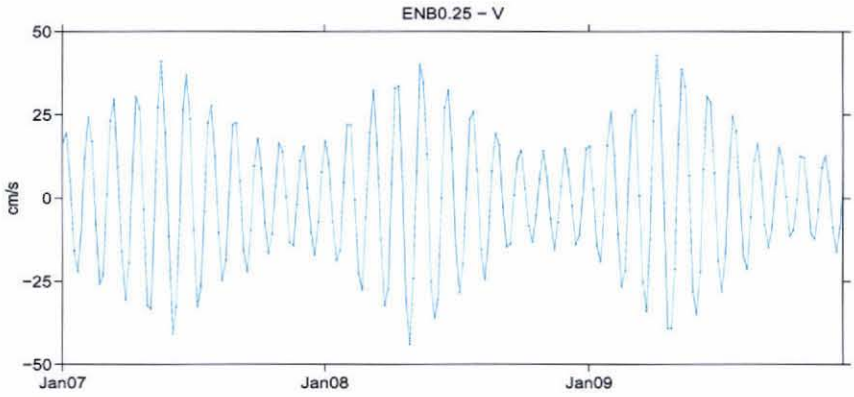

Figure A.5: Time series of equatorial V near 2000 m depth and $x = 6500$ km, and normalized by τ_0/τ in ENB0.25.

the two waves corresponds to a period of about one year and explains the near-annual modulation of the total V field in ENB0.25, ENB0.5, ENB1 (Fig. A.5). As in the previous case, the energy is spread mostly toward lower frequencies and higher wavenumbers at peaks that do not correspond to any free wave. Such dramatic increase in small vertical scales with moderate and standard forcing is illustrated in Fig. A.6. Notice in that figure that some vertical scales are close to that of the grid scale where explicit dissipation acts.

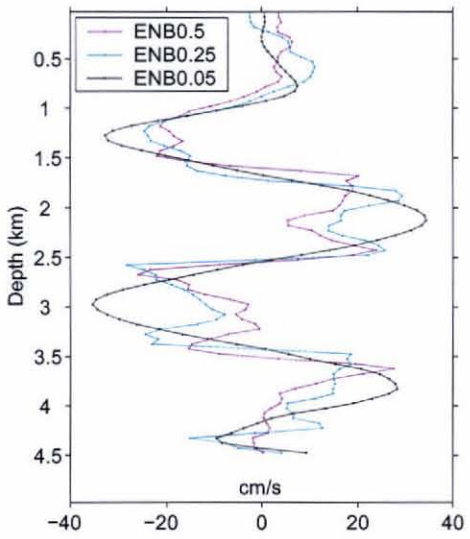

Figure A.6: Vertical profiles of equatorial V on Jan. 1, 08 near $x = 6500$ km and normalized by τ_0/τ in ENB0.5, ENB0.25 and ENB0.05.

How does the energy spread to the different peaks in frequency and wavenumber space? The answer to this question may lie in the low-frequency motion appearing in the different spectra of Fig. A.2 (white dot). Such motion is the cause for the near-annual modulation of the mean zonal flow discussed in Section 3.4.1. What is shown here is that the motion also seems to play a central role in the transfer of energy from one high-frequency wave to another.

The low-frequency motion has a period of about one year, half the vertical wavelength and about the same zonal wavelength as the directly-forced Yanai wave. Its "wavevector" $\vec{\varphi}_{LF} = (k, m, \omega)$ is thus parallel to the different linear bands of energy in frequency and wavenumber space. Furthermore, the "distance" between neighboring peaks within each band corresponds to the length of $\vec{\varphi}_{LF}$. Analogous properties are observed in the case of the strong (shear) instability of mid-latitude Rossby waves (Gill 1974), suggesting that a similar nonlinear instability of the Yanai wave is occuring.

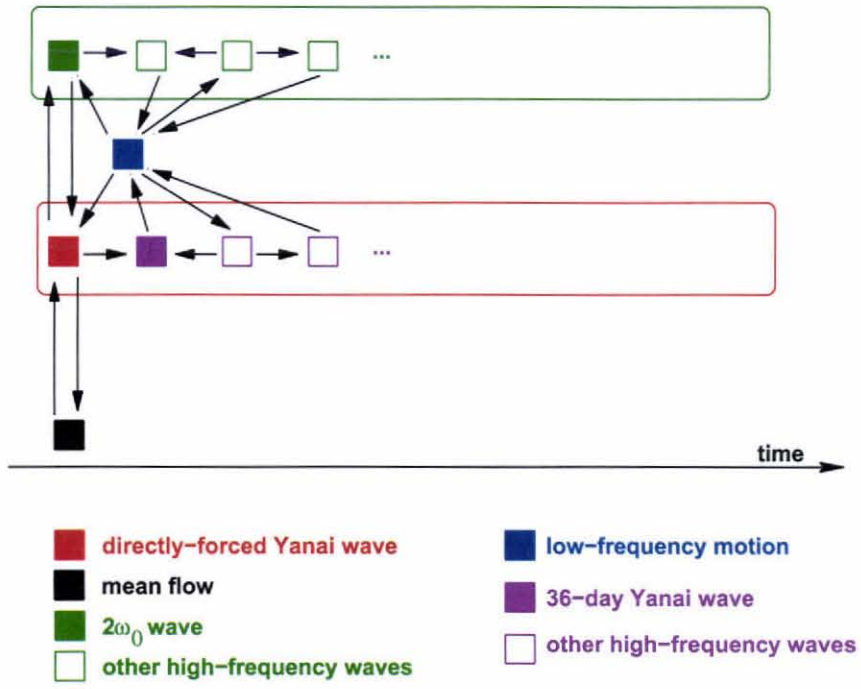

Figure A.7: Schematic of the *a priori* timeline of the nonlinear interactions occuring in ENB0.25. The vertical axis has no meaning and the direction of an arrow is arbitrary. With time, energy is being drained mostly toward lower frequencies and higher wavenumbers where it is dissipated.

The schema of Fig. A.7 recapitulates the possible timeline of the interactions oc-

curing in ENB0.25 based on the theory of nonlinear triad interactions. The directly-forced Yanai wave is self-interacting producing a mean flow as well as a $2\omega_0$ wave immediately. With moderate, standard and strong forcing, a low-frequency motion appears which then destabilizes into a series of high-frequency motions. With a few exceptions, those high-frequency motions do not correspond to free waves: they are forced locally and stay within the beam. The transfer of energy is also mostly from large to small-vertical scales (Fig. A.2) where it is dissipated. This is consistent with the observation that most of the dissipation occurs within the beam (Fig. 3.8).

Such a cascade is consistent with the increase of the vertical decay of the beam with its amplitude (Fig. 3.7). One can argue, for instance, that the stronger the amplitude of the Yanai wave, the stronger the nonlinear interactions, the more rapid the transfer of energy toward small scales, and the stronger the vertical decay. This explanation alone does not account, however, for the difference in decay seen between ENB1 and ENB0.5 (Fig. 3.7a): near 2000 m depth, the decay is stronger in ENB1 than in ENB0.5 while the local amplitude of the Yanai beam is similar. The energy of the low-frequency motion is, however, larger by about 30–40% in the first case than in the second case throughout the water column, which might explain the difference in decay rate. More work is needed to understand fully the direction and rate of the energy transfer throughout frequency and wavenumber space.

Another unanswered question is why and how the low-frequency motion arises in the first place. Hua08 demonstrates that a Yanai wave can destabilize into a structure associated with a high baroclinic mode and composed of a zonal Kelvin-like mean flow and Yanai-like motions. It is not clear if this process is what is occuring here, particularly because of the difference in geometry of the Yanai wave studied: the Yanai wave is a *vertical mode* in Hua08 while here it is a *vertically-propagating beam*. The set of high-frequency waves found in Hua08 is also qualitatively different from

those observed here. Computation of the growth rate of instability for a Yanai wave forming a beam, similar to the Hua08 calculation might explain why those low and high-frequency motions appear.

A.2 The upper 1000 m in the numerical solutions

The numerical simulations reproduce features loosely resembling the EDJs in the upper 1000 m of the water column. Because the relevance, if any, of these features to the ocean EDJs is questionable, we restrict ourselves here to their description and to a brief mention of two possible causes: the particular depth evolution of the amplitude of the Yanai beam within that depth range, the possible interaction with a directly-forced small-vertical-scale IG wave.

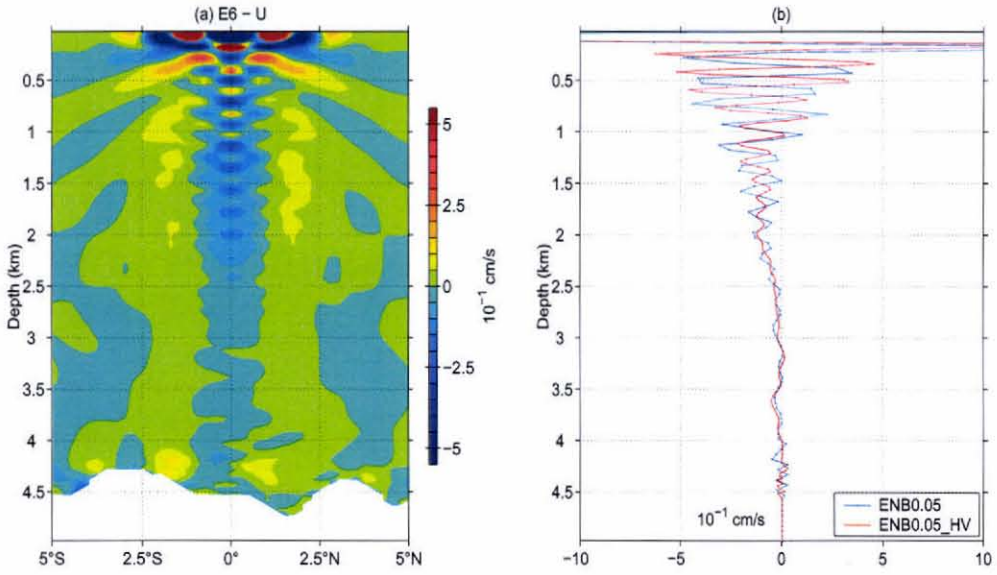

Figure A.8: (a) Mean U at $x = 5000$ km averaged over model years 7–9 in ENB0.05. Its equatorial profile is plotted in blue in (b). Plotted in red in (b) is the same equatorial profile but in the 200-level experiment ENB0.05_HV.

Relatively strong EDJ-like structure appears in all the numerical experiments. Except in ENB0.5_LV which does not have enough resolution, the structure is composed of at least four zonal equatorial jets: eastward near the surface and around 400 m, and westward near 150 m and 500 m (Figs. 3.11, 3.21 and 3.24). The equatorial jets are accompanied by an off-equatorial current structure: eastward flows near 2° off the equator with local maxima near the surface and around 500–600 m depth, and nearly surface-trapped westward flows near 4° off the equator. Finally, depending on the surface forcing, there are additional deeper equatorial jets appearing mainly to the west of the beam. The weaker the surface forcing, the more jets are found, the most extreme case being ENB0.05 with about a dozen jets appearing between the surface and 2000 m (Fig. A.8a).

Vertical wavelength also decreases with weaker forcing. The vertical wavelength of the jets varies between 300 to 600 m, which is within the range of observed vertical wavelengths in the Pacific and Atlantic oceans. In the experiments, it is relatively independent of longitude outside the beam, but it is in general larger to the west than to the east of the beam. The transition occurs within the beam where the vertical wavelength tends to decrease eastward and the jets migrate upward or downward. One consequence is that the surface equatorial flow is not always eastward but is at some locations replaced by the westward equatorial jet flowing below it. In the numerical experiments forced with the standard stress τ_0 (EBB0.5, ENB0.5, etc), with the exception of ENB0.5_LV, the vertical structure of the jets appears relatively robust with respect to the horizontal and vertical resolution (Fig. 3.24). In the experiments with weak forcing (ENB0.05 and ENB0.05_HV), the vertical wavelength of the EDJs decreases slightly, however, with the vertical grid spacing (Fig. A.8). Such a change is shown below to be due to the different vertical wavelength of the IG wave being excited in the two experiments (Section 3.3).

In the experiments forced with τ_0, the EDJ-like currents extend over the full longitudinal width of the basin although their amplitude falls by a significant fraction to the east of the beam (Figs. 3.14 and 3.21). The off-equatorial structure is also found everywhere to the west and within the beam but completely disappears to the east of the beam (Figs. 3.13c and d). The amplitude of the EDJ-like jets and off-equatorial structure reaches 10 to 15 cm s^{-1} within and to the west of the beam and over all experiments they appear as the strongest mean features obtained. The EDJ-like currents appear within the first two years of the experiments (Fig. 3.17) and the off-equatorial structure within the first four years (not shown). Both structures are robust with time, being nearly uninterrupted over the ten years of the experiments.

As for the TEJs, nonlinear processes within the Yanai beam are the likely candidates to explain the generation of the system of currents within the upper 1000 m. One evidence supporting this scenario is the spatial structure of F_x which has been studied for the TEJs in Chapter 4. Fig. A.9 shows F_x along the equator and averaged over the last three years of experiment ENB0.5. Except near the western boundary, the pattern within the upper 1000 m is the same as that obtained when only the component of velocities at the forcing frequency are retained (not shown), suggesting that F_x arises only due to the modification of the directly-forced motion. F_x appears to be strong enough to have triggered the mean surface currents: it is 4 to 5 times stronger within the first 100 m and about twice stronger between 100 and 500 m depth than within the rest of the water column. Also, its spatial pattern is more zonally coherent in x above than below 1000 m and it reverses in sign on the vertical reminiscent of the set of EDJ-like currents.

The remaining question is: What triggers the near-surface patterns in the nonlinear advective terms that are different from those at greater depth. One possibility is that the same way that the effective dissipation of the Yanai beam at depth can

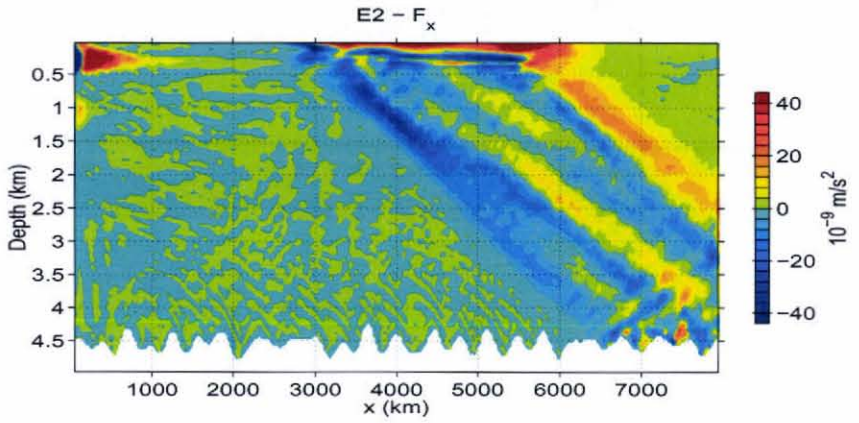

Figure A.9: Mean F_x of Eq. (4.27) at the equator and averaged over years 7–9 in ENB0.5.

be related to the formation of the TEJs, the depth variability of the beam amplitude within the upper 1000 m may be also be related to the formation of mean currents in that depth range. Indeed, the Yanai beam within the upper 1000 m is qualitatively different from its deeper part. The first difference is that the amplitude of the beam in the surface layer (first 50 m in ENB1 to ENB0.05) is systematically about twice as large as the amplitude below 1000 m, even in the experiments with weak forcing (Fig. 3.7a). Another difference is that the Yanai beam is also systematically weaker below the surface layer and above 1000 m, within a range of depths which increases with the surface forcing.

A different and more robust hypothesis is proposed, however, for the EDJs appearing in the experiments with weak forcing, ENB0.05 and ENB0.5_HV. As described in Section 3.3, the only directly-forced, high-frequency motions in these experiments other than the Yanai beam correspond to a second-meridional IG wave with a small vertical wavelength. Because the IG and Yanai waves have about the same frequency and zonal wavelength but different vertical wavenumber and are both decaying in the vertical, one product of their interaction can produce a time-mean

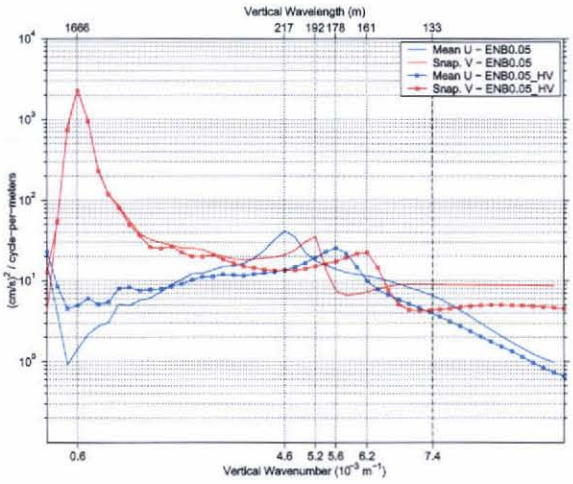

Figure A.10: Power Spectrum in z of snapshot of equatorial V on Jan. 1, 07 and of the mean equatorial U over years 7–9 in ENB0.5 and ENB0.5_HV. The dashed line indicates the vertical wavelength expected for a second-meridional IG wave forced at the central period and zonal wavenumber of the forcing.

long-zonal-scale set of currents alternating in the vertical and resembling the EDJs.

In Section 3.3, it is shown that the vertical wavelength of the IG wave is different between ENB0.05 and ENB0.5_HV because of the different vertical resolution. Because the vertical wavelength of the Yanai wave is, however, similar in both experiments, the theory predicts that the vertical wavelength of the EDJs should be different. Indeed, in both cases, the vertical wavenumber of the mean EDJs m_{EDJs} equals the difference between the vertical wavenumber of IG wave m_{IG} and that of the Yanai wave m_Y (Fig. A.10), that is,

$$m_{EDJs} = m_{IG} - m_Y, \tag{A.1}$$

supporting the hypothesis that the EDJs in the simulations with weak amplitudes arise from the interaction between the Yanai beam and the IG beam. Other evidence is that preliminary results show that the mean zonal nonlinear term F_x obtained in

ENB0.05 (Fig. 4.9a) can indeed be reconstructed from such interaction. More work is needed to confirm or reject this hypothesis.

For both hypothesis proposed for the cases of weak and stronger forcing, however, the surface layer may play an important role. If this is the case, the mechanisms causing the upper mean currents obtained in the numerical experiments may not account for the features observed at greater depth in the ocean.

Appendix B

Analytical solutions

B.1 Approximate analytical solutions

In this section, approximate formulation of the vertical wavenumber m and meridional profile of the single plane Yanai wave are given using the fact that for the regime of frequency and dissipation studied $\tilde{r} = r/\omega \ll 1$ and $\tilde{\lambda} = \lambda/\omega \ll 1$.

The vertical wavenumber is related to $\tilde{r}$, $\tilde{\lambda}$ and other wave characteristics as follows:

$$m = \pm \frac{N}{\omega(1+i\tilde{\lambda})^{1/2}(1+i\tilde{r})^{1/2}}(k + \frac{\beta}{\omega(1+i\tilde{r})}). \tag{B.1}$$

For $\tilde{r} \ll 1$ and $\tilde{\lambda} \ll 1$, Eq. (B.1) can be approximated by:

$$m \approx \pm \frac{Nk}{\omega}(1 - i\frac{\tilde{\lambda}+\tilde{r}}{2}) + \frac{N\beta}{\omega^2}(1 - i\frac{\tilde{\lambda}+3\tilde{r}}{2}). \tag{B.2}$$

The real part m^r gives the same vertical wavenumber as in the inviscid case that is:

$$m^r \approx \pm \frac{N}{\omega}(k + \frac{\beta}{\omega}) \tag{B.3}$$

and the imaginary part gives the inverse vertical decay scale of the wave

$$m^i \approx \mp \frac{N}{2\omega^2}\left[(k + \frac{3\beta}{\omega})r + (k + \frac{\beta}{\omega})\lambda\right]. \tag{B.4}$$

For the regime of dissipation studied, m^i is proportional to r and λ and $m^i \ll m^r$, that is the decay scale is much longer than the wavelength. Furthermore, for the same values of r and λ, the solution decays more rapidly vertically with Rayleigh friction alone than with Newtonian damping alone.

The quantity $c = \pm N/m$ is approximated by

$$c = c^r + ic^i \approx \frac{N}{m^r}(1 - i\frac{m^i}{m^r}) \tag{B.5}$$

so that $c^i \ll c^r$ and $c^r = C$ the gravity wave speed in the inviscid case. Similarly the quantity $1/A^2$ in Eq. (4.11) can be approximated by

$$1/A^2 = \frac{(1+i\tilde{\lambda})^{1/2}}{(1+i\tilde{r})^{1/2}} \approx (1 + i\frac{\tilde{\lambda} - \tilde{r}}{2}) \tag{B.6}$$

so that the approximated meridional profile is

$$\widetilde{v}(y) \approx e^{-\frac{\beta}{2C}y^2} e^{i\frac{\beta}{2C}\left[\frac{\tilde{\lambda}-\tilde{r}}{2} - \frac{m^i}{m^r}\right]y^2}. \tag{B.7}$$

The meridional decay scale is the equatorial Rossby radius in the inviscid case

$$L_{eq} = \sqrt{2C/\beta} \tag{B.8}$$

which is about 2° in the case studied. There is also a meridional change of phase, which is negligible: for the strongest values of dissipation used, the change of phase between 2° and the equator is less than $\pi/40$ and $\pi/100$ for Rayleigh friction alone and Newtonian damping alone respectively. Consequently, the analytical meridional profile does not change much with dissipation.

B.2 Approximate Lagrangian solution

In Chapter 4, the mean Eulerian flow and the Stokes drift are calculated directly from second-order quantities of the wave field while the mean Lagrangian flow is

deduced by summing the two. The calculation, although valid, masks the physical mechanism and in particular the explicit role of the dissipation in the generation of the mean Lagrangian component. Another way to compute the mean Lagrangian flow is to adopt a Lagrangian point of view. Moore (1970), for instance, using asymptotic expansions, deduced that without dissipation the mean Lagrangian flow has to be along geostrophic contours. Andrews and McIntyre (1976) studied the effect on the *zonal-mean* flow by damped equatorial waves and later generalized their findings into a general Lagrangian-mean (GLM) theory applicable not only to finite-amplitude waves but also to a variety of definitions for the Lagrangian mean. We study here the effect of a Yanai beam damped by Rayleigh friction on the *time-mean* flow and compute explicitly the approximate Lagrangian solution in the case of weak amplitude and dissipation. The role of the dissipation is in that case transparent.

The starting point is, in isopycal coordinate (Kasahara 1974), the equations of momenta

$$\frac{Du}{Dt} - fv = -\partial_x P - ru, \tag{B.9}$$

$$\frac{Dv}{Dt} + fu = -\partial_y P - rv, \tag{B.10}$$

the hydrostatic equation

$$\partial_\rho P = gz, \tag{B.11}$$

and the continuity equation

$$\frac{1}{z_\rho}\frac{Dz_\rho}{Dt} + \partial_x u + \partial_y v = 0, \tag{B.12}$$

where P is the Montgomery potential

$$P = p + \rho g z, \tag{B.13}$$

all quantities having the same definition as in Chapter 4 except that they are now functions of ρ instead of z with $\rho \equiv \rho_{tot}/\rho_0$. The derivatives are taken along lines of

constant ρ and the derivative following the motion is defined as

$$\frac{D}{Dt} = \partial_t + u\partial_x + v\partial_y. \tag{B.14}$$

The PV equation is then

$$\frac{D}{Dt}\left[\frac{f+\zeta}{\overline{h}+h}\right] = -r\frac{\zeta}{\overline{h}+h}, \tag{B.15}$$

where $\zeta = \partial_x v - \partial_y u$ is the relative vorticity,

$$-\partial_\rho z = \overline{h}+h \tag{B.16}$$

and

$$\overline{h} = \frac{g}{N^2} \tag{B.17}$$

is the scale over which the mean stratification N varies with depth.

The Lagrangian mean operator $\overline{(\ )}^L$ is defined for any quantity $q(\vec{x},t)$ as

$$\overline{q(\vec{x},t)}^L = \overline{q(\vec{x}+\vec{\xi}(\vec{x},t),t)} \tag{B.18}$$

where $\vec{\xi}(\vec{x},t)$ is the displacement of the water parcel due to any disturbance and $\overline{(\ )}$ is any Eulerian mean operator. In the following a time-mean Eulerian operator is used. The Lagrangian mean of Eq. (B.15) is then simply (Andrews and McIntyre 1978)

$$\frac{\overline{D}^L}{Dt}\overline{\left[\frac{f+\zeta}{\overline{h}+h}\right]}^L = -r\overline{\left[\frac{\zeta}{\overline{h}+h}\right]}^L, \tag{B.19}$$

where

$$\frac{\overline{D}^L}{Dt} = \partial_t + U_L\partial_x + V_L\partial_y, \tag{B.20}$$

and $\vec{U_L} = (U_L, V_L) = (\overline{u}^L, \overline{v}^L)$. If ϵ corresponds to the small amplitude of the wave and assuming that there is no $O(1)$ and $O(\epsilon)$ mean flow, then the mean Lagrangian flow is $O(\epsilon^2)$ and the *steady* version of Eq. (B.19) becomes at $O(\epsilon^2)$

$$V_L = -\frac{r}{\beta}\left[\zeta_L - \frac{\overline{\zeta\,\overline{h}}^L}{\overline{h}}\right], \tag{B.21}$$

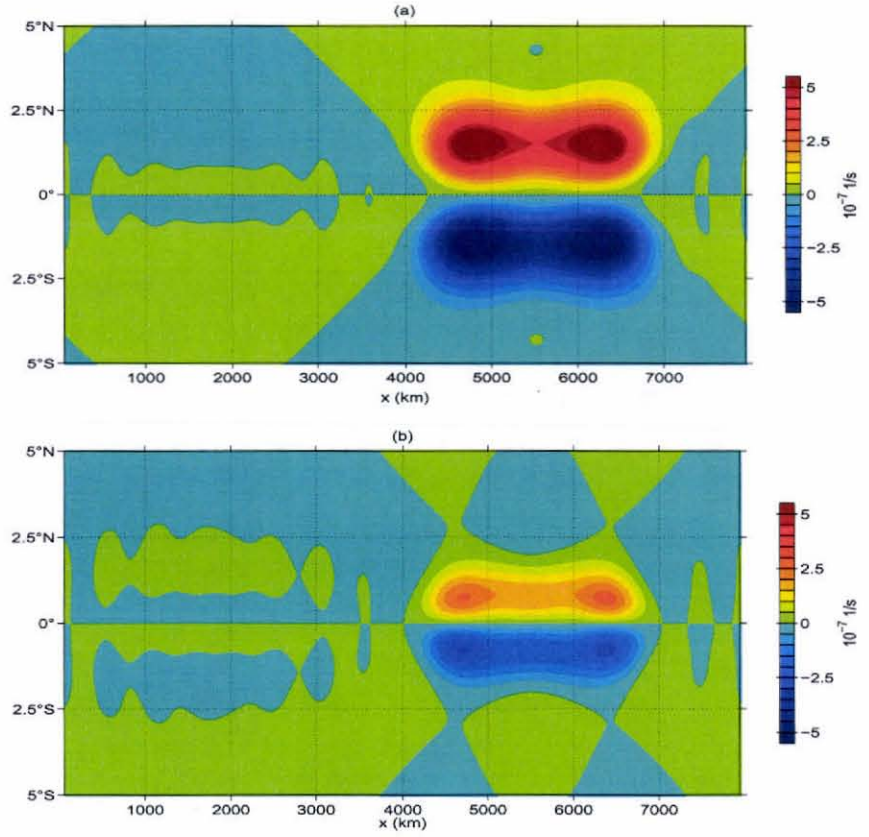

Figure B.1: (a) ζ_L^{inv} and (b) mean $-\overline{\zeta^{inv}\, h^{inv}}/\overline{h}$ at a mean depth of 1000 m.

where $\zeta_L = \overrightarrow{\zeta}^L$, ζ and h are now $O(\epsilon)$ wave quantities and $\overline{h}$ has been considered uniform. Eqs. (B.19) and (B.21) provide the physical reason for the generation of the mean Lagrangian component. The quantity in the r.h.s of Eq. (B.21) is non-zero for the Yanai wave even without dissipation; water parcels have a mean relative vorticity and stretching on average over a wave cycle. Dissipation then acts to reduce this PV anomaly providing a PV source for the mean Lagrangian flow.

To compute the term in the r.h.s. of Eq. (B.21), we notice that at $O(\epsilon^2)$ (Longuet-Higgins 1969)

$$\zeta_L = \zeta_E + \zeta_S \tag{B.22}$$

where $\zeta_E = \overrightarrow{\nabla} \times \overrightarrow{U_E}$ is the curl of the second-order mean Eulerian flow $\overrightarrow{U_E} = (U_E, V_E)$ and

$$\zeta_S = \overline{(u^t \partial_x + v^t \partial_y)\zeta} \tag{B.23}$$

is the $O(\epsilon^2)$ Stokes relative vorticity, that is the averaged relative vorticity of a water parcel over a wave cycle due to the presence of the wave alone. In Eq. (B.23), u^t and v^t are the time integral of the wave quantities u and v:

$$u^t = \int_{t_0}^{t} u(x, y, \rho, t')dt', \tag{B.24}$$

$$v^t = \int_{t_0}^{t} v(x, y, \rho, t')dt', \tag{B.25}$$

with t_0 being an arbitrary instant. Variable ζ_S is a wave property, which, in the case of the Yanai beam, is non-zero even without dissipation. Furthermore,

$$\zeta_E = \overrightarrow{\nabla} \times \overrightarrow{U_E} = \overrightarrow{\nabla} \times \overrightarrow{U_L} - \overrightarrow{\nabla} \times \overrightarrow{U_S}, \tag{B.26}$$

the first term being zero without dissipation in the presence of a meridional boundary ($\overrightarrow{U_L} = 0$; Moore 1970) and the second term being non-zero for the Yanai wave even

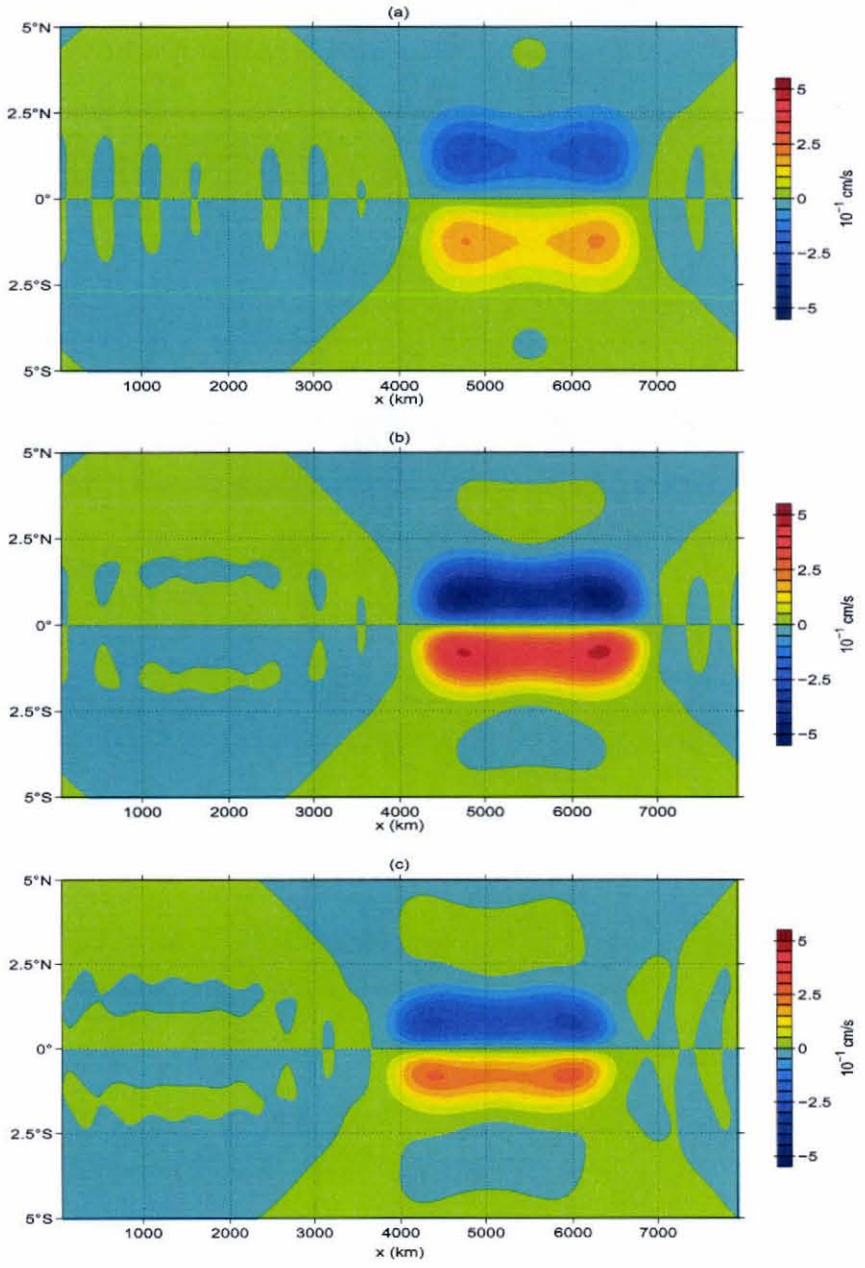

Figure B.2: The Lagrangian meridional flow at the mean depth of 1000 m in the case of the dissipated Yanai beam obtained from (a) $\left[\zeta_L^{inv} - \overline{\zeta^{inv}\, h^{inv}}^L / \overline{h}\right]$, (b) $\left[\zeta_S^{inv} - \overline{\zeta^{inv}\, h^{inv}}^L / \overline{h}\right]$ and (c) the solution of Section 4.6.4.

without dissipation. Thus, for weak dissipation,

$$\zeta_L \approx \zeta_L^{inv} = -\vec{\nabla} \times \vec{U_S}^{inv} + \zeta_S^{inv}. \tag{B.27}$$

Similarly,

$$\overline{\zeta\, h}^L \approx \overline{\zeta^{inv} h^{inv}} \tag{B.28}$$

at $O(\epsilon^2)$ and for weak dissipation, so that

$$V_L \approx -\frac{r}{\beta}\left[\zeta_L^{inv} - \frac{\overline{\zeta^{inv}\, h^{inv}}^L}{\overline{h}}\right], \tag{B.29}$$

and all quantities in the rhs can be deduced from the *inviscid linear wave solution.*

For the Yanai wave and Yanai beam, ζ_L^{inv} and $-\overline{\zeta^{inv}\, h^{inv}}/\overline{h}$ are both positive in the northern hemisphere and negative in the southern hemisphere (Fig. B.1), inducing an equatorward mean Lagrangian flow which is similar in structure but different in amplitude than the meridional Lagrangian flow obtained from $V_E + V_S$ in Section 4.6.4 (Figs. B.2a and c). Such mean meridional transport then results by conservation of mass into the zonal Lagrangian component everywhere to the west of the beam as shown in Fig. 4.19.

Differences in spatial structure between the two solutions arise because in the solution of Chapter 4, the dissipation acting on the second-order mean flow is neglected in Eq. (4.24-4.26). The equivalent term in the Lagrangian solution is $-r/\beta\left[-\vec{\nabla} \times \vec{U_S}\right]$, which is included here. When V_L is computed without that term in the Lagrangian solution, its spatial structure fits better that of V_L obtained from $V_E + V_S$ (Figs. B.2b and c). The difference in amplitude is a direct consequence of using the inviscid wave solution in the Lagrangian solution; in that case, V_L is independent of z, unlike the solution from $V_E + V_S$ which decreases with depth.

References

Andrews, D. G., and M. E. McIntyre, 1976: Planetary waves in horizontal and vertical shear: The generalized Eliassen-Palm relation and the mean zonal acceleration. *J. Atmos. Sci.*, **33**, 2031–2048.

Andrews, D. G., and M. E. McIntyre, 1978: An exact theory of nonlinear waves on a Lagrangian-mean flow. *J. Fluid Mech.*, **89**, 609–646.

Ascani, F., 2005: The equatorial subthermocline circulation in ocean general circulation models. Master Thesis, University of Hawaii, USA.

Ascani, F., E. Firing, D. Wang, and A. Ishida, 2008: Subthermocline equatorial current structure in high-resolution ocean circulation models. to be submitted.

Barnier B., and Coauthors, 2006: Impact of partial steps and momentum advection schemes in a global ocean circulation model at eddy-permitting resolution. *Ocean Dyn.*, **56**, 543–567.

Böning, C. W., and J. Kröger, 2005: Seasonal variability of deep currents in the equatorial Atlantic: a model study. *Deep-Sea Res. I*, **52**, 99–121.

Bourlès, B., M. d'Orgeville, G. Eldin, Y. Gouriou, R. Chuchla, Y. du Penhoat, S. Arnault, 2002: On the evolution of the thermocline and subthermocline eastward currents in the Equatorial Atlantic. *Geophys. Res. Let.*, **29**, doi:10.1029/2002GL015098.

Bourlès, B., C. Andrié, Y. Gouriou, G. Eldin, Y. du Penhoat, S. Freudenthal, B. Dewitte, F. Gallois, R. Chuchla, F. Baurand, A. Aman, and G. Kouadio, 2003: The deep currents in the eastern equatorial Atlantic Ocean. *Geophys. Res. Let.*, **30**, doi:10.1029/2002GL015095.

Boyd, J. P., 1976: The noninteraction of waves with the zonally averaged flow on a spherical Earth and the interrelationships of eddy fluxes of energy, heat and momentum. *J. Atmos. Sci.*, **33**, 2285–2291.

Brandt, P., and C. Eden, 2005: Seasonal variability of deep currents in the equatorial Atlantic: a model study. *Deep-Sea Res. I*, **52**, 199–219.

Brandt, P., V. Hormann, B. Bourlès, J. Fischer, F. A. Schott, L. Stramma, and M. Dengler, 2008: Oxygen tongues and zonal currents in the equatorial Atlantic. *J. Geophys. Res.*, **113**, doi:10.1029/2007JC004435.

Bunge L., C. Provost, J. M. Lilly, M. d'Orgeville, A. Kartavtseff, and J.-L. Melice, 2006: Variability of the horizontal velocity structure in the upper 1600 m of the water column on the equator at 10°W. *J. Phys. Oceanogr.*, **36**, 1287–1304.

Cane, M. A. and D. W. Moore, 1981: A Note on Low-Frequency Equatorial Basin Modes. *J. Phys. Oceanogr.*, **11**, 1578–1584.

Cox, M. D., 1980: Generation and propagation of 30-day waves in a numerical model of the Pacific. *J. Phys. Oceanogr.*, **10,** 1168–1186.

Dengler, M. and D. Quadfasel, 2002: Equatorial deep jets and abyssal mixing in the Indian Ocean. *J. Phys. Oceanogr.*, **32,** 1165–1180.

Dunkerton, T., 1980: A Lagrangian mean theory of wave, mean-flow interaction with applications to nonacceleration and its breakdown. *Rev. Geophys. Space Phys.*, **18,** 387–400.

Dutrieux, P., C. Menkes, J. Murray, E. Firing, J. Hummon and F. Ascani, 2008: Thermocline and subthermocline currents from the central to western equatorial pacific: a snapshot view from the EUC-Fe campaign. *Ocean Sciences Meeting, Orlando, USA.*

Eriksen C. C., 1985: Moored observations of deep low-frequency motions in the central Pacific Ocean: Vertical structure and interpretation as equatorial waves. *J. Phys. Oceanogr.*, **15,** 1085–1113.

Eriksen C. C., and J. G. Richman, 1988: An estimate of equatorial wave energy flux at 9- and 90-day periods in the central Pacific. *J. Geophys. Res.*, **93,** 15,455–15466.

Firing, E., 1987: Deep zonal currents in the central equatorial Pacific. *J. Marine Res.*, **45,** 791–812.

Firing, E., S. Wijffels and P. Hacker, 1998: Equatorial subthermocline currents across the Pacific. *J. Geophys. Res.*, **103,** 21 413–21 423.

Firing E., J. M. Hummon, F. Ascani, and P. Dutrieux, 2008: Pacific subthermocline equatorial currents: a deeper climatology from new shipboard ADCPs. *Ocean Sciences Meeting, Orlando, USA.*

Gent, P. R., 1987: Forcing and friction effects on vertically propagating waves in the equatorial oceans. *J. Phys. Oceanogr.*, **17,** 1897–1908.

Gill, A. E., 1974: The stability of planetary waves on an infinite beta-plane. *Geophys. Fluid Dyn.*, **6,** 29-47.

Gouriou, Y., C. Andrié, B. Bourlès, S. Freudenthal, S. Arnault, A. Aman, G. Eldin, Y. du Penhoat, F. Baurand, F. Gallois and R. Chuchla, 2001: Deep circulation in the equatorial Atlantic Ocean. *Geophys. Res. Let.*, **28,** 819–822.

Haidvogel, D. B., and P. B. Rhines, 1983: Waves and circulation driven by oscillatory winds in an idealized ocean-basin. *Geophys. Astrophys. Fluid Dynamics,* **25,** 1–63.

Harvey, R. R., and W. C. Patzert, 1976: Deep current measurements suggest long waves in the eastern equatorial Pacific. *Science,* **193,** 883–885.

Holland W. H., and P. B. Rhines, 1980: An example of eddy-induced ocean circulation. *J. Phys. Oceanogr.*, **10,** 1010–1030.

Hua B. L., M. d'Orgeville, C. Menesguen, and H. Sasaki, 2008: Destabilization of mixed Rossby gravity waves and equatorial zonal jets formation. submitted to J. Fluid Mech..

Ishida, A., Y. Kashino, H. Mitsudera, N. Yosioka, and T. Kadokura, 1998: Preliminary results of a global high-resolution GCM experiment. *J. Fac. Sci. Hokkaido Univ. Ser. 7,* **11,** 441–460.

Jochum, M., and P. Malanotte-Rizzoli, 2003: The flow of AAIW along the equator. *Interhemispheric Water Exchanges in the Atlantic Ocean,* Elsevier Oceanographic Series, pp. 193–212.

Johnson, G. C., E. Kunze, K. E. McTaggart, and D. W. Moore, 2002: Temporal and spatial structure of the equatorial deep jets in the Pacific Ocean. *J. Phys. Oceanogr.,* **32,** 3396–3407.

Johnson, G. C., and D. Zhang, 2003: Structure of the Atlantic Ocean equatorial deep jets. *J. Phys. Oceanogr.,* **33,** 600–609.

Kessler, W. S., G. C. Johnson, and D. W. Moore, 2003: Sverdrup and nonlinear dynamics of the Pacific equatorial currents. *J. Phys. Oceanogr.,* **33,** 994–1008.

Kasahara, A., 1974: Various vertical coordinate systems used for numerical weather prediction. *Mon. Wea. Rev.,* **102,** 509–522.

Li X., and P. Chang, 1999: Mixing induced by the Atlantic equatorial wave activity

in an eddy-resolved OGCM. *J. Geophys. Res.*, **104,** 13,303–13,315.

Longuet-Higgins, M. S., 1969: On the transport of mass by time-varying ocean currents. *Deep-Sea Res. I,* **16,** 431–447.

Luyten, J. R., and J. C. Swallow, 1976: Equatorial undercurrents. *Deep-Sea Res.*, **23,** 999–1001.

Lyman J. M., G. C. Johnson, and W. S. Kessler, 2007: Distinct 17- and 33-day Tropical Instability Waves in subsurface observations. *J. Phys. Oceanogr.*, **37,** 855–872.

Maltrud, M. E. and J. L. McClean, 2005: An eddy resolving global 1/10° ocean simulation. *Ocean Modelling,* **8,** 31–54.

Masina S., and S. G. H. Philander, 1999: An analysis of tropical instability waves in a numerical model of the Pacific Ocean. 1. Spatial variability of the waves. *J. Geophys. Res.*, **104,** 29,613–29,635.

Masumoto, Y., H. Sasaki, T. Kagimoto, N. Komori, A. Ishida, Y. Sasai, T. Miyama, T. Motoi, H. Mitsudera, K. Takahashi, H. Sakuma, and T. Yamagata, 2004: A fifty-year eddy-resolving simulation of the world ocean–preliminary outcomes of OFES (OGCM for the Earth Simulator). *J. Earth Simulator,* **1,** 35–56.

McCreary, J. P., 1984: Equatorial beams. *J. Marine Res.*, **42,** 395–430.

McCreary, J. P., 1985: Modeling equatorial ocean circulation. *Annu. Rev. Fluid Mech.*, **17**, 359–409.

McCreary, J.P., and R. Lukas, 1986: The response of the equatorial ocean to a moving wind field. *J. Geophys. Res.*, **91**, 11,691–11,705.

McPhaden M. J., J.A. Proehl, and L.M. Rothstein, 1986: The interaction of equatorial Kelvin waves with realistically sheared zonal currents. *J. Phys. Oceanogr.*, **16**, 1499–1515.

McPhaden, M. J., and P. Ripa, 1990: Wave-mean flow interactions in the equatorial ocean. *Annu. Rev. Fluid Mech.*, **22**, 167–205.

Menkes C. E., and Coauthors, 2002: A whirling ecosystem in the equatorial Atlantic. *Geophys. Res. Let.*, **29**, doi:10.1029/2001GL014576.

Moore, D. W., 1968: Planetary-gravity waves in an equatorial ocean. Ph.D. Thesis, Harvard University, USA.

Moore, D. W., 1970: The mass transport velocity induced by free oscillations at a single frequency. *Geophy. Fluid Dyn.*, **1**, 237–247.

Nakano, H., and H. Hasumi, 2005: A series of zonal jets embedded in the broad zonal flows in the Pacific obtained in eddy-permitting ocean general circulation models. *J. Phys. Oceanogr.*, **35**, 474–488.

Ollitrault M., M. Lankhorst, D. Fratantoni, P. Richardson, and W. Zenk, 2006: Zonal intermediate currents in the equatorial Atlantic Ocean. *Geophys. Res. Let.*, **33**, doi:10.1029/2005GL025368.

d'Orgeville, M., and B. L. Hua, 2005: Equatorial inertial-parametric instability of zonally symmetric oscillating shear flows. *J. Fluid Mech.*, **531**, 261–291.

d'Orgeville, M., B. L. Hua and H. Sasaki, 2007: Equatorial Deep Jets triggered by a large vertical scale variability within the western boundary layer. *J. Marine Res.*, **65**, 1–25.

Pacanowski, R. and S. Philander, 1981: Parametrization of vertical mixing in numerical models of tropical oceans. *J. Phys. Oceanogr.*, **11**, 1443–1451.

Pedlosky, J., 1996: *Ocean circulation theory*, Springer-Verlag, 453 pp.

Penduff T., J. Le Sommer, B. Barnier, A.-M. Treguier, J.-M. Molines, and G. Madec, 2007: Influence of numerical schemes on current-topography interactions in 1/4° global ocean simulations. *Ocean Sci.*, **3**, 509–524.

Proehl, J. A., 1990: Equatorial wave-mean Flow interaction: The long Rossby waves. *J. Phys. Oceanogr.*, **20**, 274–294.

Rhines P. B., and W. R. Holland, 1979: A theoretical discussion of eddy-driven mean flows. *Dyn. Atmos. Oceans*, **3**, 289–325.

Ripa, P., 1982: Nonlinear wave-wave interactions in a one-layer reduced-gravity model on the equatorial β plane. *J. Phys. Oceanogr.*, **12,** 97–111.

Rothstein L. M., M. J. McPhaden, and J. A. Proehl, 1988: Wind forced wave-mean Flow interactions in the equatorial waveguide. Part I: The Kelvin wave. *J. Phys. Oceanogr.*, **18,** 1435-1447.

Schott, F. A., L. Stramma, and J. Fischer, 1995: The warm water inflow into the western tropical Atlantic boundary regime, spring 1994. *J. Geophys. Res.*, **100,** 24,745–24,760.

Schott, F. A., M. Dengler, P. Brandt, K. Affler, J. Fischer, B. Bourles, Y. Gouriou, R. L. Molinari, and M. Rhein, 2003: The zonal currents and transports at 35°W in the tropical Atlantic. *Geophys. Res. Let.*, **30,** 1349–1352.

Send, U., C. Eden, and F. A. Schott, 2002: Atlantic equatorial deep-jets: Space-time structure and cross-equatorial fluxes. *J. Phys. Oceanogr.*, **32,** 891–902.

Tang T. Y., R.H. Weisberg, and D. Halpern, 1988: Vertical structure of low frequency variability in the eastern equatorial Pacific Ocean. *J. Phys. Oceanogr.*, **18,** 1009–1019.

Vallis, G. K., 2006: *Atmospheric and oceanic fluid dynamics,* Cambridge University Press, 745 pp.

Weisberg, R. H., A. M. Horigan and C. Colin, 1979: Equatorially trapped Rossby-

gravity wave propagation in the Gulf of Guinea. *J. Marine Res.*, **37**, 67–86.

Weisberg, R. H. and A. M. Horigan, 1981: Low-frequency variability in the equatorial Atlantic. *J. Phys. Oceanogr.*, **11**, 913–920.

Wunsch, C., 1977: Response of an equatorial ocean to a periodic monsoon. *J. Phys. Oceanogr.*, **7**, 497–511.

Yamagata, T., and S. G. H. Philander, 1985: The role of damped equatorial waves in the oceanic response to winds. *J. Oceanogr. Soc. Japan*, **41**, 345–357.